Stony Brook University

Transition Metal Borates as Cathode Materials for Rechargeable Batteries

A Dissertation Presented

by

Shou-Hang Bo

to

The Graduate School

in Partial Fulfillment of the

Requirements

for the Degree of

Doctor of Philosophy

in

Chemistry

Stony Brook University

August 2014

Stony Brook University

The Graduate School

Shou-Hang Bo

We, the dissertation committee for the above candidate for the

Doctor of Philosophy degree, hereby recommend

acceptance of this dissertation.

Clare P. Grey, D. Phil., Advisor
Professor, Department of Chemistry, Stony Brook University

Peter G. Khalifah, Ph. D., Advisor
Assistant Professor, Department of Chemistry, Stony Brook University

Benjamin Hsiao, Ph. D., Chairperson
Professor, Department of Chemistry, Stony Brook University

Michael G. White, Ph. D., Third Member
Professor, Department of Chemistry, Stony Brook University

Marca M. Doeff, Ph. D., Outside Member

Staff Scientist, Environmental Energy Technologies Division, Lawrence Berkeley National Lab

This dissertation is accepted by the Graduate School

Charles Taber
Dean of the Graduate School

Abstract of the Dissertation

Transition Metal Borates as Cathode Materials for Rechargeable Batteries

by

Shou-Hang Bo

Doctor of Philosophy

in

Chemistry

Stony Brook University

2014

High-capacity rechargeable batteries play a central role in a variety of emerging technologies, including mobile electronics, plug-in and hybrid electric vehicles, and grid-scale storage. All of these technologies will greatly benefit from the design and discovery of next-generation cathode materials that can deliver substantially higher energy densities at reduced cost. Transition metal borates are promising cathode candidates for battery applications, since the mass/charge ratio (*m*/*z*) of borate group (BO_3^{3-}) is the lowest among all common polyanion groups. A variety of borate based compounds were therefore explored as potential Li-ion and Mg-ion battery cathodes in this dissertation

Comprehensive studies were carried out to understand the complex structural transformation of $LiFeBO_3$ during battery cycling. It is observed that two distinct oxidative processes can occur in $LiFeBO_3$ under different conditions, resulting in either delithiation or degradation. The delithiated and degraded phases share essentially the same Fe-B-O framework as the pristine $LiFeBO_3$ phase, and can both reversibly cycle Li, but they differ in the presence

(or absence) of Li/Fe disorder. This subtle structural difference results in a much higher operation potential for the pristine phase (2.8 V) than the degraded phase (1.8 V). $LiCoBO_3$, with the same structural framework was also studied. However, it is observed that $LiCoBO_3$ could not be delithiated due to its extremely low conductivity.

$Mg_xFe_{2-x}B_2O_5$ (x = 2/3 and 4/3) and $MgVBO_4$ were investigated for their potential applications as cathodes for Mg-ion batteries. It is observed that Mg/Fe and Mg/V disorder is responsible for the low degree of demagnesiation achieved for $MgMB_2O_5$ and $MgVBO_4$ at room temperature. However, a large degree of demagnesiation was achieved when $Mg_xFe_{2-x}B_2O_5$ was heated in air, suggesting the $Mg_xFe_{2-x}B_2O_5$ structure could be demagnesiated if kinetic limitations are overcome.

Table of Contents

Chapter 3

Structures of degraded and delithiated $LiFeBO_3$, and their distinct structural changes upon electrochemical cycling

Chapter 4

Thin film and bulk investigations of $LiCoBO_3$ as a Li-ion battery cathode

Chapter 5

Defect tolerant diffusion channels in ribbon-type borates: structural insights into $MgVBO_4$ and $Mg_xFe_{2-x}B_2O_5$

Chapter 6

Conclusions

List of Figures

List of Tables

Acknowledgments

I would like to first thank my supervisors, Prof. Clare Grey and Prof. Peter Khalifah, for their tremendous support during my PhD career. It is their support that makes the completion of this dissertation a possible task. I would never grow to be the current me without their training.

I am very grateful to other committee members. Prof. Benjamin Hsiao and Prof. Michael White have been serving as my committee chair and third member since the beginning of my PhD career. Their advices and encouragements over the past years have always motivated me to move forward. Dr. Marca Doeff, the outside member of my committee, travelled all the way from California to New York, to attend my defense. It is an honor to have her as a committee member.

I would also like to thank Dr. Yuri Janssen, Dr. Lin-Shu Du and Dr. Yan-Yan Hu, who are my mentors in many areas of science. I have benefited greatly from working with them. There are many other collaborators who have supported my research in the past, including Dr. Kyung-Wan Nam, Dr. Feng Wang, Dr. Lijun Wu, Dr. Andrew Ilott, Dr. Olaf. Borkiewicz, Dr. Gunwoo Kim, Dr. Riza Dervisoglu, Dr. Wenqian Xu, Dr. Dongli Zeng, Dr. Lihua Zhang, Dr. Xiaoqing Yang, Dr. Jason Graetz, Dr. Peter Chupas, Dr. Karena Chapman, Dr. Yimei Zhu and Dr. John Parise, Mr. Hugh Glass and Dr. Sian Dutton. If I had ever accomplished anything scientifically, their help is indispensable. Colleagues from Grey's group and Khalifah's group are also acknowledged for their everyday support of my research.

Last but not least, I would like to thank my wife and my parents.

Chapter 1

Introduction

1.1 Motivation

Global warming due to burning fossil fuels has caused a substantial climate change. A major contributor on fossil fuel consumption is transportation. In the United States, for instance, 25% of the overall energy was used in transportation in 2006 and it accounted for almost 70% of the total petroleum that was consumed[1]. Developing new technologies that could reduce or even eliminate transportation's reliance on petroleum is important for reducing carbon emissions.

The widespread application of plug-in hybrid electric vehicles (PHEVs), which utilize electricity as well as gasoline, is expected to greatly reduce the carbon footprint of automotives. The core of this technology is a battery pack that can provide enough power to the vehicles. Lithium ion batteries (LIBs), owing to their high volumetric and gravimetric energy density (Figure 1.1) [2], are considered to be one of the most promising candidates for such applications. However, despite the current commercial success of LIBs in high-end portable electronics, their development and application in PHEVs is impeded primarily by cost, toxicity and safety issues related to the cathode part. Therefore, discovering economic and environmentally benign cathode materials is the key to further extend the application of LIBs.

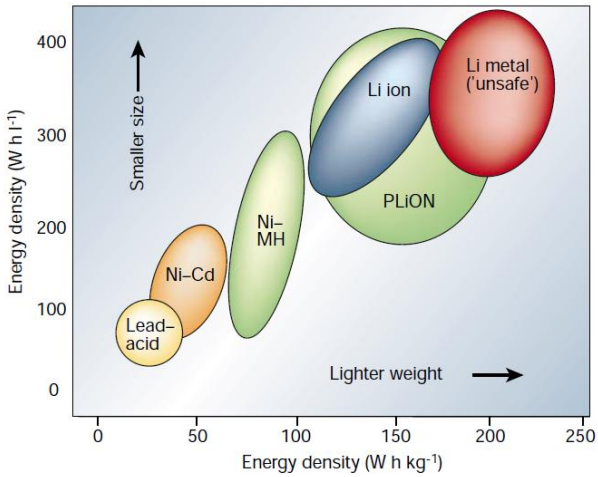

Figure 1.1. Volumetric and gravimetric energy density comparison of different battery technologies. Figure is reproduced with permission from Ref 2.

1.2 Li-ion batteries

Prior to discussing the possible ways to overcome the bottlenecks in the development of Lithium-ion batteries (LIBs), it is worthwhile introducing the basic working mechanism of LIBs and discussing the critical parameters that determine the performance of a battery.

LIBs based on intercalation and deintercalation of lithium in both electrodes are rechargeable batteries in which lithium ions are shuffled back and forth between cathode and anode when cycling (Figure 1.2). For instance, in the case of $LiCoO_2$-based LIBs, $LiCoO_2$ and graphite are used as the cathode and anode respectively. During charging, lithium ions are extracted from the cathode $LiCoO_2$. Simultaneously, they are transported and inserted into the anode (*i.e.*, graphite). The electrochemical reactions can be depicted as following:

$$LiCoO_2 \longrightarrow x\ Li^+ + Li_{1-x}CoO_2 + x\ e^-$$

$$x\ Li^+ + x\ e^- + 6C \longrightarrow Li_xC_6$$

When discharging, the reactions proceed in the opposite direction. The frameworks of $LiCoO_2$ and graphite remain stable during intercalation and deintercalation, offering the possibility of charging and discharging the battery for many cycles.

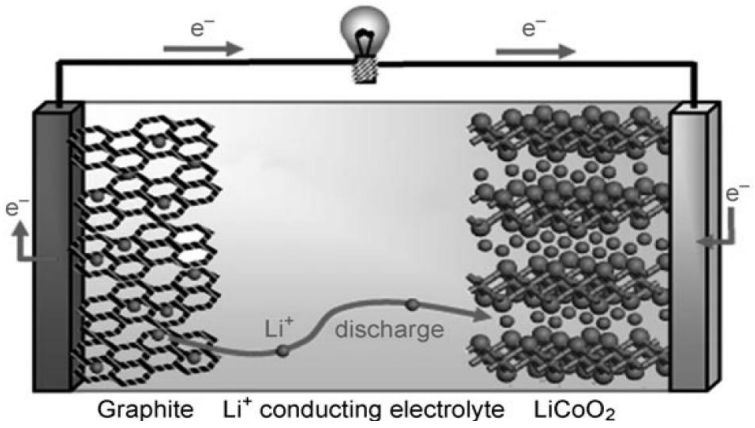

Figure 1.2. Rechargeable LIB with $LiCoO_2$ and graphite as cathode and anode respectively. Figure is reproduced with permission from Ref 3.

Among the many parameters (operation voltage, reversible capacity, thermal stability and cycling life) which are extremely important to evaluate the performance of a LIB, the energy that a battery can store or provide is directly related to its operation voltage and reversible capacity. Operation voltage is determined by the difference of chemical potentials of lithium in the cathode and the anode. The amount of lithium that can be reversibly inserted into and extracted from the cathode and anode materials sets the maximum reversible capacity that can be achieved. For example, LIB in which $LiCoO_2$ is the cathode operates on the redox couple of Co^{4+}/Co^{3+}

upon delithiation and lithiation which gives an average voltage of 3.7 V (*vs.* Li^+/Li). Only 0.5 Li can be reversibly extracted from and inserted into the $LiCoO_2$ framework when charging and discharging. As a result, a specific capacity of approximately 140 mAh/g can be achieved. The gravimetric energy density (*i.e.*, a product of the operation voltage and specific capacity) of such a $LiCoO_2$-C battery is almost two times as that of the nickel-metal hydride battery, which is the other major competitor in the battery market.

Although the current portable electronics market is dominated by $LiCoO_2$-based LIBs, cobalt is toxic, not naturally abundant, and therefore, expensive. It only makes up 20 ppm in the earth's crust which is only $1/10^3$ of iron [4]. Also, the annual production is only 17,000 tons which is far less than that of iron, manganese and other major industrial metals [5]. It can be expected that the price of cobalt will rise continuously over time as more and more cobalt will be extracted from the crust. Replacing cobalt with other major industrial metals appears to be a feasible way to tackle this cost issue.

Efforts to seek for better cathode materials for LIBs have never ceased in the past thirty years. Followed the pioneer work on $LiCoO_2$ [6] and $LiFePO_4$ [7], researchers are currently investigating various materials, especially oxoanion-based materials, as cathodes for battery applications. A brief overview of the development of cathode materials for LIBs will be provided in the following discussion. Attempts will be made to correlate the structures of the materials with their electrochemical performance.

$LiCoO_2$, which was used as cathode in the first commercial LIB developed by SONY, exhibits the α-$NaFeO_2$ layered structure with a space group of *R-3m* (#166) (Figure 1.3). The oxygen atoms adopt a cubic close-packed (*ccp*) arrangement. All the octahedral sites are occupied by Li and Co, while leaving all tetrahedral sites empty. Possibly owing to the large

difference of effective ionic radii between Li^+ (0.9 Å) and Co^{3+} (0.5 Å) [8], LiO_6 and CoO_6 octahedra are stacked in an ordered manner alternating along the *c*-lattice direction. The layered framework allows two dimensional (2D) electronic conduction as well as lithium diffusion. Accordingly, it is possible to cycle the materials with a relatively high rate. One of the inherent drawbacks with this compound is that only 0.5 Li per formula can be reversibly extracted and inserted which gives a specific capacity of only 140 mAh/g. This is mostly attributed to an irreversible reversible structural transition after 1/2 Li is extracted [9-10]. Safety issues also arise, after charging the battery over 4.2 V (*vs.* Li^+/Li), due to the dissolution of Co into the electrolyte[11]. Therefore, tremendous research efforts have been devoted to finding alternative cathodes which contain major industrial metals instead of cobalt, leading to the discovery of $LiFePO_4$ as an outstanding cathode.

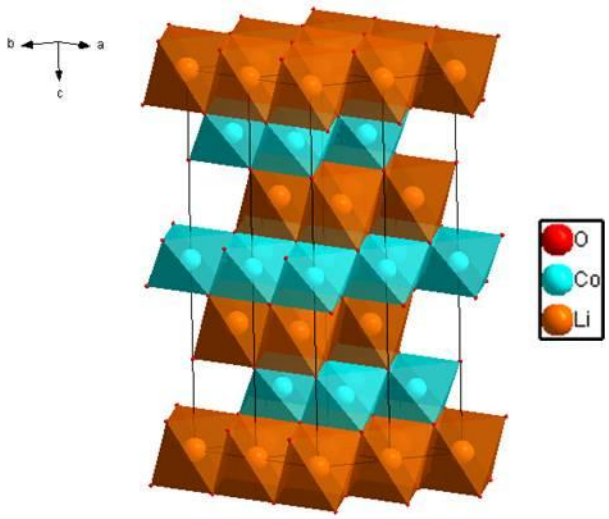

Figure 1.3. $LiCoO_2$ with a $NaFeO_2$ layered structure (*R-3m*, #166).

$LiFePO_4$ (space group *Pnma, #*62), a naturally occurring insulating mineral, possesses a distorted hexagonal close-packed (*hcp*) oxygen array. 1/8 of the tetrahedral sites are occupied by P, and 1/2 of the octahedral sites are occupied by Li or Fe (Figure 1.4). In $LiFePO_4$, Li and Fe layers are separated and stacked along the *a* axis. However, unlike $LiCoO_2$, edge-shared LiO_6 octahedra and corner-shared FeO_6 octahedra are connected along the *b* axis. This 1D connection makes $LiFePO_4$ a poor ionic and electronic conductor, since the lithium diffusion is constrained to be one dimensional (1D) and the electron or hole hopping energy barriers are made higher. Additionally, Li and Fe anti-site[12] and/or sarcopside-like defects[13] can be present in the $LiFePO_4$ structure. A possible consequence of these defects is the blockage of lithium diffusion pathways which dramatically affects the rate of lithium diffusion through the framework [14]. Surprisingly, with simple modifications such as coating carbon [15], reducing particle size [16] and doping aliovalent or isovalent cations [17], $LiFePO_4$ can yield excellent rate performance. It is also worth noting that cycling $LiFePO_4$, in most cases, gives a very flat plateau at around 3.4 V (*vs.* Li^+/Li), since the electrochemical reaction proceeds through a two-phase reaction pathway (with end members of $LiFePO_4$ and $FePO_4$) [7]. The striking similarity between $LiFePO_4$ and $FePO_4$ provides excellent reversibility. Studies of $LiFePO_4$ also highlight the possibility to fine tune the potential of the Fe^{3+}/Fe^{2+} redox couple through crystal structure engineering, such as introducing different highly covalent oxoanions (Figure 1.5) [18,19]. This finding opened the pathway to investigate other oxoanion-based cathode materials for LIBs, leading to the discovery of several promising oxoanion-based cathode materials thereafter.

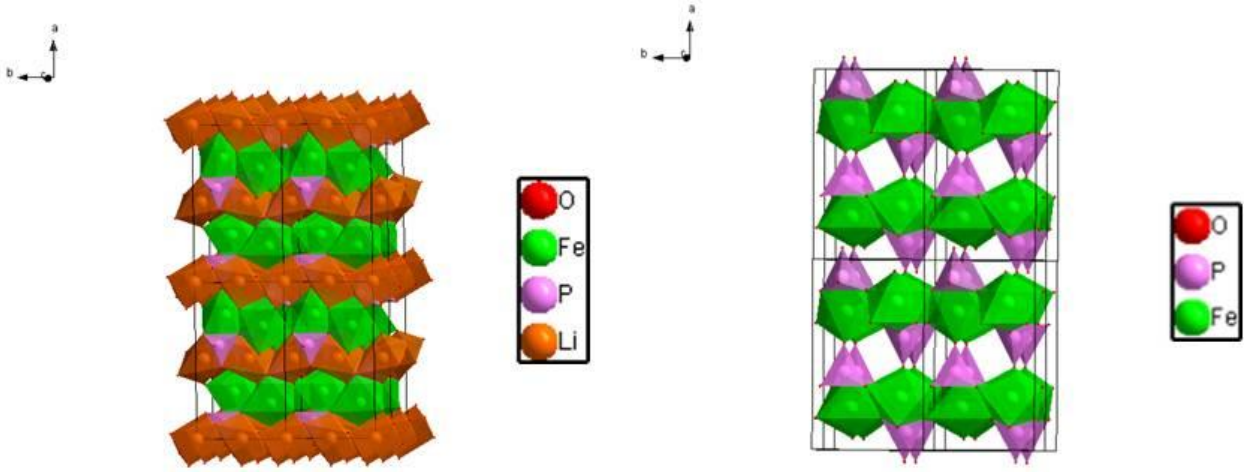

Figure 1.4. Crystal structure of $LiFePO_4$ (left) and $FePO_4$ (right).

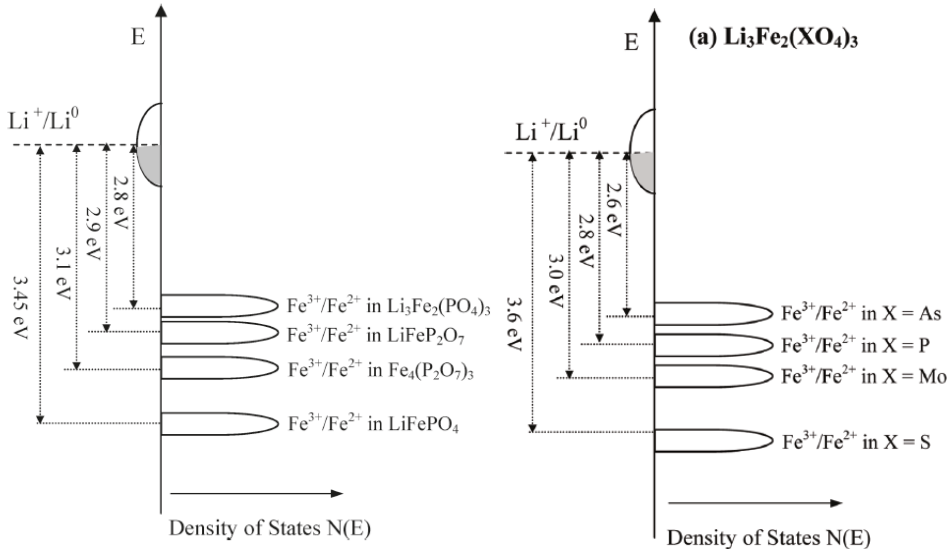

Figure 1.5. Positions of Fe^{3+}/Fe^{2+} redox couples relative to Fermi energy of lithium in different phosphates (left) and in NASICON structure with different oxoanions (right). Figure is reproduced with permission from Ref 18.

One of the oxoanion-based cathode materials which has attracted extensive attention in recent years is Li_2MSiO_4 (*M* = Fe and Mn) [20, 21]. As reported by A. Yamada and his coworkers [22], in Li_2FeSiO_4 (space group $P2_1$, #4), 1/4 of the tetrahedral sites are occupied by cations, and oxygen atoms adopt an *hcp* arrangement (Figure 1.6). LiO_4 tetrahedra are corner-shared along the [10-1] direction, and FeO_4 tetrahedra are isolated by SiO_4 and LiO_4 tetrahedra. Poor electronic and ionic conductivity is therefore expected in this class of compounds. One great promise these materials offer is the removal of multiple Li per formula, *via* the utilization of M^{4+}/M^{2+} redox couple. As a result, a theoretical capacity of *ca.* 330 mAh/g is possible. However experimentally, no more than one lithium per formula can be extracted from the host upon consecutively cycling with a corresponding capacity of approximately 160 mAh/g [20,21,23-25]. Further explorations to realize the 2-electron redox reaction in this type of materials are still needed.

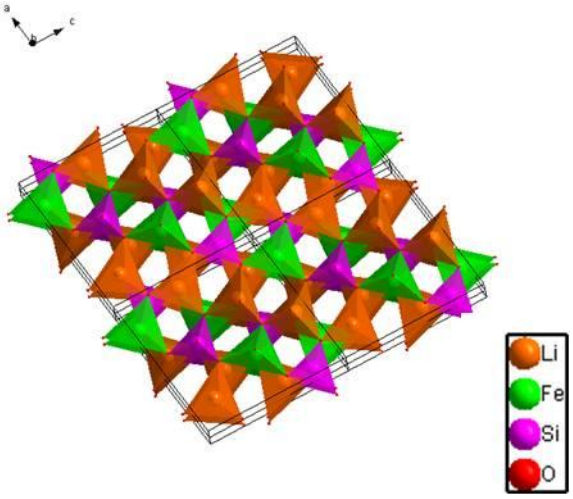

Figure 1.6. Crystal structure of Li_2FeSiO_4 ($P2_1$, #4).

Another class of materials which have received considerable attention more recently are the fluoro-oxoanion-based materials [26,27]. The introduction of fluorine atom into the framework can in principle further raise the operation voltage, owing to the highly electron-withdrawing character of F^-. For example, $LiFeSO_4F$ [27] shows a plateau at around 3.6 V (*vs*. Li^+/Li) which is higher than that of $LiFePO_4$ (3.4 V *vs*. Li^+/Li). It is also intriguing to note that $LiFeSO_4F$ can give a specific capacity of 140 mAh/g at 0.1C (1C corresponds to fully charge a battery within one hour, and 0.1 C corresponds to fully charge the battery within 10 hours) without any surface coating or particle size reduction. This indicates that $LiFeSO_4F$ has much better electronic and ionic conductivity compared to $LiFePO_4$.

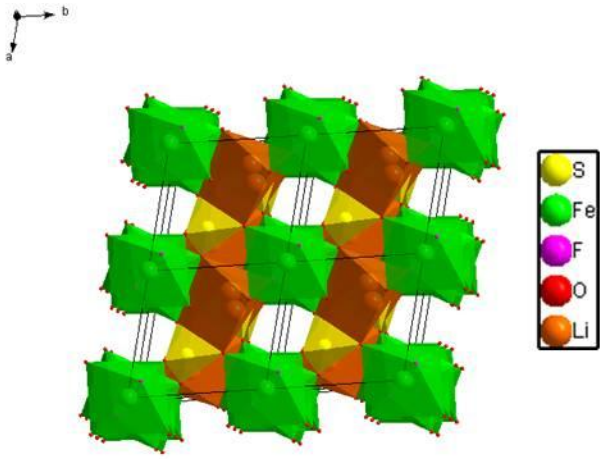

Figure 1.7. Crystal structure of $LiFeSO_4F$ (*P-1*, #2).

A class of materials that are closely related to this dissertation research is lithium metal borates (*i.e.*, Li*M*BO_3, M = Mn, Fe, Co). These phases are promising cathode materials for Li-ion battery applications, since borate group is light and offers a higher gravimetric energy density

compared to other polyanion systems. While a more complete overview of related research regarding Li*M*BO_3 phases will be given in subsequent chapters, a brief structural description of these phase are given here. Two structural types were found to exist for Li*M*BO_3, the monoclinic form with trigonal bipyramid coordination for both Li and *M*, and the hexagonal form with square pyramid coordination for *M* and tetrahedral coordinated Li. Based on prior work, the monoclinic form of $LiFeBO_3$ and $LiMnBO_3$ have shown intriguing electrochemical performance. The hexagonal form of Li*M*BO_3 phases, on the other hand, does not show appreciable electrochemical activity. This may be related to the peculiar coordination environment of transition metal in the hexagonal structure of Li*M*BO_3 (*i.e.*, square pyramid), which is often found to stabilize either the lithiated or the delithiated phases but not both of them.

1.3 Scope

The primary focus of this dissertation is the study of various borate based cathode materials for LIBs, although some efforts were also dedicated to Mg-ion batteries which will be briefly summarized in the last chapter of this dissertation. By combining various structural characterization tools, especially diffraction and nuclear magnetic resonance (NMR) techniques, the aim of this dissertation research was to develop a fundamental understanding of structure-property correlations in borate materials for battery applications. General principles regarding diffraction and NMR techniques are discussed below.

1.4 Bragg and total scattering

Diffraction or scattering is a principal technique in characterization of solids. The occurrence of Bragg scattering relies on the presence of periodicity in solids (*i.e.*, presence of repeating units). Therefore, Bragg scattering is often limited to the characterization of crystalline

materials. Total scattering, on the other hand, also takes into account diffuse scattering that arises when "imperfections" in solids are present (*i.e.*, any disruption of the perfect periodicity such as defects), and can be thus extended to the characterization of amorphous materials such as glasses. While Bragg scattering can serve as a sufficient tool to characterize the long range average structure of a crystalline solid, total scattering can provide additional insights to the short-to-medium range structures of solids, allowing the nature of existing defects to be unraveled.

Bragg reflection occurs only when Bragg's law is met, that is:

$$2d \sin \theta = \lambda$$

where d is the distance between two adjacent lattice planes in a crystalline solid, θ is the so-called Bragg angle between the incident beam and the reflection planes under consideration (Figure 1.8), and λ is the wavelength of the incident beam. The derivation of Bragg law can be found in almost every chemistry or physics related text books, and therefore, will not be repeated. Instead, some implications of this formula is highlighted.

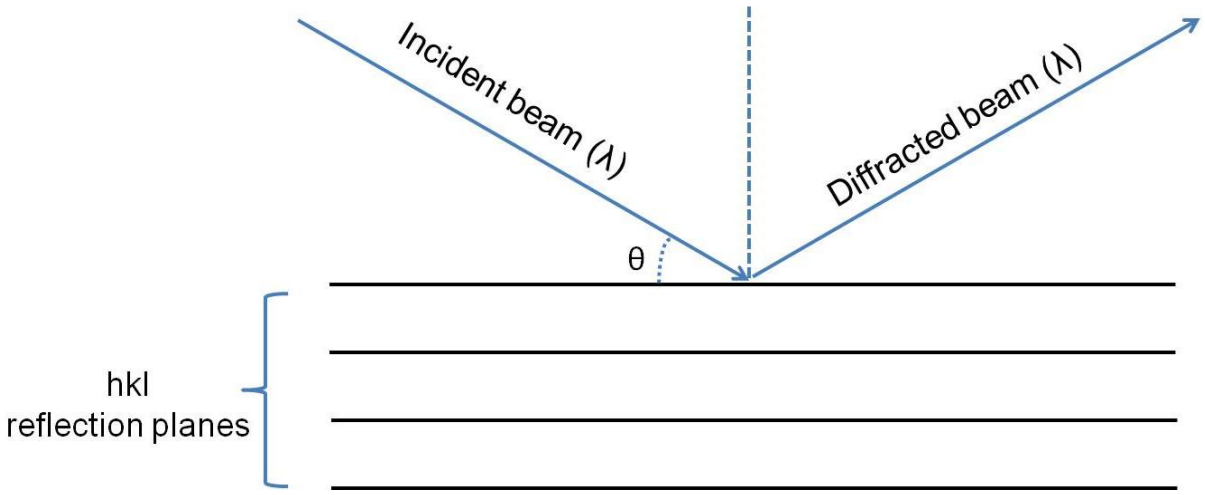

Figure 1.8. Schematic illustration of the Bragg condition.

Since sin θ is less than 1, the lowest d spacing (d_{min}) that can be probed by a specific radiation with certain wavelength λ is set by the quantity of $\lambda/2$. Thus in the case of Cu radiation, which is widely used in laboratory powder diffractometers, d_{min} is ~0.8 Å. Mo radiation, which is typically used in laboratory single crystal diffractometers gives a d_{min} of ~ 0.4 Å. A modern synchrotron X-ray beam with a wavelength of ~0.4 Å, such as the 11BM beamline at Advanced Photon Source (APS), can probe d spacings as low as ~0.2 Å. This limit can be pushed even further when considering high-energy electrons that are employed in modern electron diffraction analysis (d_{min} is on the order of 0.02 Å). As the number of Bragg diffraction peaks increases rapidly with decreasing d, the use of high-energy sources (or beams) often yields sufficiently large data sets for accurate structural analysis.

Since d is often the quantity of interest, varying either λ or θ while keep the other constant can give a measure of d. This consideration leads to two different experimental methodologies. One uses radiations with specific wavelengths, such as the various radiations

discussed in the previous paragraph. Information about *d* can be therefore inferred through examining the intensities of diffracted beams as a function of θ. The other approach measures diffraction intensities at one or several fixed Bragg angles with a energy dispersive source, such as a continuous-wavelength radiation (*i.e.*, the so-called white beam) and time-of-flight neutrons.

Two pieces of information are particularly important in a Bragg scattering measurement: (1) the angles at which Bragg scattering occur and (2) the corresponding intensities. The angles as discussed earlier are determined by the Bragg's law. This information correlates with the lattice dimension of a crystalline solid, which is characterized by the six lattice parameters (a, b, c, α, β, γ). In most cases, one will observe that a few or many peaks are missing in the Bragg scattering pattern but are predicted by the lattice dimension. These missing peaks arise most likely from the so-called systematic absences due to the centering of the lattice (*e.g.*, the (100) peak is missing in α-Fe since the lattice is body-centered) and/or the presence of symmetry elements in the structure (*e.g.*, glide plane). Therefore, in principle, a close examination of the Bragg scattering peak positions allows the lattice dimension to be unambiguously assigned, and the possible space group(s) to be determined.

The corresponding intensities reflect the contents (*i.e.*, compositions) and the arrangements of atoms within a crystalline solid. This correlation can be best rationalized when considering the physical processes that occur when an incident beam hits the atoms within a crystalline solid. The incident beam, either X-rays, neutrons or electrons, can be considered as electromagnetic waves with characteristic wavelengths and magnitudes. When the incident beam hits a point source (such as X-ray hits the electrons associated with an atom), this point source will act as a center for secondary scattered waves. It is these secondary scattered electromagnetic waves that interfere with each other producing the diffraction patterns. Within the content of

Bragg scattering, the scattered waves possess the same wavelength as the incident beam. However, their magnitudes, and relative phases at a specific location in space depend on the nature of the scattering point sources and their relative positions. Therefore, the diffracted intensity at where the constructive interference occurs (*i.e.*, where the Bragg's law is met) depends on the scattering power (magnitude) and the relative positions (phase) of all the point sources. It should be noted that the scattering power of a specific atom also depends the incident beam. For the most commonly used X-ray source, the X-ray scattering power of a specific atom is proportional to the number of electrons associated with it. For instance, the scattering power of Zn (z = 30) is 10 times higher than that of Li (z = 3). This highlights the difficulty of locating light elements by X-ray diffraction, especially when heavy elements are present. This difficulty could be solved by the use of multiple data sets that are collected *via* different incident beams, such as X-ray and neutron, a method that is extensively used in this dissertation.

Total scattering is a sum of Bragg and diffuse scattering. The use of total scattering can provide insights into not only the long range average structure of a crystalline solid, but also the medium-to-local structures. A particular useful technique in analyzing total scattering data is the pair distribution function analysis (PDF), which will be discussed in detail in later section. The measurements of total scattering and Bragg scattering are in many ways similar. A notable difference is that data with high counting statistics at very low d spacing (or very high momentum transfer Q) is essential for a total scattering measurement, while the $\Delta d/d$ resolution (the sharpness of the peaks) that is important in Bragg scattering is less of importance in total scattering measurements.

1.4.1 Powder diffraction

When high quality single crystals are available, single crystal diffraction is undisputedly the best technique for structural determination of an unknown compound. With the aid of modern computation, the structural solution can be obtained even within minutes for moderately complex compounds. However, the most difficult step in a successful single crystal diffraction measurement is obtaining a high quality single crystal. When single crystals are not accessible, which is often the case, powder diffraction renders a unique opportunity to characterize the structure of crystalline solids.

Powder diffractometers are currently routine laboratory instruments. With the advance of X-ray detector technology, high quality X-ray diffraction patterns can be obtained within a few hours by a laboratory X-ray diffractometer. The development of high flux, high resolution synchrotron beamlines offers the possibility to even refine structures of biologically important macromolecules. Moreover, the recent emergence of spallation neutron sources around the globe significantly reduced the data collection time of neutron powder diffraction measurements. The obtained powder diffraction data can serve as an invaluable source for not only phase identification and structural refinement, but also *ab initio* structural determination (discussed in later sections).

The challenge of powder diffraction is manifested in the fact that 3-dimentional (3D) information (single crystal diffraction samples the 3D reciprocal lattice) is collapsed into 1D in powder diffraction. An appealing analogy of the information collapse in powder diffraction was made in the book of *Basic Solid State Chemistry*, where West described it as overlapping the complete contents of a book with many pages onto a single page. The primary challenge of

analyzing powder diffraction data is then readily seen, that is, how to separate the overlapping information.

1.4.2 Rietveld analysis of powder diffraction data

A milestone in the analysis of powder diffraction data is the birth of Rietveld refinement [28], which is named after the father of this method, the Dutch crystallographer Hugo Rietveld. Traditionally, structural refinement was carried out through comparisons of the observed integrated intensities of certain reflections with the ones that are calculated based on specific structural models. This method significantly limits the use of powder diffraction data in structural analysis, due to the overlapping peak issues discussed earlier. The Rietveld method takes a different approach in extracting reflection intensities. Instead of taking integrated intensity as a single data point, it minimizes the difference between the calculated and the observed intensities of each step (*i.e.*, each profile point) by assigning peak profiles to every reflection (either Gaussian, Lorentzian or a combination thereof). Detailed structural information, such as atomic positions, occupancies and thermal parameters can be obtained in this way, although a good starting structural model is a necessity. This method of structural analysis plays a central role in modern structural characterizations, and is frequently utilized in this dissertation.

1.4.3 Other tools to analyze Bragg scattering

This section aims to introduce the basic concepts of *ab initio* structural determination from powder diffraction data, and maximum entropy method (MEM) in acquiring high-resolution electron or nuclei density maps.

Although different approaches can be taken in pursuing a structural solution from powder diffraction data, the steps toward a final structural solution are in general the same: (1) data collection, (2) determination of the lattice type, (3) extraction of reflection intensities, (4) determination of the space group, (5) structural solution to produce an initial structural model and (6) final optimization of the structural model *via* Rietveld refinement. A particular important step is data collection, since it provides the foundation for all subsequent work. This highlights the importance of obtaining a high quality powder sample (*e.g.*, highly crystalline and preferably single phase) and the best possible diffraction data (often involves the use of synchrotron and/or neutron sources). The assignment of lattice type and space group is often not easy, and requires experience and trial-and-error. Once the space group is determined, structural solution can be attempted in different ways. Two relevant approaches that have been adopted in this dissertation, *i.e.*, simulated annealing and charge flipping.

Simulated annealing is a direct space approach (*i.e.*, real space approach). Similar to Rietveld refinement, it probes the parameter space according to a χ^2 statistics. Typically, a trial structure model will be constructed first by randomly positioning the atoms, based on the specified unit cell contents and space group information. After comparing with the observations (*i.e.*, the diffraction data), structural parameters will be adjusted in such a way that minimizes the difference between the calculated and observed diffraction profiles. However, it should be noted

that structural models which gives a larger difference is also accepted according to certain probabilities, to prevent the solution from trapping in local minima. There are various techniques that can be used to facilitate the structural solution process, *i.e.*, finding the global minima, such as bond-length restraints, implementation of rigid bodies, and the use of other penalties. Interested reader can consult Ref 29 for detail.

Charge flipping [30], on the other hand, is a dual space approach, meaning it operates on both real and reciprocal spaces. This method is not as computationally efficient as direct space approaches, such as simulated annealing. However, it does not require space group information (the solution carries out in P1) and is extremely simple as only one parameter needs to be specified (*i.e.*, η). It works in the manner of Fourier recycling, since the real space of a crystal structure is a unitary mapping of the reciprocal space (*i.e.*, reflection space) with the two spaces related by Fourier and inverse Fourier transform. This algorithm starts with assigning random phases (from 0 to 2π) to the observed structure factors while keeping the observed structure factor moduli (square root of the observed intensity) unaltered. All unobserved structural factors are assigned to be zero. An inverse Fourier transform was then performed to obtain the real space electron densities that are distributed onto a user-defined 3D grid. Then, the only parameter, η, needed in this algorithm comes into play. This parameter defines a threshold under which the signs of electron densities will be flipped (the so-called "charge flipping"). The modified electron densities are subsequently Fourier transformed to form a different set of structure factors (moduli and phases are both modified). The observed structure moduli are then substituted for those calculated from the trial electron densities without modifying the phases. A single iteration cycle is completed by generating a new trial electron density map through inverse Fourier transform of

the modified structure factors. A structure solution is considered to be found when a convergence of the total electron densities is met.

Another useful technique in analyzing Bragg diffraction data is the MEM analysis. Rooted in Bayesian statistics, MEM has been a useful tool in reconstruction of electron/nuclear density maps from the analysis of diffraction data for a variety of materials. It permits the visualization of spatial distribution of electron/nuclear densities, and thus the diffusion pathway to be inferred [31]. The use of MEM can produce better resolution electron/nuclear density maps ,and which are not limited to Gaussian probability distribution (in contrast to the routinely used Fourier synthesis). The latter advantage is critical for studies of ion diffusion. However, caution should be taken in interpretation of the MEM results, since MEM maps tend to exhibit spurious details when inappropriately used. Complimentary techniques are therefore needed to test the accuracy of MEM derived density maps.

1.4.4 Pair distribution function analysis of total scattering data

Pair distribution function (PDF), G(*r*), is a function of distance r in real space. It measures the scattering power weighted probability of finding an atom at a specific distance *r*. PDF pattern is derived from total scattering data, which accurately measures the Bragg as well as diffuse scattering components. Of note is that diffuse scattering can also arise from other background contribution rather than the sample itself. PDF data collection, therefore, requires a precise measurement of the background contribution. Many excellent reviews about PDF are available. Interested readers can refer to Ref 32 and 33 for details.

As an example to better illustrate the general principle about PDF, Figure 1.9 shows a PDF pattern of Ni with face-centered cubic structure. This data was collected at the beamline NOMAD of the Spllation Neutron Source at Oak Ridge National Lab, with the use of a time-of-flight neutron source. The distance at which a peak appears corresponds to a Ni-Ni correlation in this structure. The integrated intensity is a weighted bond length contribution, *i.e.*, proportional to the coordination number weighted by the scattering power of the atomic pair. The peak shape is Gaussian, and reflects thermal vibrations as well as the instrument resolution.

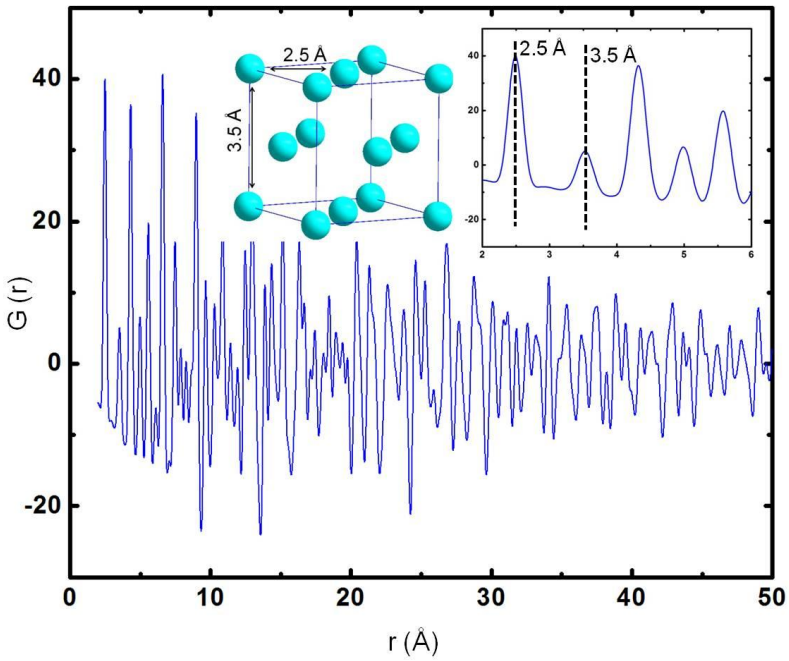

Figure 1.9. Neutron PDF pattern of a Ni sample from 0 to 50 Å. Inset shows the face-centered cubic structure of Ni and an enlarged PDF pattern from 2 to 6 Å. The first peak at 2.5 Å corresponds to the first coordination shell of Ni with a coordination number of 12. The second peak at 3.5 Å corresponds to the second coordination shell of Ni with a coordination number of 6. The two peaks should therefore have an integrated peak intensity ratio of 2:1 (*i.e.*, 12:6).

PDF data can be analyzed in different ways. The most straightforward technique is small-box modeling, with the use of one or a few unit cells [34]. This method works similarly as Rietveld refinement in Bragg scattering, and is used in this dissertation. The counterpart of small box modeling, *i.e.*, large-box modeling, can be also employed to analyze PDF data. This method is often coupled with the use of Reversed Monte Carlo technique [35], where a large supercell is built and relaxed to minimize χ^2 with respect to the experimental data.

1.4 Solid state NMR

Solid state NMR is widely used to probe the local structure of both crystalline and amorphous materials. Solid state NMR spectra almost always exhibit broad peaks due to the presence of anisotropic spin interactions, such as chemical shielding, dipolar coupling and quadrupole coupling. This is in stark contrast to its liquid counterpart, where sharp peaks are often present as the rapid tumbling of molecules in liquid averages all the aforementioned anisotropic interactions to zero. The substantial anisotropy in solid state NMR, on one hand, complicates the analysis of NMR data. On the other hand, it provides valuable insights into the local environment of target nuclei. Therefore, manipulating these spin interactions, or, switching them on and off in a controlled manner is essential to gain useful information from solid state NMR measurements [36].

1.4.1 NMR of paramagnetic materials

One particularly important interaction worth discussing in further detail in this dissertation is paramagnetic interactions, since most battery materials contain transition metals as redox centers and are paramagnetic either in the pristine state or at charged or discharged states. These paramagnetic interactions can often produce NMR shifts that go far beyond the typical shift range for diamagnetic materials. For instance, the ^{7}Li hyperfine shift for Li in $LiFeBO_3$ is at -233 ppm while Li in most diamagnetic materials resonates at around 0 ppm. The dipolar interactions between target nuclei with unpaired electrons also significantly broaden the NMR spectra, making it difficult to resolve isotropic peaks. However, valuable structural information is often embedded in such paramagnetic interactions, as these NMR interactions are very sensitive to the electronic structure of the materials. It is often straightforward to distinguish between target nuclei containing in diagmagnetic materials and paramagnetic materials [37].

Paramagnetic interactions are often composed of two parts, *i.e.*, the through bond interaction (Fermi-contact) and the through space interaction (dipolar). The Fermi-contact interaction occurs through electron density transfer from the paramagnetic centers to the target nuclei (^{7}Li in ^{7}Li NMR), either directly or indirectly through intervening bonding atoms (such as O). This interaction is, therefore, sensitive to the bonding environment of the NMR target nuclei (such is Li-O-metal bonding distances and angles). The through space dipolar interaction occurs between the NMR target nuclei (such as Li) and the time-averaged magnetic moment produced by the unpaired electrons associated with the paramagnetic centers. When only isotropic magnetic moment is concerned, this dipolar interaction produces a large anisotropy that can be described by a second-order tensor (similar to chemical shift anisotropy), but with no overall shift. The anisotropy can be averaged by magic angle spinning as will be discussed in later

section. If magnetic anisotropy is present (often due to the asymmetry of orbital configurations), an overall shift (pseudo-contact shift) will be produced as well as a large anisotropy. This anisotropy, however, cannot be removed by magic angle spinning.

1.4.2 Magic angle spinning (MAS) NMR

MAS NMR is currently a routine technique to achieve high resolution NMR spectra by removing or partially removing the large anisotropy caused by chemical shift interaction, dipolar coupling and quadrupole coupling. A typical MAS NMR experiment typically involves the rapid spinning of the sample in a rotor about a spinning axis of $54.57°$ (the so-called "magic angle") with respect to the applied magnetic field. The underlying principle is that all the aforementioned anisotropic interactions are angular dependent with a form of $3\cos^2\theta - 1$ (to a first order approximation). when spinning at the magic angle, $3\cos^2 54.57° - 1$ goes to zero and the anisotropic interactions vanish. The effect of MAS is readily seen in Figure 1.10, where the static and MAS NMR ^{7}Li NMR spectra of $LiFeBO_3$ are compared. The MAS NMR spectrum is characterized by an isotropic peak and several spinning side bands due to the incomplete averaging of the anisotropy under MAS. The separation between spinning side bands, and between spinning side band and the isotropic peak is governed by the spinning speed. These spinning sidesbands can be in principle completely removed when the spinning speed exceeds the overall anisotropy of all the present NMR interactions. However, due to instrument limitation, modern equipment can only spin up to 50-100 kHz. The fact that many quadrople and paramagnetic interaction are on the scale of MHz or hundreds of kHz makes the complete removal of spinning side bands an impossible task. When multiple resonances are present,

resolving isotropic peaks becomes increasingly difficult. This motivates the use of other spinning sideband removal pulse sequence, such as pjMATPSS [38] (see discussion in later chapter), to improve the resolution of NMR spectra.

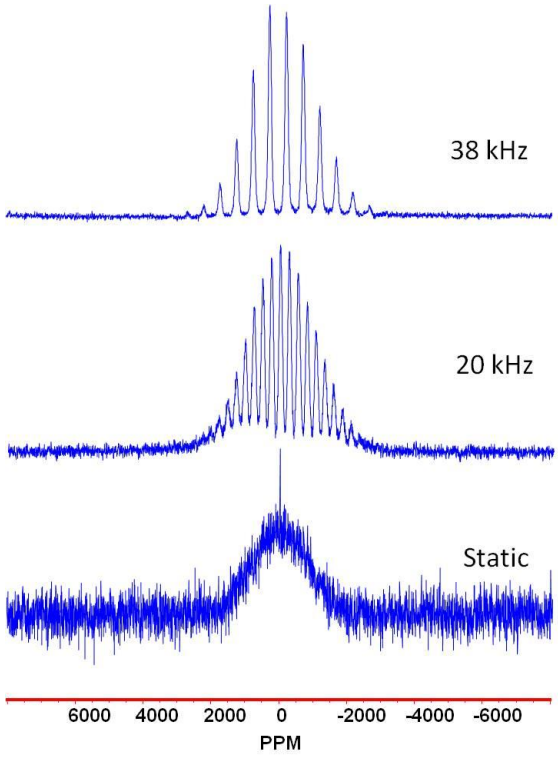

Figure 1.10. Comparison of ^{7}Li NMR spectra of $LiFeBO_3$ that were collected under static, under spinning conditions. While the static spectrum is characterized by the presence of a broad and featureless peak, with increasing spinning speed, higher resolution spectra can be obtained which clearly separate the isotropic peak from spinning side band manifolds.

1.5 References

1. Richter, B.; Goldston, D.; Crabtree, G.; Glicksman, L.; Goldstein, D.; Greene, D.; Kammen, D.; Levine, M.; Lubell, M.; Savitz, M.; Sperling, D.; Schlachter, F.; Scofield, J.; Dawson, J., How America can look within to achieve energy security and reduce global warming. *Rev Mod Phys* **2008,** *80* (4), S1-S107.

2. Tarascon, J. M.; Armand, M., Issues and challenges facing rechargeable lithium batteries. *Nature* **2001,** *414* (6861), 359-367.

3. Bruce, P. G.; Scrosati, B.; Tarascon, J. M., Nanomaterials for rechargeable lithium batteries. *Angew Chem Int Edit* **2008,** *47* (16), 2930-2946.

4. Barbalace, K., http://environmentalchemistry.com/yogi/periodic/.

5. Haxel, G. B.; Hedrick, J. B.; Orris, G. J., USGS Fact Sheet 087-02, 2002.

6. Mizushima, K.; Jones, P. C.; Wiseman, P. J.; Goodenough, J. B., Li_xCoO_2 "(0<x<1) - a New Cathode Material for Batteries of High-Energy Density. *Mater Res Bull* **1980,** *15* (6), 783-789.

7. Padhi, A. K.; Nanjundaswamy, K. S.; Goodenough, J. B., Phospho-olivines as positive-electrode materials for rechargeable lithium batteries. *J Electrochem Soc* **1997,** *144* (4), 1188-1194.

8. Shannon, R. D., Revised Effective Ionic-Radii and Systematic Studies of Interatomic Distances in Halides and Chalcogenides. *Acta Crystallogr A* **1976,** *32* (Sep1), 751-767.

9. Reimers, J. N.; Dahn, J. R., Electrochemical and In Situ X-Ray Diffraction Studies of Lithium Intercalation in Li_xCoO_2. *J Electrochem Soc* **1992,** *139* (8), 2091-2097.

10. Yang, X. Q.; Sun, X.; McBreen, J., New phases and phase transitions observed in $Li_{1-x}CoO_2$ during charge: in situ synchrotron X-ray diffraction studies. *Electrochem Commun* **2000,** *2* (2), 100-103.

11. Amatucci, G. G.; Tarascon, J. M.; Klein, L. C., Cobalt dissolution in $LiCoO_2$-based non-aqueous rechargeable batteries. *Solid State Ionics* **1996,** *83* (1–2), 167-173.

12. Islam, M. S.; Driscoll, D. J.; Fisher, C. A. J.; Slater, P. R., Atomic-scale investigation of defects, dopants, and lithium transport in the $LiFePO_4$ olivine-type battery material. *Chem Mater* **2005,** *17* (20), 5085-5092.

13. Janssen, Y.; Santhanagopalan, D.; Qian, D. N.; Chi, M. F.; Wang, X. P.; Hoffmann, C.; Meng, Y. S.; Khalifah, P. G., Reciprocal Salt Flux Growth of $LiFePO_4$ Single Crystals with Controlled Defect Concentrations. *Chem Mater* **2013,** *25* (22), 4574-4584.

14. Malik, R.; Burch, D.; Bazant, M.; Ceder, G., Particle Size Dependence of the Ionic Diffusivity. *Nano Lett* **2010,** *10* (10), 4123-4127.

15. Huang, H.; Yin, S.-C.; Nazar, L. F., Approaching Theoretical Capacity of $LiFePO_4$ at Room Temperature at High Rates. *Electrochemical and Solid-State Letters* **2001,** *4* (10), A170-A172.

16. Yamada, A.; Chung, S. C.; Hinokuma , K., Optimized $LiFePO_4$ for Lithium Battery Cathodes. *J Electrochem Soc* **2001,** *148* (3), A224-A229.

17. Chung, S.-Y.; Bloking, J. T.; Chiang, Y.-M., Electronically conductive phospho-olivines as lithium storage electrodes. *Nat Mater* **2002,** *1* (2), 123-128.

18. Padhi, A. K.; Nanjundaswamy, K. S.; Masquelier, C.; Okada, S.; Goodenough, J. B., Effect of Structure on the Fe^{3+}/Fe^{2+} Redox Couple in Iron Phosphates. *J Electrochem Soc* **1997,** *144* (5), 1609-1613.

19. Padhi, A. K., Mapping Redox Energies of Electrode Materials for Lithium Batteries. Thesis. The University of Texas at Austin, 1997.

20. Nytén, A.; Abouimrane, A.; Armand, M.; Gustafsson, T.; Thomas, J. O., Electrochemical performance of Li_2FeSiO_4 as a new Li-battery cathode material. *Electrochem Commun* **2005,** *7* (2), 156-160.

21. Dominko, R.; Bele, M.; Gaberscek, M.; Meden, A.; Remskar, M.; Jamnik, J., Structure and electrochemical performance of Li_2MnSiO_4 and Li_2FeSiO_4 as potential Li-battery cathode materials. *Electrochem Commun* **2006,** *8* (2), 217-222.

22. Nishimura, S.-i.; Hayase, S.; Kanno, R.; Yashima, M.; Nakayama, N.; Yamada, A., Structure of Li_2FeSiO_4. *J Am Chem Soc* **2008,** *130* (40), 13212-13213.

23. Kokalj, A.; Dominko, R.; Mali, G.; Meden, A.; Gaberscek, M.; Jamnik, J., Beyond One-Electron Reaction in Li Cathode Materials: Designing $Li_2Mn_xFe_{1-x}SiO_4$. *Chem Mater* **2007,** *19* (15), 3633-3640.

24. Gong, Z. L.; Li, Y. X.; Yang, Y., Synthesis and Characterization of $Li_2Mn_xFe_{1-x}SiO_4$ as a Cathode Material for Lithium-Ion Batteries. *Electrochemical and Solid-State Letters* **2006,** *9* (12), A542-A544.

25. Aravindan, V.; Karthikeyan, K.; Ravi, S.; Amaresh, S.; Kim, W. S.; Lee, Y. S., Adipic acid assisted sol-gel synthesis of Li_2MnSiO_4 nanoparticles with improved lithium storage properties. *J Mater Chem* **2010,** *20* (35), 7340-7343.

26. Ellis, B. L.; Makahnouk, W. R. M.; Makimura, Y.; Toghill, K.; Nazar, L. F., A multifunctional 3.5V iron-based phosphate cathode for rechargeable batteries. *Nat Mater* **2007,** *6* (10), 749-753.

27. Recham, N.; Chotard, J. N.; Dupont, L.; Delacourt, C.; Walker, W.; Armand, M.; Tarascon, J. M., A 3.6V lithium-based fluorosulphate insertion positive electrode for lithium-ion batteries. *Nat Mater* **2010,** *9* (1), 68-74.

28. Rietveld, H., A profile refinement method for nuclear and magnetic structures. *J Appl Crystallogr* **1969,** *2* (2), 65-71.

29. Bruker, TOPAS Technical Reference.

30. Oszlanyi, G.; Suto, A., Ab initio structure solution by charge flipping. *Acta Crystallogr A* **2004,** *60* (2), 134-141.

31. Gilmore, C. J., Maximum entropy and Bayesian statistics in crystallography: A review of practical applications. *Acta Crystallogr A* **1996,** *52*, 561-589.

32. Proffen, T.; Kim, H., Advances in total scattering analysis. *J Mater Chem* **2009,** *19* (29), 5078-5088.

33. Egami, T.; Billinge, S. J. L., Underneath the Bragg peaks: structural analysis of complex materials, Pergamon, Amsterdam; Boston,. **2003**.

34. Farrow, C. L.; Juhas, P.; Liu, J. W.; Bryndin, D.; Božin, E. S.; Bloch, J.; Th, P.; Billinge, S. J. L., PDFfit2 and PDFgui: computer programs for studying nanostructure in crystals. *Journal of Physics: Condensed Matter* **2007,** *19* (33), 335219.

35. Keen, D. A.; Tucker, M. G.; Dove, M. T., Reverse Monte Carlo modelling of crystalline disorder. *Journal of Physics: Condensed Matter* **2005,** *17* (5), S15.

36. Duer, M. J., Solid-State NMR Spectroscopy Principles and Applications, Wiley-Blackwell; 1 edition (December 21, 2001).

37. Grey, C. P.; Dupré, N., NMR Studies of Cathode Materials for Lithium-Ion Rechargeable Batteries. *Chem Rev* **2004,** *104* (10), 4493-4512.

38. Hung, I.; Zhou, L.; Pourpoint, F.; Grey, C. P.; Gan, Z., Isotropic High Field NMR Spectra of Li-Ion Battery Materials with Anisotropy >1 MHz. *J Am Chem Soc* **2012,** *134* (4), 1898-1901.

Chapter 2

Degradation and (de)lithiation processes in the high capacity battery material $LiFeBO_3$[1]

2.1 Introduction

$LiFePO_4$ is one of the more promising cathode candidates for Li-ion battery applications, because of its inexpensive constituents and "safe" operating voltage. However, its lower energy density relative to other competing technologies such as $LiNi_{1/3}Mn_{1/3}Co_{1/3}O_2$ has driven research efforts to find "safe" cathode materials that operate below about 4.1 V with high capacities. $LiFeBO_3$ is a possible alternative to $LiFePO_4$ because of its larger theoretical capacity (220 *vs*. 170 mAh/g for $LiFePO_4$). A number of attempts have been made to access its theoretical capacity with a greatly varying degree of success since it was first proposed as cathode material for lithium-ion batteries in 2001.[2]

Prior structural studies on $LiFeBO_3$ have determined that the structure is monoclinic with a space group of *C2/c* and contains trigonal planar BO_3 building blocks, as shown in Figure 2.1[2b]. Both Li and Fe cations were reported to adopt an asymmetric trigonal bipyramidal coordination geometry, in which the central atoms are shifted off-center giving two partially occupied split sites rather than a single fully occupied site. The oxygen atoms in this structure adopt a distorted hexagonal close packed (*hcp*) array. The FeO_5 trigonal bipyramids are edge-shared along the [10-1] direction, providing the primary pathway for electronic transport. The LiO_5 polyhedra in this structure are edge-shared and run along the [001] direction. Based on the observed crystal structure and electronic structure calculations performed by Seo and coworkers, the most probable Li diffusion pathway is the channel in this [001] direction[2c]. We have recently

redetermined the structure of this material using single crystal diffraction methods and found that the structure of $LiFeBO_3$ is in fact commensurately modulated [3]. The modulation results in a tetrahedral coordination environment for Li. This and earlier structural determinations suggest that $LiFeBO_3$ is a 1D ionic conductor with electronic conductivity that is similar to its olivine counterpart $LiFePO_4$, *i.e.*, low. From this, it can be inferred that nanostructuring and carbon-coating may be required to obtain good electrochemical performance.

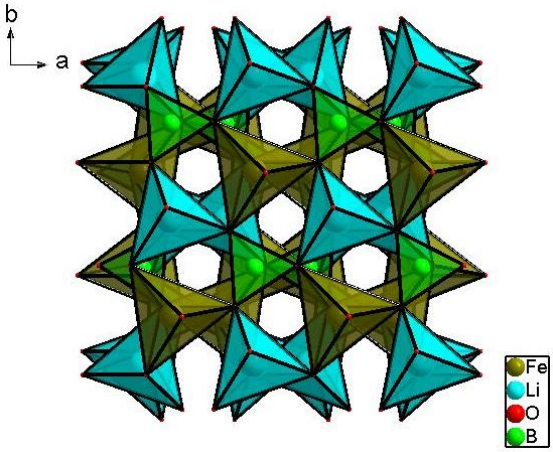

Figure 2.1. Crystal structure of monoclinic $LiFeBO_3$ with space group of *C2/c* viewed along [001] direction to emphasize the pseudo-trigonal symmetry in the planar layers of BO_3 triangles, FeO_5 trigonal bipyramids, and LiO_5 trigonal bipyramids. Figure is reproduced with permission from Ref 1.

Accessing the large theoretical specific capacity of $LiFeBO_3$ has not been a trivial exercise. The electrochemical performance of $LiFeBO_3$ was first investigated in 2001 with a reported capacity of less than 10 mAh/g under an extremely low rate (C/250)[2b]. When the material was revisited by Dong and coworkers, carbon coating was employed to facilitate the

electronic transport during cycling[2a]. Even though they were able to achieve a better electrochemical performance in terms of the observed capacity (150 mAh/g), a large polarization was observed and only 60 mAh/g were delivered below 4.5 V on charging. Very recently, Yamada and coworkers achieved a large reversible capacity of approximately 190 mAh/g by carefully preparing electrode samples under an inert Ar atmosphere[2d]. They attributed the performance improvement to the prevention of air exposure and the minimization of material degradation. In their work, it was convincingly demonstrated, by Mössbauer spectroscopy that Fe (II) was mostly oxidized to Fe (III) after prolonged air exposure, especially at elevated temperature. However, the underlying mechanism of degradation and capacity loss remains unclear and a method for improving the performance of this promising material at high rates is still desired. A thorough understanding of the degradation issue will be a crucial step towards minimizing degradation and improving battery performance. $LiFeBO_3$ and its substituted variants could be excellent cathode candidates for the next generation of lithium-ion batteries if such performance enhancements are realized.

Oxidation or degradation of electrode materials, and in particular nanomaterials, by moisture attack at ambient conditions or moderately high temperature has been well documented in the literature. One notable example is the vulnerability of nano-$LiFePO_4$ to moisture attack[4]. The degradation of Fe^{2+}-containing materials upon air exposure generally involves both delithiation and oxidation of Fe^{2+}. Also, the impurity phases generated upon air exposure such as LiOH and/or Li_2CO_3, can in many cases cover the surfaces of the pristine particles in a manner that can harm their electrochemical performance.

X-ray diffraction (XRD) techniques are widely used to characterize the structural evolutions of the battery materials during the process of degradation. However, X-ray methods

are not very sensitive to changes that involve light elements such as Li, B and O. Neither are they sensitive to the formation of amorphous components. Nuclear magnetic resonance (NMR) is a probe that is particularly sensitive to the local environment of target nuclei and is not limited to the characterizations of crystalline materials[5]. In addition, electron energy-loss spectroscopy implemented in the transmission electron microscope (TEM-EELS) enables maps of the spatial distribution of the main constituents in samples and allows their valence states to be determined[6]. To complement laboratory and synchrotron XRD studies of this system, we have carried out detailed structural analyses using ^{7}Li solid state NMR, electron microscopy, TEM-EELS and X-ray absorption spectroscopy (XAS) techniques for a variety of $LiFeBO_3$ preparations with different particle sizes. The structural and chemical information obtained in the measurements were analyzed in the context of the electrochemical performance of these samples. We discuss the particle-size dependence of degradation, likely products of the degradation, and a suggested mechanism for the degradation of $LiFeBO_3$. An optimized electrode preparation method was developed based on our understanding of the degradation process of $LiFeBO_3$ upon air exposure. The (de)lithiation processes of $LiFeBO_3$ were then investigated by galvanostatic cycling and galvanostatic intermittent titration techniques (GITT).

2.2 Experimental

Synthesis: $LiFeBO_3$ was prepared through the solid-state reaction of precursors under an actively reducing atmosphere of forming gas (5% H_2/95% N_2). In a typical synthesis of carbon-free ceramic $LiFeBO_3$, 3g of the powders precursors of $LiBO_2$ (pre-dried) and $FeC_2O_4 \cdot 2H_2O$ were combined in a stoichiometric ratio and ball milled for 30 minutes in a SPEX

SamplePrep8000 Mixer/Mill high-energy ball mill. The resulting fine powders were then put into a graphite crucible and transferred into a tube furnace, which was sealed and purged with N_2. Following calcination at 350 ℃ for 10 hours to decompose FeC_2O_4 $2H_2O$ and remove moisture, the reaction temperature was ramped up to 650 ℃ for 20 hours under a heating rate of 100 ℃/h. After the furnace was cooled to room temperature, the reaction products were removed from the furnace and immediately transferred to and stored in an argon glove box until the time of their characterization. A second synthesis route was utilized to produce a carbon coating that reduced particle size. This $LiFeBO_3$/C synthesis differed only in the reaction precursors, which were Li_2CO_3, $FeC_2O_4{\cdot}2H_2O$ and H_3BO_3 to which citric acid was added as the carbon source. Two sets of samples were prepared with targeted carbon contents of 10 wt% and 20 wt%, with the amount of added citric acid calculated based on the assumption that pure carbon is formed with a 100% yield.

Characterization: Room temperature powder XRD data were measured using a Bruker D8 diffractometer with Cu K_α radiation, a 300 nm working radius and a 192 channel LynxEye detector whose energy window settings (lower level of 0.19 V, window width of 0.06 V) were set to minimize the influence of iron fluorescence on the collected data within the modest energy resolution of the detector (25%). Synchrotron XRD data was collected at beamline 11-BM of the Advanced Photon Source with a constant wavelength of approximately 0.41 Å with samples first loaded and sealed into a 0.5 mm diameter glass capillary and then secured in a secondary Kapton capillary. Variable-temperature *in situ* XRD experiments were performed on a Rigaku Ultima-IV diffractometer equipped with a heating stage and a 128 channel X-ray detector capable of energy discrimination[7]. Rietveld refinement was performed with the Topas software package, version 4.2 (Bruker AXS).

In the ^{7}Li MAS NMR experiments, a 1.8 mm HX probe was employed on Chemagnetics-200MHz spectrometer with a 4.7 T magnetic field. A rotor-synchronized spin echo sequence ($\pi/2$-τ-π-τ-acquisition) was utilized. The operating frequency was 77.71 MHz and the pulse width was 2.75 μs ($\pi/2$). A recycle delay of 0.1 s was used. The external reference was 1 M LiCl set at 0 ppm.

X-ray absorption spectroscopy (XAS) data on the Fe-*K* edge were collected at the X18A and X19A beamlines of the National Synchrotron Light Source (NSLS) using a Si(111) double-crystal monochromator in transmission mode. The beam intensity was reduced by 30% to minimize the high order harmonics. Reference spectra (Fe metallic foil) for the energy calibration were collected simultaneously with all of the sample spectra . The X-ray absorption near edge structure (XANES) and extended X-ray absorption fine structure (EXAFS) spectra were processed using the Athena software package[8]. The AUTOBK code was used to normalize the absorption coefficient, and separate the EXAFS signal, $\chi(k)$, from the isolated atom absorption background. The extracted EXAFS signal, $\chi(k)$, was weighted by k^3 to emphasize the high-energy oscillations and then Fourier-transformed in a *k*-range from 3.0 ~ 11.0 Å^{-1} using a Hanning window with a window sill (Δk) of 2.0 Å^{-1} to obtain magnitude plots of the EXAFS spectra in *R*-space (Å).

TEM images and EELS spectra were recorded at 200 kV in a JEOL2100F microscope equipped with a Gatan image filter (GIF) spectrometer whose energy resolution is about 1.1 eV, as judged by the FWHM of the zero-loss peak (ZLP). Spectra were recorded in both scanning TEM (STEM) mode for local analysis and electron diffraction (ED) for average information. Energy filtered TEM images were recorded at 300 kV using a FEI Titan TEM, also equipped with GIF spectrometer. Compositional analysis was obtained through integrating intensities of

the O *K* edge and Fe L_3 edge EELS responses after background subtraction, which were recorded simultaneously as a ~1 nm beam was step-scanned across the sample in the STEM mode of operation, with a step increment of 1.5 nm. The information about the valence state of iron is encoded in the near-edge fine structure of the edge peaks, whose onsets were around 536 eV (O *K* edge) and 706 eV (Fe L_3 edge).

Electrochemical testing was done in a 2032 type coin cell using an Arbin battery cycler. The electrolyte was 1 M $LiPF_6$ in a 1:1 volumetric mixture of anhydrous ethylene carbonate (EC) and anhydrous dimethyl carbonate (DMC). For standard $LiFeBO_3$ cathode preparations, 70 wt% of active material, 20 wt% of Super P and 10 wt% of polyvinylidenedifluoride (PVDF) were mixed and ground thoroughly with 1-methyl-2-pyrrolidone (NMP) in an Ar glove box. The slurry was cast onto an Al foil and then dried in a vacuum oven overnight at 60 ℃. Circular disks with a diameter of approximately 14 mm were punched with a loading of *ca.* 2-3 mg of electrode materials. In the optimized preparation of electrodes for galvanostatic cycling experiments, Super P, PVDF and NMP were dried before use. The cut-off voltage was 4.7 V for charging and 1.3 V for discharging. For the galvanostatic intermittent titration (GITT) measurements, a series of current pulses were applied (1/50 C) to the assembled coin cells. The cells were then allowed to relax for a user-defined time after each current pulse.

2.3 Results and discussion

2.3.1 Synthesis and particle size control by carbon-coating

There are two primary challenges in the synthesis of highly pure $LiFeBO_3$. First, Li and B are both potentially volatile, and any Li and/or B loss during the synthesis can force the system

to off-stoichiometry. Second, Fe(II) is generally not a stable iron oxidation state in air at the synthesis temperatures of $LiFeBO_3$, and rigorous control of the oxygen partial pressure is therefore required to ensure that no other valence of iron is present in the product. For the synthesis of highly pure ceramic (carbon-free) $LiFeBO_3$, $LiBO_2$ was chosen as the Li and B source owing to its relatively high melting temperature (approximately 850 ℃) with respect to the synthesis temperature (650 ℃). An actively reducing atmosphere was chosen (5% H_2/95 % N_2) to drive the formation of Fe(II), regardless of the initial oxidation state of the Fe-containing precursor (typically $FeC_2O_4 \cdot 2H_2O$). Smaller particle sizes were targeted in a second set of syntheses using citric acid as the carbon source (nominally 10 wt% or 20 wt% C in the final product) to limit grain growth and enhance electronic transport in the battery electrode. Li_2CO_3, H_3BO_3 and $FeC_2O_4 \cdot 2H_2O$ were used as the precursors for these syntheses, which were typically carried out at the same temperature as for ceramic $LiFeBO_3$. Synchrotron XRD studies on representative samples were used to quantify the presence and prevalence of impurities (wt%) through Rietveld analysis, while SEM analysis were utilized to qualitatively assess particle size (Fig. 2.2). The average particle sizes of $LiFeBO_3$/C with nominally 10 wt% C and 20 wt% C are around 200 and 100 nm respectively (denoted as 200 nm $LiFeBO_3$/C and 100 nm $LiFeBO_3$/C for later discussion), both representing a substantial reduction from that of the native ceramic (2-3 μm) prepared at the same temperature. Both sets of $LiFeBO_3$/C samples contained a small minority of one micron (or larger) sized particles. All preparations contained from 3% to 10% of the Fe_3BO_5 impurity phase, the amount increasing noticeably for the sample with the smallest particle size. Fe_3BO_5 was also observed as the major impurity (~10%) in other reported syntheses[2d]. A preliminary TGA determination of the carbon content suggests that the particles contain at most 6.3 and 11.3 wt% carbon for the 200 nm and 100 nm $LiFeBO_3$ particles,

respectively. It is worth noting that partial oxidation of Fe prior to the TGA experiment would cause the true carbon content to be slightly lower than these values.

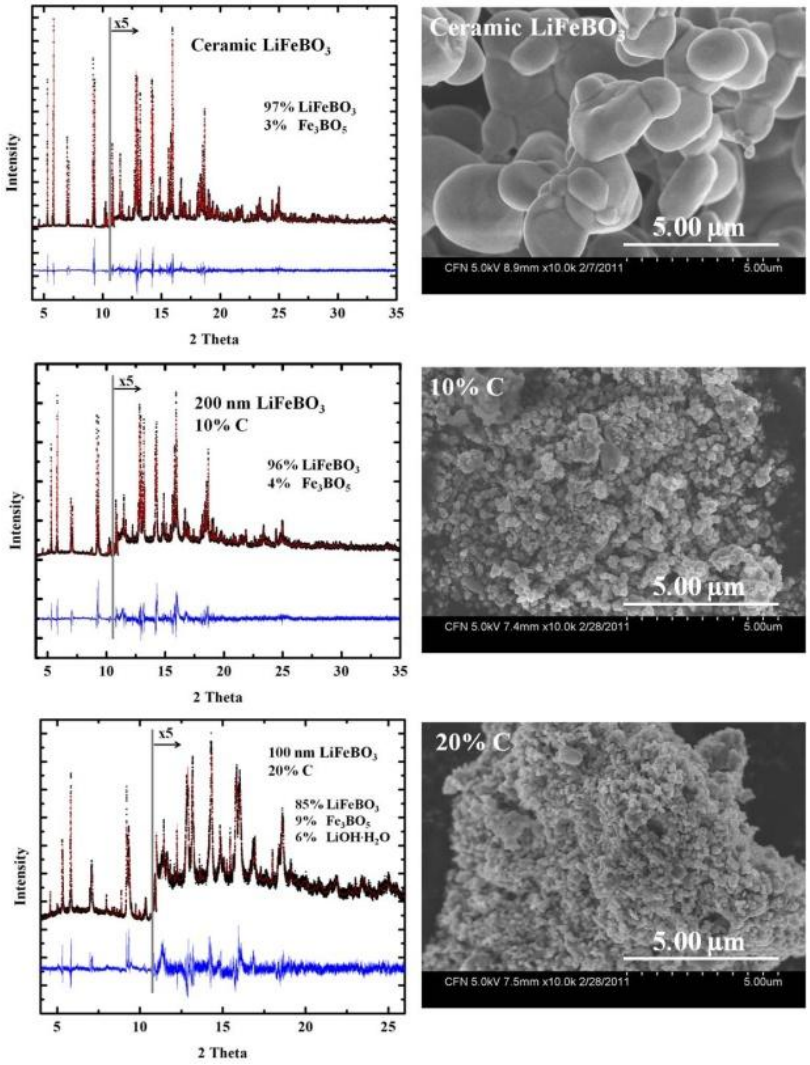

Figure 2.2. Rietveld refinements of the ceramic (carbon-free) $LiFeBO_3$ (top), 10% C $LiFeBO_3$/C (middle) and 20% C $LiFeBO_3$/C (bottom), and their corresponding SEM images on the right. Figure is reproduced with permission from Ref 1.

Further insights into particle size distribution and the nature of the carbon coating were

obtained by TEM and STEM imaging, as shown in Figure 2.3. For the 200 nm $LiFeBO_3$/C composite, a non-uniform size distribution is observed, typically ranging from 10 nm to 200 nm or even bigger (Fig. 2.3a). A thin layer of surface carbon coating, of about 2-3 nm, can be also discerned from high-resolution TEM (HRTEM) images (Fig. 2.3b). The surface carbon is mostly amorphous. The EELS elemental mapping highlights the distribution of carbon across a big area of the composite (Fig. 2.3c-f). Most of the particles were wrapped in the amorphous carbon, which is critically important for their electrochemical performance. The 100 nm $LiFeBO_3$/C composite is very similar to the 200 nm one, except that the particle size is smaller. A broad size distribution of particle sizes was also observed in TEM experiments, ranging from a few nanometers to more than 100 nm (Fig. 2.4).

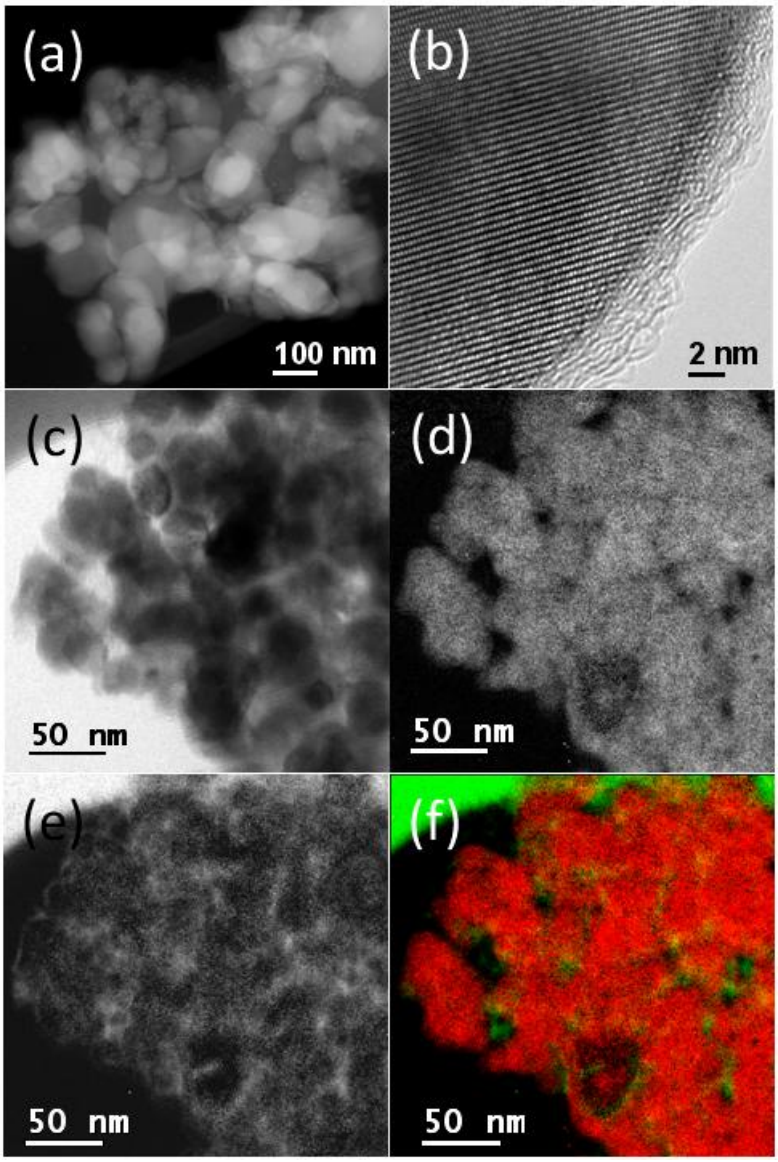

Figure 2.3. Morphology and surface carbon coating of the as-prepared $LiFeBO_3$ particles by (a) annular dark-field (ADF) STEM image; (b) high resolution TEM (HRTEM) image; (c) bright field (BF) TEM image; (d) Fe-$L_{2,3}$ image; (e) C-K image; (f) false colored compositional image with red color for Fe and green for C. Data was collected and analyzed in collaboration with Dr. Feng Wang from Brookhaven National Laboratory. Figure is reproduced with permission from Ref 1.

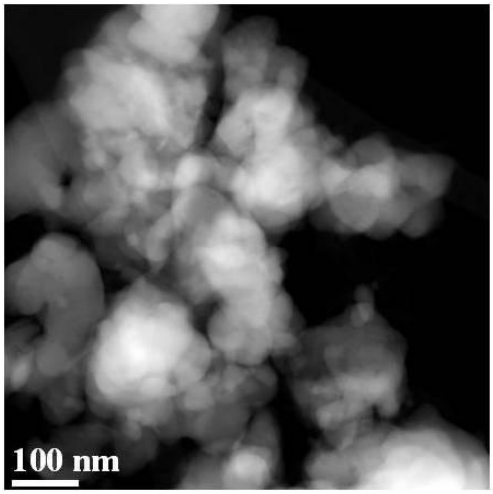

Figure 2.4. Micrograph of the 100 nm $LiFeBO_3$/C with approximately 20 wt% carbon by an Annular dark-field (ADF) STEM image. Data was collected and analyzed in collaboration with Dr. Feng Wang from Brookhaven National Laboratory. Figure is reproduced with permission from Ref 1.

2.3.2 Signatures of the $LiFeBO_3$ degradation

X-ray diffraction (XRD) experiments were used to track the cell parameter changes in $LiFeBO_3$ during degradation. Figure 2.5 shows the XRD patterns of the 200 nm $LiFeBO_3$/C composite after 1 – 6 days of air exposure at room temperature. Although the changes were very small, it was observed that the original reflections in several 2θ regions begin to merge after air exposure. A closer look at the Miller indices of these reflections reveals that it is the *hkl* and *hk-l* peaks that tend to merge together after extended air exposure. Considering that the pristine $LiFeBO_3$ phase has a monoclinic structure with $\beta = 91.39°$, it is likely that the degraded $LiFeBO_3$ phase possesses a higher symmetry (possibly orthorhombic) than that of the pristine one, whose

lattice parameters can equivalently be described by a $LiFeBO_3$-type monoclinic cell but with β = 90 °. Thus, *hkl* and *hk-l* peaks likely become symmetry equivalents in degraded $LiFeBO_3$. The change in symmetry is not a continuous one, as can be seen in the inset of Figure 2.5. The *112* and *11-2* peaks of the pristine monoclinic $LiFeBO_3$ decrease in intensity while the new peak from the degraded phase located in between increases in intensity, without any resolvable shifts in peak position during the conversion process even at this optimal position for monitoring the structural changes.

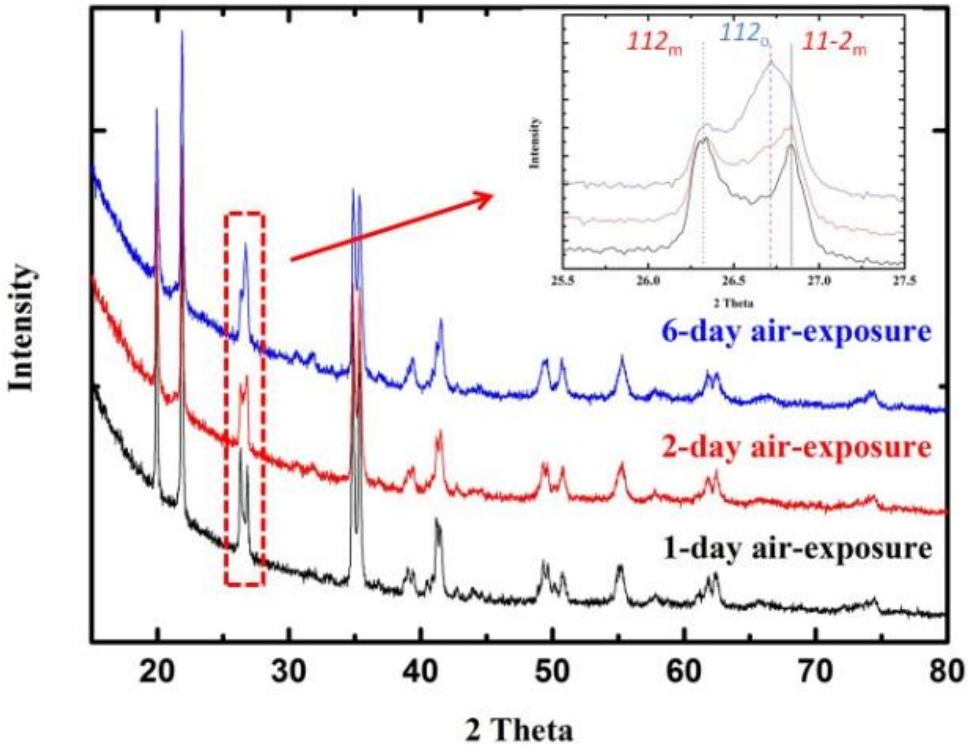

Figure 2.5. XRD patterns of 200 nm $LiFeBO_3$/C after 1-6 days of air exposure at room temperature. The inset highlights a new reflection that results from the degradation and which could be indexed as the *112* reflection (blue label) of a higher symmetry orthorhombic cell. An orthorhombic cell might result when the monoclinic β angle is decreased to 90°. The lack of

observable shifts in the $LiFeBO_3$ cell parameters of the original phase, as evidenced by the positions of *112* and *11-2* peaks (red labels) of its monoclinic lattice, indicates a discontinuous symmetry change during the $LiFeBO_3$ degradation. Figure is reproduced with permission from Ref 1.

This data clearly indicates that 200 nm $LiFeBO_3$ particles can be substantially degraded even at room temperature, and underscores the difficulty of accessing the intrinsic capacity of the nano-scale $LiFeBO_3$. Typical routes for preparing battery electrode films usually involves drying the electrode material at elevated temperature (100 ℃ or even higher) in air, conditions which would be expected to accelerate $LiFeBO_3$ degradation and result in a serious capacity loss even before the first cycle. Although X-ray diffraction clearly shows evidence for the formation of a degradation product with a crystal structure different than that of $LiFeBO_3$, there are limited opportunities for obtaining more detailed structural information from X-ray studies due to the weak X-ray peak intensities in these light-element phases and the high degree of peak-overlap between the X-ray peaks of the original and degraded phases.

The signature for $LiFeBO_3$ degradation is more direct in the ^7Li solid-state NMR experiments. The degradation during electrode preparation can be readily monitored by following the peak intensity of the Li signal due to Li loss from the structure. Lost Li cations no longer neighbor paramagnetic Fe ions, and therefore give a simple diamagnetic response with a 0 ppm chemical shift (Fig. 2.6). As-prepared ceramic $LiFeBO_3$ has a single resonance with an isotropic shift of -233 ppm, and is essentially free of diamagnetic Li. This large isotropic (Fermi-contact) shift is caused by a through-bond hyperfine interaction between the paramagnetic centers (Fe^{2+}) and the observed nuclei (^7Li), *via* the intervening oxygen atoms. All other

observed peaks are spinning side bands, which arise from partial averaging the dipolar coupling of Li nuclei to the unpaired electrons associated with Fe^{2+} by magic angle spinning (MAS). After ball milling with C under Ar protection, a weak resonance at around 0 ppm was observed from the creation of a Li-containing diamagnetic phase. The spectrum following mixing of the ball milled powder with NMP and PVDF in an Ar glove box and drying under vacuum at 60 ℃ overnight contains an even stronger resonance at 0 ppm, indicating that Li was lost from the framework of $LiFeBO_3$ during this method of preparing the cathode film.

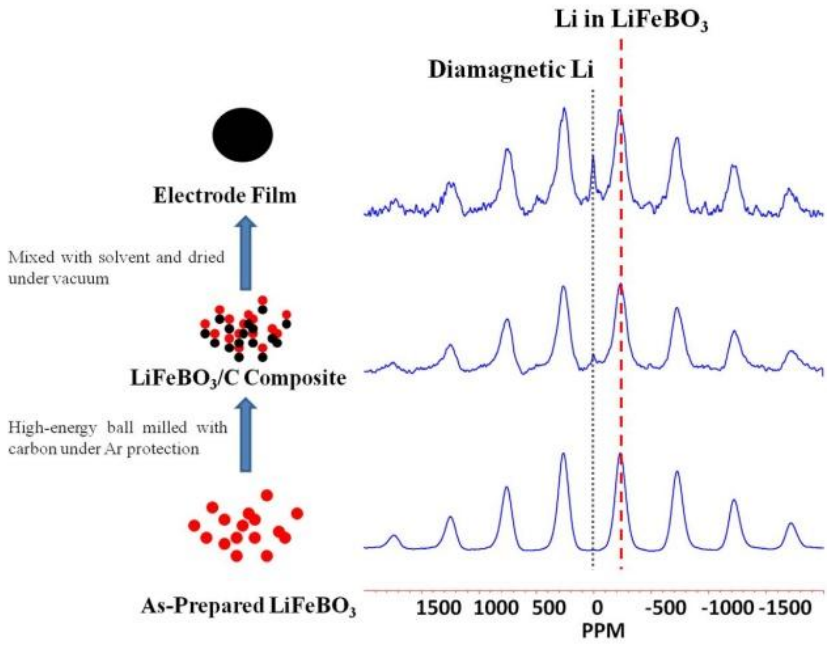

Figure 2.6. ^{7}Li MAS NMR spectra of the as-prepared ceramic $LiFeBO_3$, the $LiFeBO_3$/C mixture and the electrode film. The isotropic resonances are marked with dashed lines; the remaining peaks are spinning side bands that originate from MAS. The cartoon on the left illustrates the method used to prepare the electrode film. Data were collected at a spinning speed of 35 kHz. Figure is reproduced with permission from Ref 1.

The two preparation steps are expected to cause degradation in different manners. High-energy ball milling generally reduces the particle sizes dramatically and creates new, highly reactive surfaces, which likely leads to the observed degradation of $LiFeBO_3$. During the electrode film preparation, absorbed moisture in the carbon, PVDF or NMP components can directly contribute to the oxidation of the $LiFeBO_3$ surface and the accompanying Li loss. Due to these facile degradation processes, the inherent electrochemical capacity of $LiFeBO_3$ will be very difficult to access in batteries prepared using this method. Thus, an optimized electrode fabrication process was used in which solvents or liquid components involved were dried by molecular sieves before use, and all the powders or solid components were dried at 100 ℃ in an oven. Moreover, the ball-milling step was eliminated. As can be seen in Figure 2.7, the resonance at 0 ppm is very weak in electrode film fabricated by this manner, which indicates that the degradation of $LiFeBO_3$ during electrode fabrication can be effectively controlled.

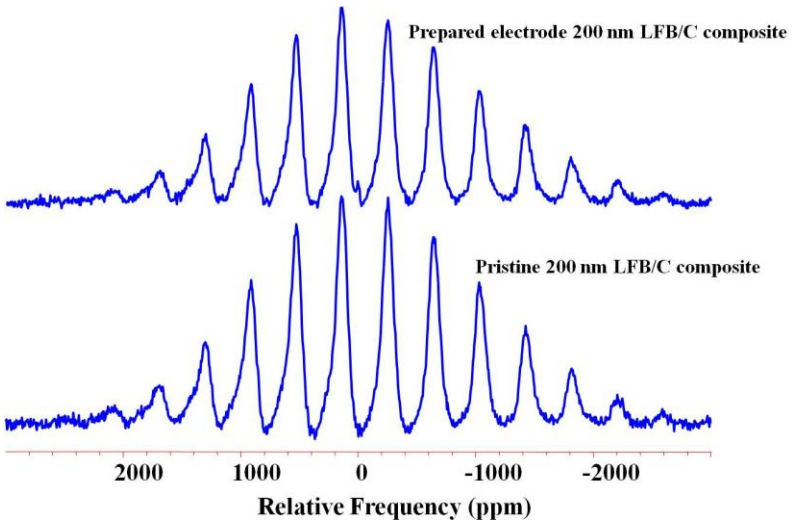

Figure 2.7. ^{7}Li MAS NMR spectra of the pristine 200 nm $LiFeBO_3$/C composite and the corresponding prepared electrode film. Data were collected at a spinning speed of 35 kHz. Figure is reproduced with permission from Ref 1.

2.3.3 Degradation mechanism of $LiFeBO_3$

The use of *in situ* XRD techniques at elevated temperature allowed the structural evolution of 200 nm $LiFeBO_3$/C during the degradation to be captured in a single experimental run. In a typical experiment, 200 nm $LiFeBO_3$/C was mounted on the heating stage of a diffractometer, and the diffraction patterns were collected while heating. As highlighted in the zoomed-in region of Figure 2.8, the diffraction patterns start with two symmetry-related reflections in the signature regions (*112* and *11-2* peaks viewed between $2\theta = 25.5°$ and $2\theta = 27.5°$), and one degraded phase peak grows to be dominant at the end of the reaction. Although there are clearly microscopic changes in the patterns, the large changes in the peak positions and intensity do not occur during degradation. This indicates that the long-range structure change occurring to $LiFeBO_3$ is likely due to subtle changes in occupancies, bonding, and/or coordination, but most likely does not involve radical changes in the iron borate structural framework, at least until 150 °C.

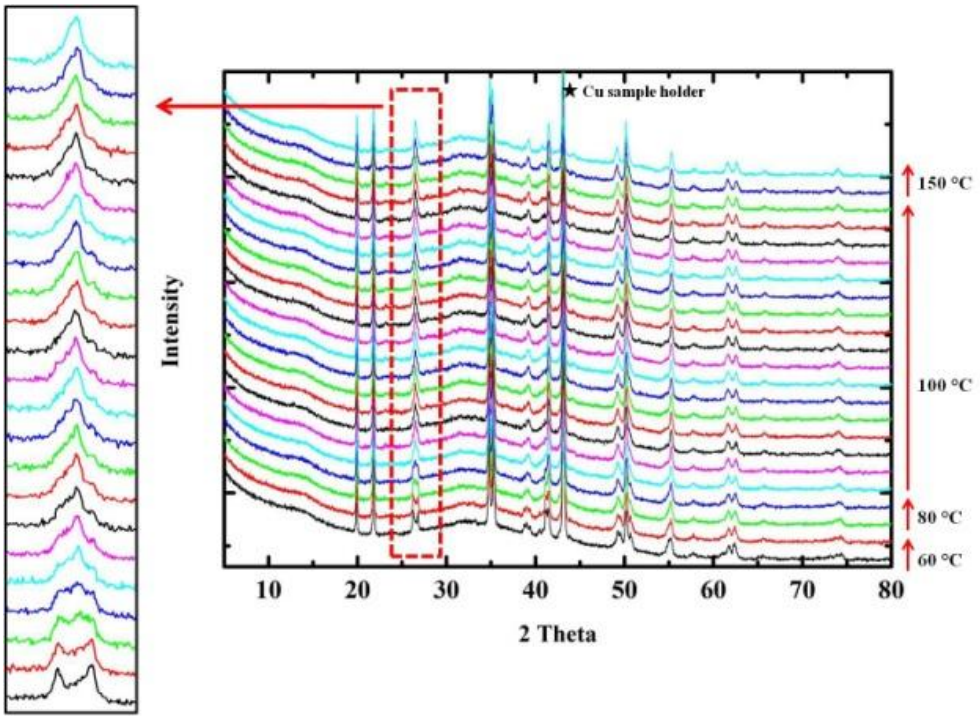

Figure 2.8. *In-situ* X-ray diffraction patterns of the $LiFeBO_3$/C composite with an average particle size of 200 nm during heating up to 150 ℃ in air over 30 hrs. The temperature was ramped at a rate of 10 ℃/min, and then stabilized for ~30 mins at target temperatures (60 ℃, 80 ℃, 100 ℃, and 150 ℃) before collecting scans. Each scan took approximately 80 minutes, and the temperature remained constant while scanning. Data was collected and analyzed in collaboration with Dr. Wenqian Xu from Stony Brook University. Figure is reproduced with permission from Ref 1.

Degraded 200 nm $LiFeBO_3$/C samples formed by heating at 100 ℃ in air for variable times were further characterized using *ex situ* ^{7}Li MAS NMR (Fig. 2.9). Although XRD results suggest only small structural differences between the pristine and degraded phases, the NMR results show very different responses from Li in the phases formed during degradation. After 12

hours at 100 ℃, two new resonances were observed together with the -233 ppm resonance of the Li in the pristine material. One new resonance with a shift of around -3 ppm is ascribed to Li contained within a diamagnetic phase, while the second resonance with a shift of around +218 ppm is ascribed to Li nearby paramagnetic iron centers. On the basis of prior NMR studies of lithium iron(II) and iron(III) oxides and phosphates, a shift to higher frequencies is generally associated with an increase of iron oxidation state[9]. For example, large positive ^{6,7}Li Fermi contact shifts are observed for a number of Fe(III) containing phosphates, such as $LiFeP_2O_7$, monoclinic $Li_3Fe_2(PO_4)_3$ and rhombohedral $Li_3Fe_2(PO_4)_3$. Thus, the 218 ppm peak was assigned to Li in an Fe(III)-rich environment.

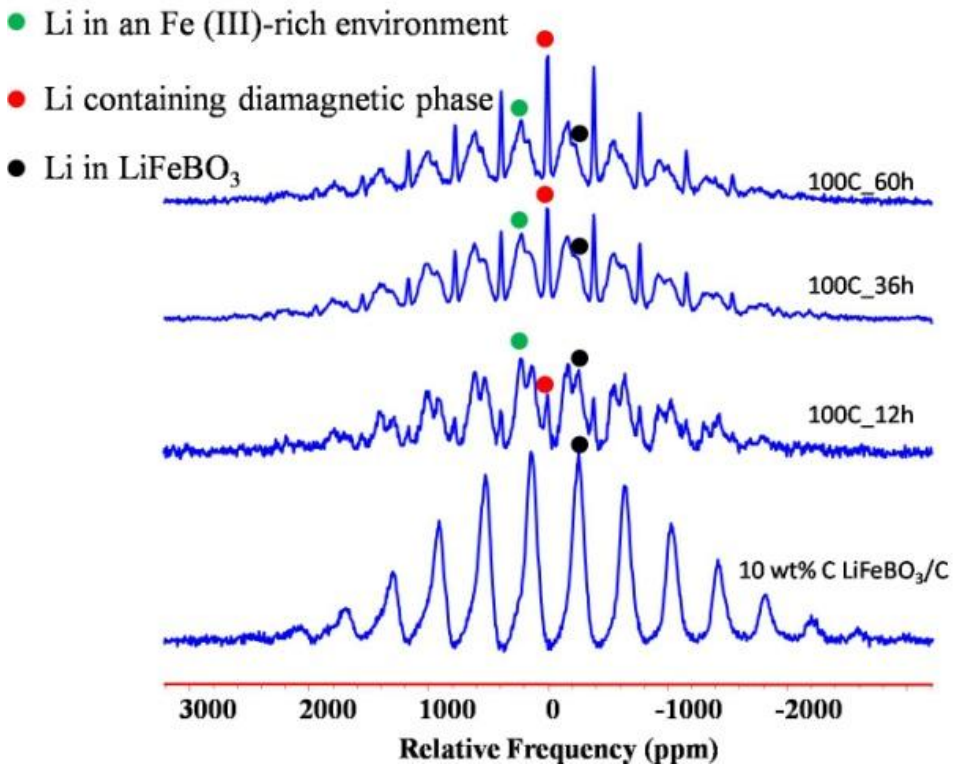

Figure 2.9. *Ex situ* ^{7}Li MAS NMR spectra of the 200 nm $LiFeBO_3$/C composite before and after heating in air. Data were collected at a spinning speed of 30 kHz. Figure is reproduced with permission from Ref 1.

With increasing heating time in air, the -3 ppm and +218 ppm resonances continuously grow in intensity while the -233 ppm resonance decreases (Fig. 2.9). After 60 hours of exposure, the resonance due to pristine $LiFeBO_3$ has almost disappeared. No obvious changes in chemical/Fermi contact shifts occurred during the entire time course studies, suggesting that the principal Li-containing phases (environments) signified by these three resonances are not substantially modified during the degradation process, although their relative intensity clearly varies dramatically. In particular, it suggests that the Fe valence state is essentially constant in both the original $LiFeBO_3$ material and in the higher valence degradation product, and that

neither phase has a variable Li content. This implies that the Li loss from $LiFeBO_3$ that accompanies degradation results in an immediate structural transformation to a new phase that is Li-poor and contains Fe in a higher oxidation state. The fact that the degraded phase still exhibits a ^{7}Li NMR signal suggests that Fe in the phase is not fully oxidized to Fe(III).

Investigations into the degradation-induced changes in Fe valence and local structure by X-ray absorption spectroscopy were carried out through *ex situ* experiments using 200 nm $LiFeBO_3$/C samples treated at 100 ℃ in air. Normalized Fe *K*-edge XANES spectra of the product after different degradation times are compared to the reference compounds of $Fe(II)Cl_2$ and $Fe(III)_2O_3$ in Figure 2.10a. Spectra always contained both a pre-edge feature (labeled "A") and a main edge feature (labeled "B"). The expected Fe(II) valence of the initial pristine $LiFeBO_3$/C composite is seen in its XANES spectrum, which has an edge position that is close to the $Fe(II)Cl_2$ reference compound. While heat treatments definitely result in the oxidation of iron, the XANES spectrum of the final 120 hr product falls midway between that of the Fe(II) and Fe(III) reference compounds suggesting that the fully converted degradation product does not have fully oxidized iron, consistent with the ^{7}Li NMR results, which also suggested that a mixed Fe(II)/Fe(III) compound was formed.

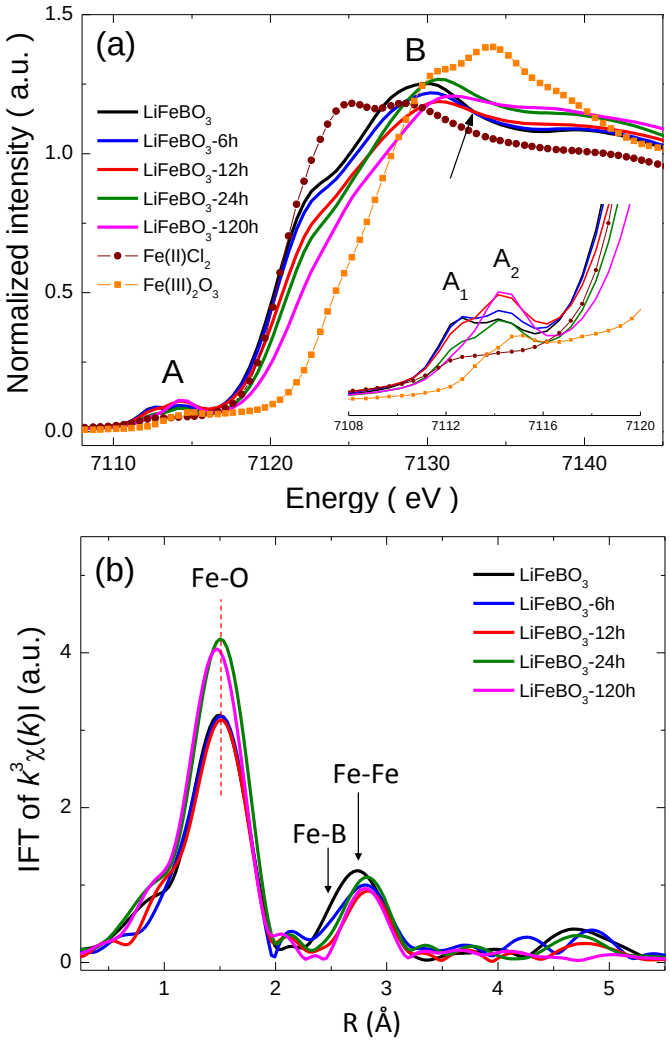

Figure 2.10. (a) Normalized Fe K-edge XANES spectra of the 200 nm $LiFeBO_3$/C composite with different degradation times as compared to the reference iron compounds $(Fe(II)Cl_2$ and $Fe(III)_2O_3)$. The inset shows detailed features in the pre-edge region A from 7108 to 7120 eV. The arrow marks an isosbestic point, a feature that is only present for the first 12 hrs. (b) Fourier transforms (FTs) magnitudes of the of EXAFS spectra, suggesting that a second Fe-containing degradation phase with octahedral iron is present after 24 hrs. The phase shift in the FTs was not corrected. Data was collected and analyzed in collaboration with Dr. Kyung-wan Nam from Brookhaven National Laboratory. Figure is reproduced with permission from Ref 1.

A closer look at the changes in the XANES features suggests that the degradation process of 200 nm $LiFeBO_3$/C involves more than two Fe-containing species. The XANES spectra changes can be divided into two stages during the degradation: in the first 12 h of degradation, an increase in the pre-edge peak A intensity was observed while the main peak B corresponding to *1s→4p* electronic transition decreased. Notably, there appear to be isosbestic points at ~7113 and ~7134 eV (latter indicated by an arrow in Fig. 2.10a), which suggests that the degradation process involves only two Fe-containing phases during this period, pristine $LiFeBO_3$ and a degraded phase having a higher oxidation state (likely the Fe(III)-rich phase observed in the NMR experiments). Beyond 12 h, the peak intensities vary in the opposite manner (A decreases, B increases) and no isosbestic point exists, indicating that at least one more iron-containing phase is present. This phase could either represent a new phase such as an iron oxide or borate, or change in oxidation state in an existing phase that substantially modifies its XAS response.

Insights into the Fe local structural changes that accompany the degradation process can be obtained from the pre-edge A feature. Pre-edge absorption is attributed to the electric dipole forbidden transition from a 1s electron to an unoccupied *3d* orbital (which can be partially allowed in the presence of electric quadrupole coupling due to *3d-4p* orbital mixing arising from a non-centrosymmetric Fe-O coordination environment). $LiFeBO_3$, with its trigonal bipyramial FeO_5 coordination, has a pre-edge peak intensity that is substantially higher than those of the reference compounds $Fe(II)Cl_2$ (octahedral FeO_6) and Fe_2O_3 (mixed octahedral FeO_6 and tetrahedral FeO_4) (Fig. 2.11). A close look at the pre-edge feature of pristine and degraded phases (inset of Fig. 2.10a) shows that it is at least a doublet (with the two dominant peaks labeled A_1 and A_2 in order of increasing energy). This doublet likely results from the presence of multiple phases that have different oxidation states (*e.g.*, Fe(II) and Fe(III)). The A_1 feature is

present in highly pure ceramic $LiFeBO_3$ while the A_2 feature appears to be absent (Fig. 2.11), suggesting that the A_2 feature is indicative of the main degradation phase. Over the first 12h, the observed enhancement in the A_2 intensity relative to the A_1 peak intensity indicates the growth of the main degradation phase with the sacrifice of the $LiFeBO_3$ phase. Beyond 12h, the net intensity of the pre-edge features (primarily A_1 and A_2) decreases relative to less degraded samples. This decreased pre-edge intensity can be correlated to symmetry changes of the Fe-O coordination environment, which could potentially assigned to the formation of an iron compound with an octahedral FeO_6 environment by analogy to the behavior of reference compounds.

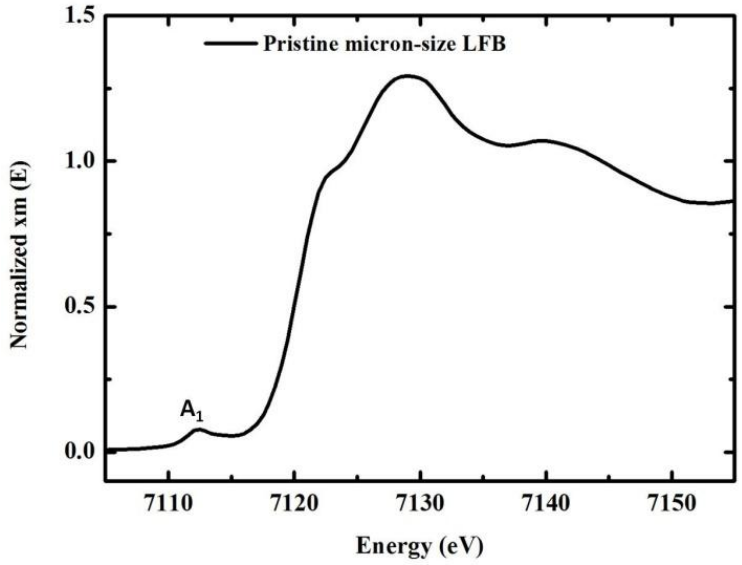

Figure 2.11. XANES of the highly pure ceramic (carbon-free) $LiFeBO_3$. The presence of **A_1** feature is due to the noncentrosymmetric FeO_5 coordination environment in $LiFeBO_3$. Data was collected and analyzed in collaboration with Dr. Kyung-wan Nam from Brookhaven National Laboratory. Figure is reproduced with permission from Ref 1.

The presence of octahedral Fe-O or Fe with a larger coordination number (CN) at the end of the degradation process is also suggested by Fourier-transform (FT) magnitudes of EXAFS spectra for these samples (Fig. 2.10b). For pristine $LiFeBO_3$, the first strong peak around 1.5 Å corresponds to the first Fe-O coordination shell while the second weaker peak around 2.7 Å corresponds to the five Fe-B interatomic distances and the two Fe-Fe distances found in the previously reported $LiFeBO_3$ crystal structure. These assignments agree with the literature values of the bond lengths, noting that the FT was not phase-corrected so that the actual bond lengths are typically underestimated by 0.2~0.4 Å. The intensity of the peak at 1.5 Å (Fe-O) substantially increases after 12h, suggesting the creation of a higher coordinated iron in the degradation process. Considering that no third Fe-containing ^{7}Li response was observed in the *ex situ* NMR measurements besides the +218 and -233 ppm resonances, this higher coordinated (presumably 6-coordinate) Fe compound should be free of Li, and some candidate phases are Fe_3O_4, Fe_2O_3, or $FeBO_3$. The increase in the Fe-Fe interatomic distance on degradation is ascribed to the increased repulsion between the cations as their oxidation state increases.

TEM-EELS studies allow the distribution of phases within a single particle to be determined in a manner that is not possible using the bulk structural probes previously discussed, providing deeper insights into the mechanism of the degradation process. TEM experiments were performed on the same class of 200 nm $LiFeBO_3$/C particles, and the data shown in Figure 2.12 is for a particle after heating in air for 70 hours, corresponding to the second stage of degradation according to the XAS results. Spectra acquired along a line from the exterior to the center of an approximately 150 nm diameter single particle were used to probe variations in the overall chemical composition and in the specific Fe valence state. The integrated intensity of the O *K*-edge and Fe L_3 peak (Fig. 2.12b) peaks show a rapid increase in intensity that is attributed to the

spherical shape of the particle and the increased path length that the beam travels through the sample. Phase changes were followed through the ratio of the edge peak intensities I_{Fe}/I_O. In the outer 30 nm of the particle this ratio is nearly constant at about 0.9 ± 0.1. Further in the particle (30-42 nm), the ratio decreases slightly to 0.8 ± 0.1, suggesting the presence of a phase that is different from the phase in the near-surface region.

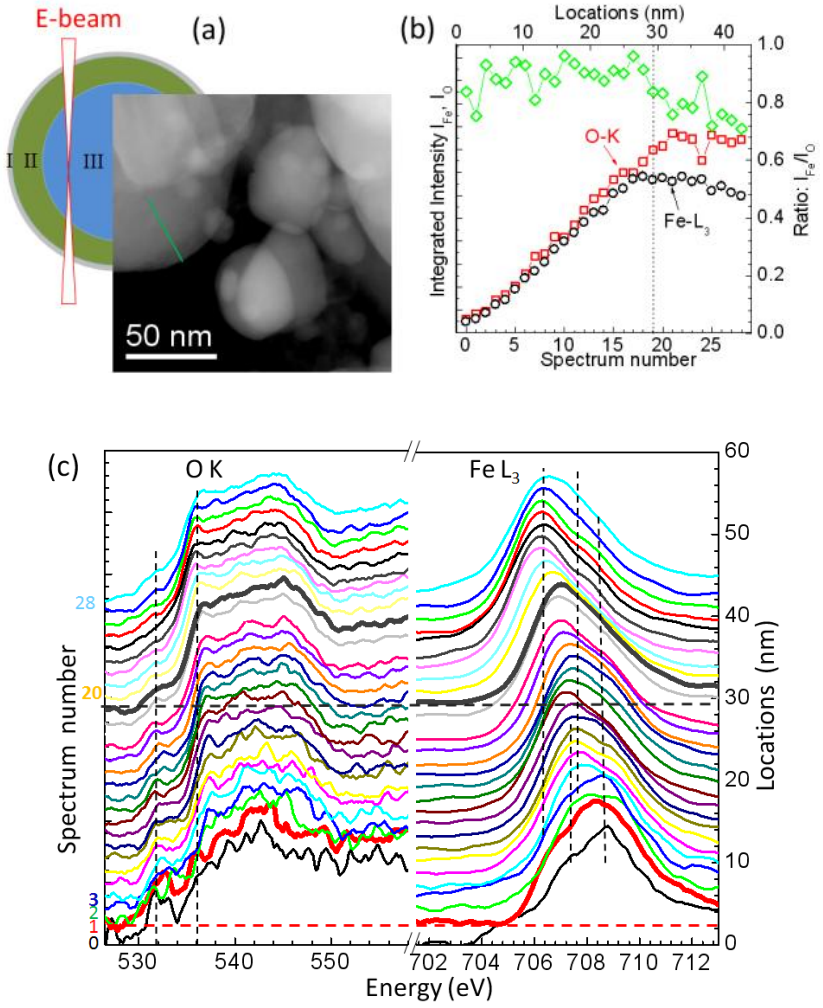

Figure 2.12. Degradation of individual particles by STEM-EELS: (a) ADF-STEM survey image. Scanning was performed along the green line marked in this figure, from the edge towards the center of a particle; (b) integrated intensity for the Fe L_3 and O K edges; the ratio of the two

intensities is shown as green diamonds; (c) EELS spectra for O *K* and Fe L_3 edges recorded at different sites along the green line in (a). Data was collected and analyzed in collaboration with Dr. Feng Wang from Brookhaven National Laboratory. Figure is reproduced with permission from Ref 1.

The fine structure of the O *K* edge and Fe L_3 edge suggest the presence of three regions (I - III). In a manner similar to the XAS Fe *K*-edge, the Fe L_3 peak (arising from *2p-3d* transition) is sensitive to the coordination environment and oxidation state of Fe. Region I, (the outer 2-3 nm of the nanocrystal) gives rise to the splitting of the Fe L_3 peak, with a main peak at 708.7 eV, and a shoulder at 707.1 eV, features that are characteristic of Fe at a higher valence state, *i.e.* Fe^{3+}. It is challenging to resolve the phase in this 2-3 nm thin surface layer by routine crystallography tools. However, the high energy of the Fe L_3 edge and the noticeable pre-peak in the O *K* edge data (Fig. 2.12c) suggest the likely formation of Fe_2O_3 or a structurally similar phase, although the presence of an Fe-rich borate cannot be excluded. The small fraction of Region I makes this phase invisible to the bulk sensitive techniques that have been applied to study the degradation process (XRD, NMR and XAS). It should be also stated that we did not observe this thin layer in the pristine 200 nm $LiFeBO_3$/C sample, suggesting that this layer is a degradation product.

The phase present in Region II (3-30 nm from surface) is almost certainly the degradation product with a structure closely related to that of $LiFeBO_3$ that was observed in the XRD studies, and which gives rise to a ^{7}Li NMR resonance at +218 ppm. In this region, the characteristic Fe EELS features are a main peak located at 707.2 eV and a shoulder at 708.7 eV. Some differences

between spectra near the I / II interface (spectrum 2, green; spectrum 3, blue) come from the differential contribution of the surface Region I to the spectrum of a region of the particle dominated by Region II, which may be easily understood by considering the illustration of the electron beam configuration (inset of Fig. 2.12a). As indicated by the EELS spectra, the Fe oxidation state in this region is between Fe^{3+} and Fe^{2+}, which is almost certainly accompanied by a loss of Li based on our NMR data. Region III extends inwards from a depth of 30 nm to the center of the particle, and corresponds to the pristine $LiFeBO_3$ that has been preserved against degradation. The strong EELS peak shifts to a lower energy of 706.4 eV, indicating a lower valence state of Fe, most likely Fe^{2+}; however, this peak is broadened due to the contributions from Regions I and II that the electron beam must transverse before entering Region III. The intact $LiFeBO_3$ present in the core of this 150 nm particle suggests that degradation is a self-limiting process, a conclusion that is supported by the negligible changes in the bulk x-ray patterns of micron-size $LiFeBO_3$ after heating in air at 100 ℃ for 3 days (Fig. 2.13). The self-limiting degradation process can potentially correlate to the diffusion of Li, which is an essential step during the degradation process. Where the starting particles are small (< ~60 nm), complete degradation of the particles was observed where $LiFeBO_3$ core is absent (Fig. 2.14). The formation of an iron rich coating on the surface may also slow down the degradation process.

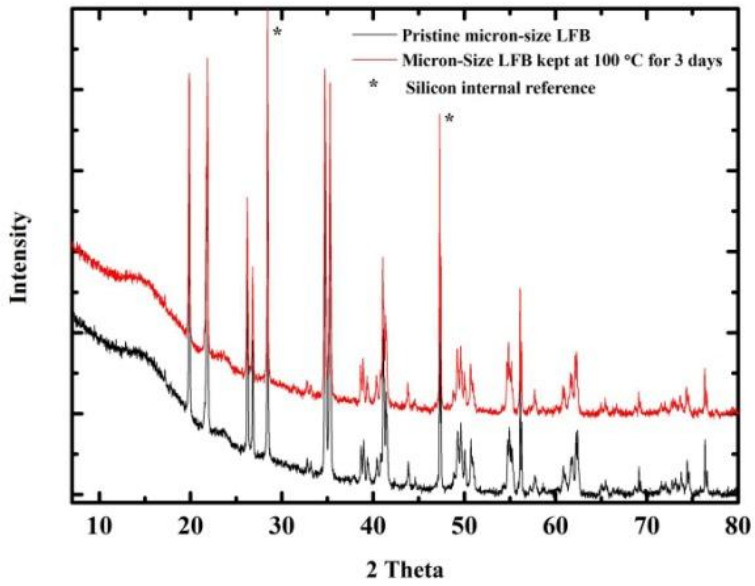

Figure 2.13. XRD patterns of pristine micron-size $LiFeBO_3$ and the sample after 3-day heat treatment at 100 °C in air. Figure is reproduced with permission from ref 1.

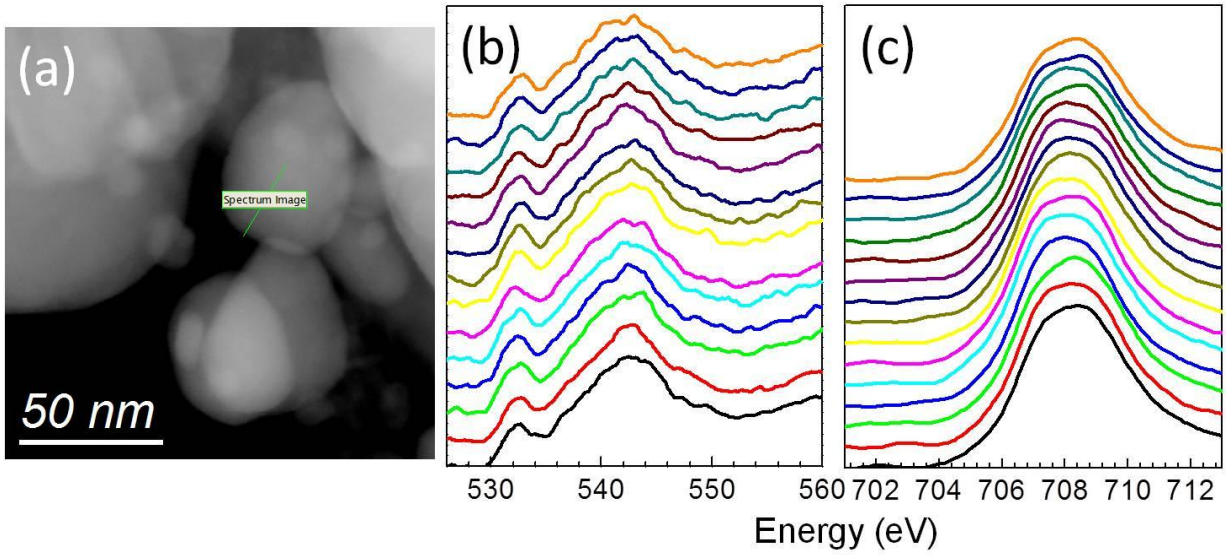

Figure 2.14. STEM-EELS studies of 200 nm $LiFeBO_3$/C after 70 hours heat treatment in air: (a) DF-STEM image shows the scanning along the green line, from the edge towards the center of a

particle (~50 nm); (b) O *K* edge and (c) Fe L_3 edge recorded at different sites along the green line in (a). The big prepeak in the O *K*-edge and high energy position of Fe L_3 (~ 708 eV) peak indicates a higher oxidation state of Fe, as a result of the degradation. Figure is reproduced with permission from Ref 1.

The O *K* edge data support the assignment of these regions, though the interpretation of this data will not be discussed in depth due to its similarity with the Fe L_3 edge results. Notably, the fine structure in Region III closely resembles data collected from a pristine $LiFeBO_3$ sample that has not been exposed to degradation-causing conditions. The small changes in the O *K* edge pre-peak and main peak (whose positions are marked by the black dashed lines in Fig. 2.12) also suggest that Region II represents the degraded phase.

A schematic representation of three shells of phases created by the degradation of predominantly 200 nm $LiFeBO_3$ primary particles is given in Figure 2.15. The innermost core (III) is intact $LiFeBO_3$, which is protected by the self-limiting nature of the degradation reaction. Surrounding this core is a ~30 nm shell of a new degraded phase (II) which has a composition that is probably near $Li_{0.5}FeBO_3$ and which has a structure related to that of $LiFeBO_3$. The degradation of $LiFeBO_3$ appears to occur in a homogenous and epitaxial fashion that does not lead to particle cracking. Finally, there is a 2-3 nm thick surface layer (I) of a more highly oxidized iron oxide, hydroxide or iron-rich borate. When the degradation occurs, Li must react with appropriate counterions (such as hydroxide or oxide ions extracted from moisture or carbonate ions extracted from atmospheric CO_2) to form the diamagnetic phases that were seen by NMR. These presumably surround the $LiFeBO_3$ particles, not as a surface film, but possibly

as the smaller particles shown in Figure 2.15.

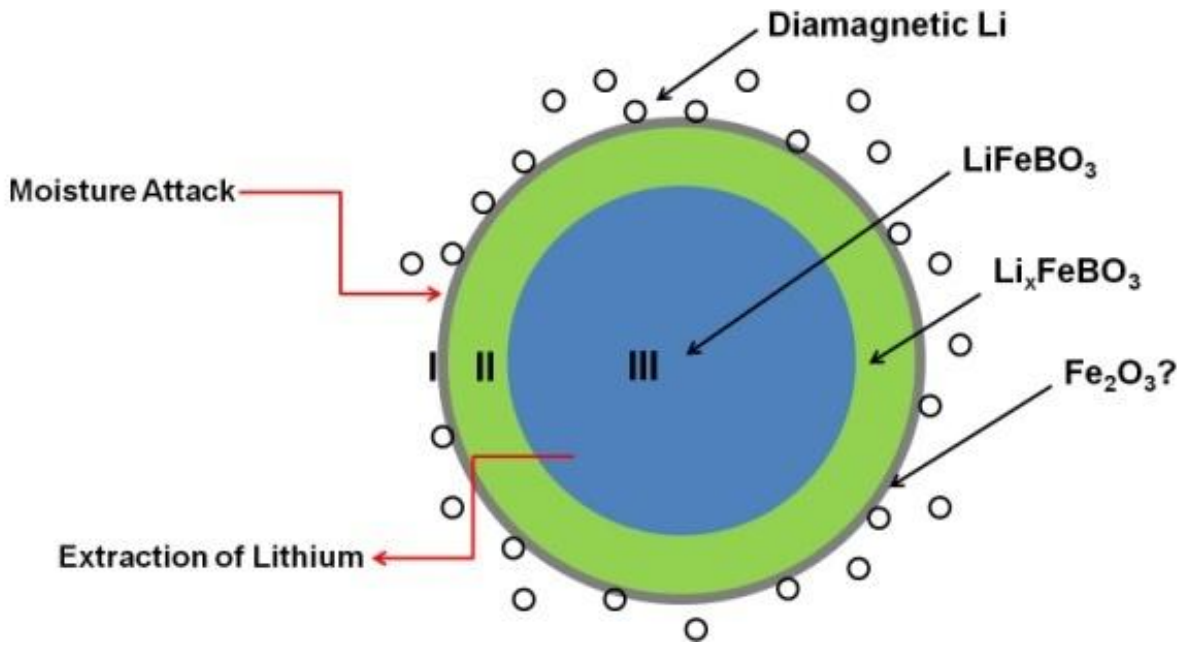

Figure 2.15. Schematic representation of the degradation mechanism of the nano-size $LiFeBO_3$/C composite. Figure is reproduced with permission from Ref 1.

2.3.4 Electrochemistry

The insights obtained from the studies into the $LiFeBO_3$ degradation process and mechanism were used to design an optimized procedure for preparing $LiFeBO_3$ electrodes. In all cases, electrode preparation was carried out under conditions shown to minimize $LiFeBO_3$ degradation through monitoring of the diamagnetic Li peak in the ^{7}Li NMR experiments. The total air exposure time was limited to < 10 min, and moisture from carbon, PVDF and NMP were removed before use. The best performance was obtained from $LiFeBO_3$ synthesized with ~20 wt% carbon (~100 nm particle size) rather than the ~200 nm particles that resulted from the use

of 10 wt% carbon or the ceramic micron-size $LiFeBO_3$ (Fig. 2.16). This suggests that the conductivity limitations (ionic and/or electronic) severely hinder the performance of this material. Electrochemical characterization therefore focused on electrodes prepared from this ~100 nm $LiFeBO_3$/C composite (20 wt% carbon).

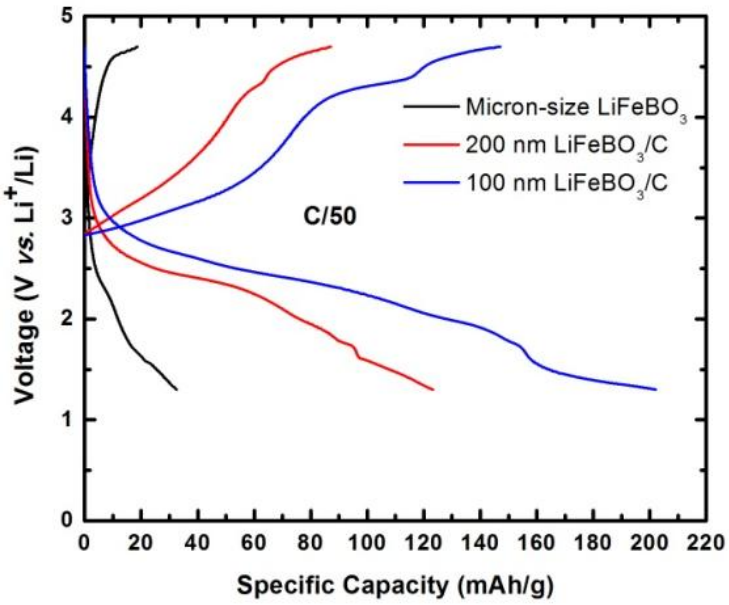

Figure 2.16. Comparison of the 1st cycle performance of micron-size $LiFeBO_3$, 200 nm $LiFeBO_3$/C and 100 nm $LiFeBO_3$/C. Figure is reproduced with permission from Ref 1.

The electrochemical cycling performance of ~100 nm $LiFeBO_3$/C (20 wt% carbon) between 4.7 V and 1.3 V (*vs.* Li^+/Li) is shown in Figure 2.17. The first charge gives a capacity of ~140 mAh/g at C/50. A substantially larger capacity was observed for the second charge (~190 mAh/g), in a manner similar to that observed by the Yamada group. The extra gain in capacity in

the second charge originates from the capacity delivered below 2.8 V, which is the initial open circuit voltage (OCV) of the battery. This suggests that pre-oxidation of $LiFeBO_3$ has occurred prior to the first charge resulting in leveling of the OCV to the potential that moisture provides, even with precautions taken to prevent this. Access to the redox process below 2.8 V, which do not survive ambient conditions become possible after the electrode is discharged with the hermetically sealed battery cell, and this cycling remains reversible in subsequent cycles. It appears possible that Li loss from the degradation process of $LiFeBO_3$ can be readily reversed using a discharge cycle.

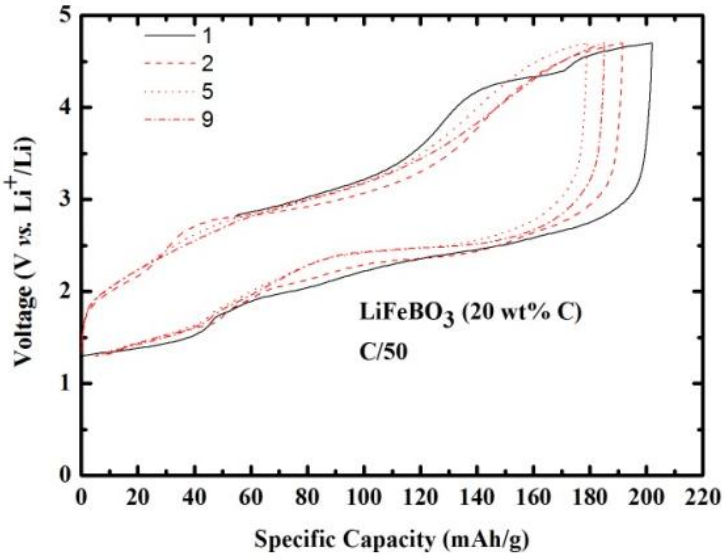

Figure 2.17. Charge and discharge curves of 100 nm $LiFeBO_3$/C composite (20 wt% carbon) at C/50. Figure is reproduced with permission from Ref 1.

It can be seen that $LiFeBO_3$ continues to reversibly store charge even when cycled to the low potential of 1.3 V. This is far below the ~3.0 V potential of the nominal average operating voltage of Fe(III)/Fe(II) redox couple in Li_xFeBO_3, and may represent the observation of Fe conversion chemistry (reduction to metallic Fe) rather than intercalation chemistry. It is also

possible that this process involves the lithiation of disordered or amorphous phase formed either *via* the initial degradation or on charge. Surprisingly, this electrochemistry process is reversible, making a future investigation of this process worthwhile. Approximately ~160 mAh/g (based on the second charge) can be assigned to reversible intercalation processes of this composite electrode, this process having a high degree of polarization (~0.5 to 1 V) even for these small nano-particles. This high polarization is almost certainly related to the low electronic (and possibly ionic) conductivity of the composite electrode. However, it is not known whether this reflects the intrinsic Li conduction properties of $LiFeBO_3$ or instead originates from low electronic and/or Li ion conductivity of the difficult-to-eliminate degraded phase that may form a shell around each $LiFeBO_3$ core. A third possibility is that the diamagnetic Li-containing phase generated during the degradation can sharply decrease the electronic conductivity of the system.

Further understanding of the electrochemical processes in $LiFeBO_3$ can be obtained using galvanostatic intermittent titration technique (GITT) studies, which can provide information about the equilibrium thermodynamic voltages that are obscured when polarization (and therefore a kinetic limitation) exists. This is one of the most straightforward ways to identify whether (de)lithiation occurs through a solid solution or a two-phase reaction mechanism. The (de)lithiation of $LiFeBO_3$ were previously reported to occur through a solid solution pathway based on the evolution of lattice parameters in diffraction studies, implying the presence of a continuum of phases with formula Li_xFeBO_3[2d]. However, our GITT data (Fig. 2.18) do not support that conclusion and suggest that at least some of the delithiation occurs via a two-phase reaction. Starting at the OCV of 2.8 V for the as-prepared $LiFeBO_3$ electrode materials, charging gives a plateau at the beginning which is followed by a sloping region. This indicates that delithiation of $LiFeBO_3$ first proceeds through a two-phase pathway (where the two phases

present are the monoclinic $LiFeBO_3$, *m*-$LiFeBO_3$ and a second uncharacterized phase which appears to be partially delithiated $LiFeBO_3$, referred to as *pdl*-$LiFeBO_3$) and possibly afterwards a solid solution pathway (where monoclinic $LiFeBO_3$ is absent and the *pdl*-$LiFeBO_3$ loses its Li in a continuous manner form a presumed "$FeBO_3$" end product). However, it should be noticed that the large polarization observed when charging up to 4 V posed significant difficulty in fully relaxing the electrode to the equilibrium thermodynamic potentials of the system, which complicates our analysis of the delithiation behavior of $LiFeBO_3$ at high voltages. It is therefore possible that the two-phase region can extend to near the end of charging. Upon discharging, the lithiation reaction proceeds in a reversed manner as when charging. The lithiation begins with a sloping region, which is then followed by a plateau region at about 2.8 V, which should correspond to continuous Li insertion into the "$FeBO_3$" end member producing the *pdl*-$LiFeBO_3$ phase, and the two-phase reaction between *pdl*-$LiFeBO_3$ and *m*-$LiFeBO_3$, respectively. Notably, there appears to be a different electrochemical process with an equilibrium thermodynamic potential of below 1.8 V, which may be related to the Fe conversion chemistry or a reaction with a degraded or an amorphous phase. A detailed discussion regarding this low voltage process can be found in the next chapter.

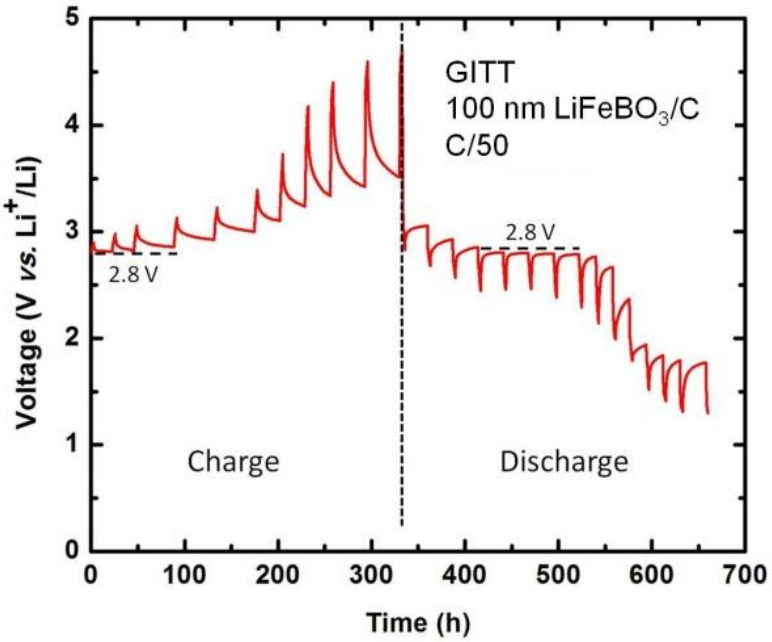

Figure 2.18. Galvanostatic intermittent titration curve of $LiFeBO_3$ upon first charging and discharging. The battery is charged at a rate of C/50, and allowed to relax after each 3-hour current pulse for time intervals of 15-50 hours. Figure is reproduced with permission from Ref 1.

2.4 Conclusions

Highly pure $LiFeBO_3$ samples with different particle sizes were synthesized *via* solid-state synthesis under an actively reducing atmosphere (5% H_2/ 95% N_2). The use of citric acid as a carbon source played an important role in limiting the particle size of the reaction products and enhancing the reversible capacity. Strict air and moisture avoidance was also critical to obtain a large reversible capacity. Accurate assessment of the capacity of $LiFeBO_3$ was complicated by the observation of three different electrochemical regimes. The lowest potentials of (1.3 - 1.5 V) appeared to access reversible conversion chemistry reactions or reactions with a second possibly disordered borate phase that occurs at a thermodynamic potential of about 1.8 V. Intermediate

(1.5 V- 3.4 V) were required to remove the first 0.5 Li from $LiFeBO_3$ in a two-phase reaction occurring at a thermodynamic potential of 2.8 V, but with a moderate polarization (~0.2 – 0.5 V). The last 0.5 Li were removed from intermediate $Li_{0.5}FeBO_3$ phase through what appears to be a solid solution mechanism at a thermodynamic potential of above 2.8 V, with a very large polarization (~0.5 to more than 1.5 V) indicative of poor Li/electronic transport within this phase.

A degradation model of $LiFeBO_3$ can be constructed to explain the experimentally observed structural and chemical changes that result from moisture exposure and heating in air. The degradation of nanoscale $LiFeBO_3$ is initiated on the surface of the particles and moves inward along a spherical front. Moisture/air attack drives the surface oxidation of Fe(II) in a process which maintains charge balance through Li loss, but which cannot occur in the absence of suitable counterions (such as OH^-, O^{2-} or CO_3^-). The Li must be transported to the surface in a diffusional process for degradation to occur. Present and prior electrochemical tests on $LiFeBO_3$ suggest that Li ions can diffuse ~100 nm within $LiFeBO_3$ on the relevant timescale (~1 day) at room temperature; substantially larger mobilities are expected at 100 ℃.

In situ XRD experiments demonstrate that the degradation reaction causes an immediate structural conversion to a new phase, which appears to be similar to the two-phase reaction that occurs on delithiation. Based on the limited depth of degradation, it appears that this new degradation product has much lower Li mobility and electronic transport than $LiFeBO_3$. This is also consistent with the present and previously observed resistance of the degradation product to electrochemical delithiation that can severely limit the experimentally accessible charge capacity of $LiFeBO_3$. It is not as-yet known if the degraded phase is identical to the intermediate phase that occurs during $LiFeBO_3$ delithiation (detailed discussion in the next chapter). Although the

large theoretical capacity of $LiFeBO_3$ (220 mAh/g) makes this material desirable for electrochemical storage applications, the observed thermodynamic voltages of Li (de)intercalation (2.8-3.0 V) limit the specific energy density and stability of this compound.

In summary, fundamental insights into the factors that limit the electrochemical performance of $LiFeBO_3$ were obtained via the use of a wide range of complementary structural probes. With the in-depth understanding of the degradation and capacity loss of $LiFeBO_3$ upon air exposure, it is anticipated that improved electrochemical performance can be achieved in the near future.

2.5 References

1. Bo, S.-H.; Wang, F.; Janssen, Y.; Zeng, D.; Nam, K.-W.; Xu, W.; Du, L.-S.; Graetz, J.; Yang, X.-Q.; Zhu, Y.; Parise, J. B.; Grey, C. P.; Khalifah, P. G., Degradation and (de)lithiation processes in the high capacity battery material $LiFeBO_3$. *J Mater Chem* **2012,** *22* (18), 8799-8809.

2. (a) Dong, Y. Z.; Zhao, Y. M.; Shi, Z. D.; An, X. N.; Fu, P.; Chen, L., The structure and electrochemical performance of $LiFeBO_{(3)}$ as a novel Li-battery cathode material. *Electrochimica Acta* **2008,** *53* (5), 2339-2345; (b) Legagneur, V.; An, Y.; Mosbah, A.; Portal, R.; La Salle, A. L.; Verbaere, A.; Guyomard, D.; Piffard, Y., $LiMBO_3$ (M = Mn, Fe, Co): synthesis, crystal structure and lithium deinsertion/insertion properties. *Solid State Ionics* **2001,** *139* (1-2), 37-46; (c) Seo, D. H.; Park, Y. U.; Kim, S. W.; Park, I.; Shakoor, R. A.; Kang, K., First-principles study on lithium metal borate cathodes for lithium rechargeable batteries. *Physical Review B* **2011,** *83* (20); (d) Yamada, A.; Iwane, N.; Harada, Y.; Nishimura, S.; Koyama, Y.;

Tanaka, I., Lithium Iron Borates as High-Capacity Battery Electrodes. *Advanced Materials* **2010,** *22* (32), 3583-3587.

3. Janssen, Y.; Middlemiss, D. S.; Bo, S.-H.; Grey, C. P.; Khalifah, P. G., Structural Modulation in the High Capacity Battery Cathode Material $LiFeBO_3$. *J Am Chem Soc* **2012,** *134* (30), 12516-12527.

4. Hamelet, S.; Gibot, P.; Casas-Cabanas, M.; Bonnin, D.; Grey, C. P.; Cabana, J.; Leriche, J. B.; Rodriguez-Carvajal, J.; Courty, M.; Levasseur, S.; Carlach, P.; van Thournout, M.; Tarascon, J. M.; Masquelier, C., The effects of moderate thermal treatments under air on $LiFePO_{(4)}$-based nano powders. *Journal of Materials Chemistry* **2009,** *19* (23), 3979-3991.

5. Grey, C. P.; Dupre, N., NMR studies of cathode materials for lithium-ion rechargeable batteries. *Chem Rev* **2004,** *104* (10), 4493-4512.

6. Wang, F.; Graetz, J.; Sergio Moreno, M.; Ma, C.; Wu, L.; Volkov, V.; Zhu, Y., Chemical Distribution and Bonding of Lithium in Intercalated Graphite: Identification with Optimized Electron Energy Loss Spectroscopy. *Acs Nano* **2011,** *5* (2), 1190-1197.

7. Szczygiel, R.; Grybos, P.; Maj, P.; Tsukiyama, A.; Matsushita, K.; Taguchi, T., Low-noise multichannel ASIC for high count rate X-ray diffractometry applications. *Nuclear Instruments & Methods in Physics Research Section a-Accelerators Spectrometers Detectors and Associated Equipment* **2009,** *607* (1), 229-232.

8. Ravel, B.; Newville, M., ATHENA, ARTEMIS, HEPHAESTUS: data analysis for X-ray absorption spectroscopy using IFEFFIT. *Journal of Synchrotron Radiation* **2005,** *12*, 537-541.

9. (a) Cabana, J.; Shirakawa, J.; Chen, G. Y.; Richardson, T. J.; Grey, C. P., MAS NMR Study of the Metastable Solid Solutions Found in the $LiFePO_{(4)}/FePO_{(4)}$ System. *Chem. Mat.* **2010,** *22* (3), 1249-1262; (b) Kim, J.; Middlemiss, D. S.; Chernova, N. A.; Zhu, B. Y. X.; Masquelier, C.; Grey, C. P., Linking Local Environments and Hyperfine Shifts: A Combined Experimental and Theoretical (31)P and (7)Li Solid-State NMR Study of Paramagnetic Fe(III) Phosphates. *J. Am. Chem. Soc.* **2010,** *132* (47), 16825-16840.

Chapter 3

Structures of degraded and delithaited $LiFeBO_3$, and their distinct structural changes upon electrochemical cycling [1]

3.1 Introduction

Two competing oxidative processes occurring in $LiFeBO_3$ *(i.e.*, the degradation and delithiation processes) were systematically investigated in the previous chapter, allowing the signatures of these two reactions to be identified through diffraction, NMR and XAS techniques. These signatures were used in this chapter to carry out a detailed mechanistic study on these two redox processes in $LiFeBO_3$. Detailed mechanistic knowledge is needed if the rate and voltage limitations of this compound [2,3] and its substituted variants [4,5] are to be understood and overcome.

Good room-temperature cycling behavior for $LiFeBO_3$ was only achieved after the existence of a degradation process was identified and steps were taken to minimize air exposure of $LiFeBO_3$ [2], leading to greatly improved electrochemical performance relative to prior studies [6]. Studies in the previous chapter determined that degradation results in the formation of a distinct phase with an as-yet unknown crystal structure that is expected to be closely related to that of the pristine $LiFeBO_3$ phase [7], and which still contains Li based on ^{7}Li solid state NMR data. In both cases, it was found that degradation occurs very quickly when nano-$LiFeBO_3$ is exposed to air, and that this process occurs faster under modest heating (100 – 200 ℃).

On delithiation, it has been clearly established that there is a ~2% reduction in the unit cell volume of $LiFeBO_3$. Published diffraction data has thus far lacked the resolution and intensity needed to effectively distinguish between the delithiated and degraded phases, which are similar in cell dimensions and volume. Single crystal diffraction experiments have recently demonstrated the existence of supercell in pristine $LiFeBO_3$ leading to a doubled *a*-axis and a four-dimensional space group of *C2/c*(α0γ)00 with α = ½ and β = 0 [8] relative to the originally reported crystal structure[6a]. However, the subcell space group (*C2/c*) and lattice (a = 10.336 Å; b = 8.869 Å; c = 10.166 Å; β = 91.514 °) are generally the most appropriate to use when modeling powder diffraction data since the strongest supercell reflection is about 3000 times weaker than the strongest subcell reflection, as judged from the X-ray diffraction structure factors. Unfortunately, this very small volume change makes it difficult to infer mechanistic insights (*i.e.*, solid-solution *vs.* two-phase) from the diffraction data published to date, which has been obtained on laboratory X-ray diffractometers.

The delithiation of the $LiFeBO_3$ was first reported to occur through a solid-solution mechanism with a continuum of phases $Li_{1-x}FeBO_3$ [2]. The solid solution mechanism was also suggested by density functional theory (DFT) calculations, based on the evaluation of the relative stabilities of $Li_{1-x}FeBO_3$ phases [2]. In a subsequent DFT study, the volume change between $LiFeBO_3$ and "$FeBO_3$" was predicted to be 1.4%, in reasonable agreement with experimental results [9]. It should be noted though that both DFT calculations were carried out using the originally published structure of $LiFeBO_3$ in the space group of *C2/c* (#15) rather than the commensurately modulated structure. The modulation in $LiFeBO_3$ results in a long-range ordering of the one-dimensional (1D) LiO_4 tetrahedral chains that cannot be described in the originally proposed unmodulated *C2/c* structure. This modulation modifies the configuration of

the LiO_4 tetrahedra chains and thus alters the energy landscape of the $Li_{1-x}FeBO_3$ phases, though it is expected that the modulation will be absent in delithiated and degraded $LiFeBO_3$, both of which are formed through the loss of Li.

In contrast, as discussed in the previous chapter, our studies suggested that the initial delithaition of $LiFeBO_3$ proceeds *via* a two-phase reaction based on galvanostatic intermittent titration technique (GITT) measurements with longer relaxation times [7]. It was not established whether this two-phase reaction persists across the full range of Li content with end members $LiFeBO_3$ and "$FeBO_3$", or whether intermediate compositions are formed. This remains an open question, due in part to the difficulty in fully relaxing the system to its equilibrium thermodynamic potentials at high states of charge.

A second unresolved question is the origin of the commonly observed low-voltage process (< 2 V) during cycling of $LiFeBO_3$ that is manifested as a discrete plateau at ~1.8 V in GITT data [6b, 7], but whose existence is also discernible in the curvature of other charge-discharge curves at low voltages. A typical $LiFeBO_3$ charge and discharge curve is shown in Fig. 3.1. Starting with an open circuit potential of 2.8 V, charging the sample to 4.5 V results in a specific capacity of only 105 mAh/g, less than the expected full capacity of 176 mAh/g of this sample (80 wt% $LiFeBO_3$, 10 wt% Fe_3BO_5 and 10 wt% C). This charge capacity therefore corresponds to a removal of 0.6 Li per formula. The Li intercalation is clearly reversible, but surprisingly, an extra 0.2 Li can be accommodated in this system at voltages lower than 2 V. This process occurs at a potential of approximately 1 V lower than the Fe^{3+}/Fe^{2+} redox couple in $LiFeBO_3$ (~2.8 V). It can in principle arise from either Fe conversion chemistry (the reduction of Fe^{2+} to Fe metal), a reaction with the degraded phase (designated D-Li_dFeBO_3), or a reaction with an amorphous phase that is formed at low voltage. It is important to identify the origin of this low-voltage

process, which appears to be an integral part of the electrochemical activity of many $LiFeBO_3$ electrode preparations.

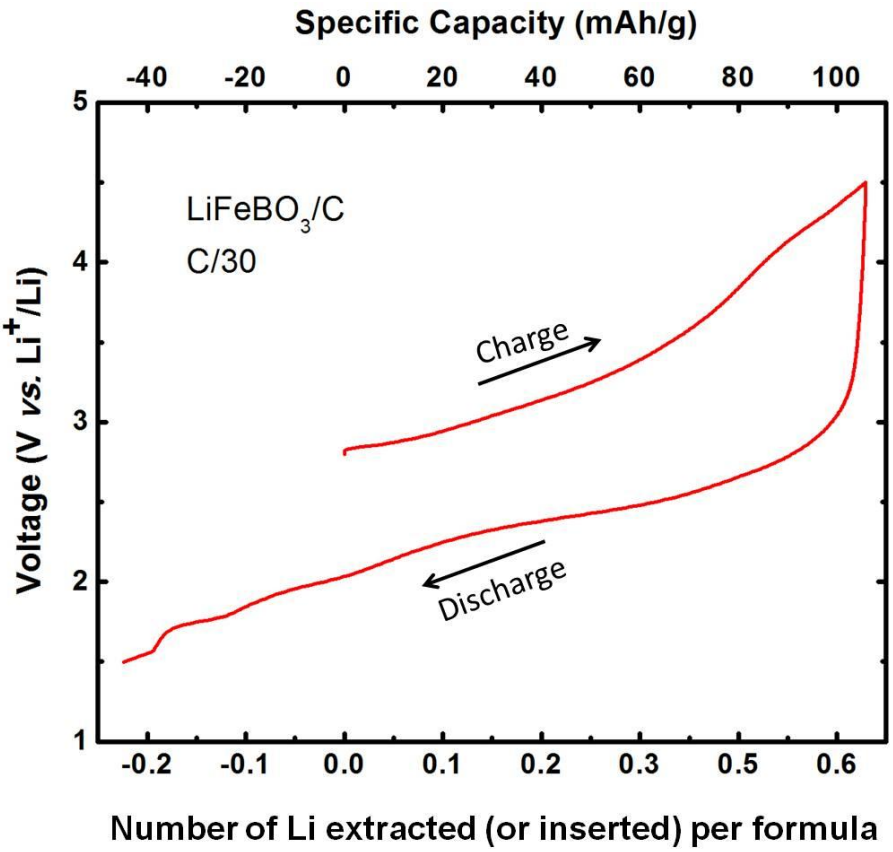

Figure 3.1. Electrochemistry of $LiFeBO_3$ at a rate of C/30 between 4.5 V and 1.5 V. The number of Li extracted (or inserted) per formula was calculated based on a full capacity of 176 mAh/g. The approximate valence of Fe was estimated based on the assumption that iron was divalent after discharge, in accord with XANES results. See Ref 7 for experimental details. Figure is reproduced with permission from Ref 1.

In order to resolve the complex evolution of structural and valence changes associated with $LiFeBO_3$ redox processes, we have used a wide range of complementary structural probes both *in situ* and *ex situ* that go beyond the normal repertoire of laboratory techniques. The *in situ* techniques included high-resolution synchrotron diffraction and synchrotron X-ray absorption fine structure measurements (XAFS). Also, solid state nuclear magnetic resonance (NMR) was employed to probe the local environments of both Li and B ions during electrochemical cycling since structurally similar phases that are difficult to distinguish in diffraction can still give very different NMR signals if their electronic structures vary [10]. Neutron Bragg scattering and pair distribution function (PDF) analysis of total scattering data were used to probe differences in the structures of pristine and degraded $LiFeBO_3$ (D-Li_dFeBO_3). Finally, site occupancies of Fe and Li in the degraded phase were directly probed by high-resolution transmission electron microscopy (HRTEM) imaging at single-particle level. Based on the analysis of results from these (and additional) complementary techniques, a model for the structural and valence changes in $LiFeBO_3$ during the distinct oxidative processes of delithiation and degradation is proposed. Furthermore, we demonstrate that degraded $LiFeBO_3$ is structurally distinct from the pristine $LiFeBO_3$ phase. The degraded phase is electrochemically active and is responsible for the reversible 1.8 V redox process which first occurs during sample discharge (lithiation), since the as-formed degraded phase cannot be further delithiated.

3.2 Experimental

$LiFeBO_3$/C composite: $LiFeBO_3$/C composite was prepared through the solid-state reaction of precursors under an actively reducing atmosphere of forming gas (5% H_2/95% N_2). In

a typical synthesis, 3 g powder precursors of Li_2CO_3 (Mallinckrodt, 99.0% min), $FeC_2O_4 \cdot 2H_2O$ (Alfa Aesar, 99%), and H_3BO_3 (Alfa Aesar, 99.5% min) were mixed in a stoichiometric ratio. Citric acid (Alfa Aesar, 99.5+%) was also added as the carbon source with a carbon content of no more than 20 wt%, where the 20 wt% assumption is based on carbon being produced from citric acid with 100% yield. The powder mixture was ball milled for 30 minutes in a SPEX SamplePrep8000 Mixer/Mill high energy ball mill by the use of a stainless steel jar. The resulting powder was then heated in a graphite crucible that was sealed in a tube furnace. After a dwell at 350 ℃ for 10 hours, the temperature was ramped up to 650 ℃ under a heating rate of 100 ℃ h^{-1}, and kept at 650 ℃ for 20 hours. Reaction products were removed from the furnace and immediately transferred to an argon glove box. The $LiFeBO_3$/C nanocomposite typically contains ~10 wt% Fe_3BO_5 as a major impurity based on X-ray diffraction (XRD) and ~10 wt% C according to thermogravimetric analysis (TGA) results. A broad particle size distribution from a few nanometers to more than 100 nm was observed by scanning electron microscopy (SEM). A thin surface layer of about 2-3 nm of amorphous carbon coating was observed by transmission electron microscopy (TEM) [7].

Isotopic $^{7}LiFe^{11}BO_3$/C composite and degraded isotopic $^{7}LiFe^{11}BO_3$: $^{7}Li^{11}BO_2$ was first synthesized by heating a ~2 g powder mixture of $^{7}Li_2CO_3$ (Sigma-Aldrich, 99 atom % ^{7}Li) and $^{11}B_2O_3$ (ISOTEC, 99 atom % ^{11}B) at 750 ℃ in an alumina crucible for about 2 hours with intermediate grinding. The isotopic $^{7}LiFe^{11}BO_3$/C composite was then synthesized in the same way as in the synthesis of non-isotopic $LiFeBO_3$/C composite. Degraded $^{7}LiFe^{11}BO_3$ was prepared by heating ~1 g powder of the as-prepared $^{7}LiFe^{11}BO_3$/C composite at 100 ℃ or 200 ℃ in air for 2-5 days.

Electrochemistry: Electrochemical testing was done in a 2032-type coin cell using an Arbin battery cycler. The electrolyte was 1 M $LiPF_6$ in a 1:1 volumetric mixture of anhydrous ethylene carbonate (EC) and anhydrous dimethyl carbonate (DMC). For the $LiFeBO_3$ cathode preparation, super P, polyvinylidene difluoride (PVDF) and 1-methyl-2-pyrrolidone (NMP, Sigma-Aldrich, 99.5%) were dried before use. First, 70 wt% active material, 20 wt% super P and 10 wt% PVDF were mixed and ground thoroughly with NMP in an argon glove box. This slurry was cast onto an Al foil and dried in a vacuum oven at 60 ℃ overnight. Circular disks with a diameter ~14 mm were punched with a loading of *ca.* 5-10 mg of electrode materials. The current density was converted into a C rate based on the $LiFeBO_3$ theoretical capacity of 220 mAh/g.

In situ Fe K-edge X-ray absorption spectroscopy (XAS): The Fe K-edge XAS was carried out in transmission mode at beamlines X18A and X18B at the Brookhaven National Laboratory's (BNL) National Synchrotron Light Source (NSLS) using a Si(111) double-crystal monochromator. The beam intensity was reduced by 30% to minimize high order harmonics. The XAS spectra were continuously collected while the *in situ* cell was charged and discharged in a voltage window of 1.5 – 4.5 V using a current density corresponding to C/30 rate. Reference spectra from a Fe metal foil were simultaneously collected for energy calibration. The X-ray absorption near edge spectra (XANES) data were processed using the Athena programs [11]. The extracted extended X-ray absorption fine structure (EXAFS) signal, $\chi(k)$, was weighted by k^2 to emphasize the high-energy oscillations and then Fourier-transformed in a k range from 3.0 – 13.0 Å using a Hanning window function to obtain magnitude plots in R-space (Å). The filtered Fourier transforms of EXAFS spectra in a R-range of 1.1 – 3.1 Å were fitted using theoretical

single scattering paths generated with the FEFF 6.0 *ab initio* simulation code, using the subcell structure of $LiFeBO_3$ (*C2/c*) [2].

In situ high-resolution X-ray diffraction: Electrode pellets of the $LiFeBO_3$/C were prepared by mixing the active material with carbon black (Vulcan XC-72, Cabot Corporation), graphite SFG-6 (Alfa-Aesar) and PTFE binder (Sigma-Aldrich) in the mass ratio 6:1:1:2 and then pressing pellets (10 mm diameter, 120-150 μm thick) at an applied pressure of 1.6 – 1.8 ton. Pellets were assembled into the "AMPIX" electrochemical cell designed for *in situ* measurements[12]. Cells were cycled galvanostatically against lithium at a constant current of 7.3 mA/g (C/30), in the potential range of 4.5 V – 1.5 V. High-resolution X-ray diffraction data were collected in transmission geometry at beamline 11-BM (λ = 0.4134 Å) of the Advanced Photon Source, at Argonne National Laboratory. Calibration of the instrument for wavelength, detector offsets, and instrument profile shapes was performed with a NIST SRM 660a (LaB_6). Data were collected using a multi-analyzer detection assembly, consisting of 12 independent Si (111) crystal analyzers and $LaCl_3$ scintillation detectors, scanned between -2 and 12.0 ° at 0.12 s/step with 0.002 °steps (14 min scan time). Data sets with Q_{max} ~ 9 $Å^{-1}$ were collected at 1 h intervals.

Neutron Bragg diffraction and pair distribution function: Time-of-flight (TOF) neutron Bragg diffraction data was collected at the POWGEN beamline of Spallation Neutron Source (SNS) at Oak Ridge National Laboratory (ORNL). Typically, ~1.5 g of powder was packed into a 6 mm V can. Data was collected at a temperature of 300 K, with a proton pulse rate of 60 Hz. The data spans a d space of 0.41-3.61 Å, and was normalized against proton charge. A typical data collection time of 3-6 hours was used. Neutron total scattering measurements were performed at the NOMAD beamline of the SNS at ORNL[13]. Typically, ~100 mg of powder was packed into a 6 mm V can. One-hour scans were typically collected with a Q_{max} of ~50 $Å^{-1}$. The

pair distribution function (PDF) data were reduced and processed using scripts to normalize the data against a V spectrum from a 6 mm diameter V rod corrected for absorption, diffraction and multiple scattering.

NMR: In the ^{7}Li magic angle spinning (MAS) NMR experiments, a 1.3 mm HX probe (Ago Samoson) was employed on a Tecmag 200 MHz spectrometer with a 4.7 T magnetic field. A rotor-synchronized spin echo sequence ($\pi/2$-τ-π-τ-acquisition) was utilized, with a spinning speed of 50 kHz. The Larmor frequency of ^{7}Li is 77.71 MHz. A pulse width of 2 μs ($\pi/2$) was used. The recycle delay was 100 ms. 1 M LiCl was used as an external chemical shift reference (0 ppm).

The NMR spectra of paramagnetic materials are often broad and analysis is made more complicated by overlapping spinning sidebands manifold even under fast magic angle spinning (MAS). A recently developed pulse sequence, projection-magic angle turning phase adjusted spinning sidebands (pj-MATPASS) was therefore employed to better resolve contributions from different phases [14]. For the pj-MATPASS experiments, the same probe was employed on a wide-bore Oxford 500 MHz (11.7 T) Varian Infinity Plus spectrometer and a 50 kHz spinning speed was used. The pj-MATPASS pulse sequence was adopted from ref. [14] and the starting t_1 was set to be 2/3 of a rotor period to minimize pulse ring-down effects before detection. The $\pi/2$ projection pulse was 1 μs, allowing a broad excitation of the spectra.

HRTEM: High-resolution TEM images were recorded from individual particles of the degraded phase, at 200 kV using a JEOL2100F microscope equipped with a Schottky field-emitter and a high-resolution pole-piece with a 0.23 nm point-to-point spatial resolution. To

assist interpretation of the HRTEM images, image simulations were carried out using our own simulation codes based on the multislice method [15].

3.3 Results and discussion

3.3.1 Phase progression during $LiFeBO_3$ cycling

A broad overview of the changes that occur in bulk $LiFeBO_3$ during cycling was obtained through *in situ* X-ray absorption fine structure measurements at the Fe K-edge. EXAFS measurements are most sensitive to local structure changes, while XANES measurements mostly probe Fe valence. As can be clearly seen in the data and fits to EXAFS spectra collected for the pristine, fully charged and fully discharged samples, the local environment of Fe is minimally changed during electrochemical cycling of $LiFeBO_3$ (Fig. 3.2).

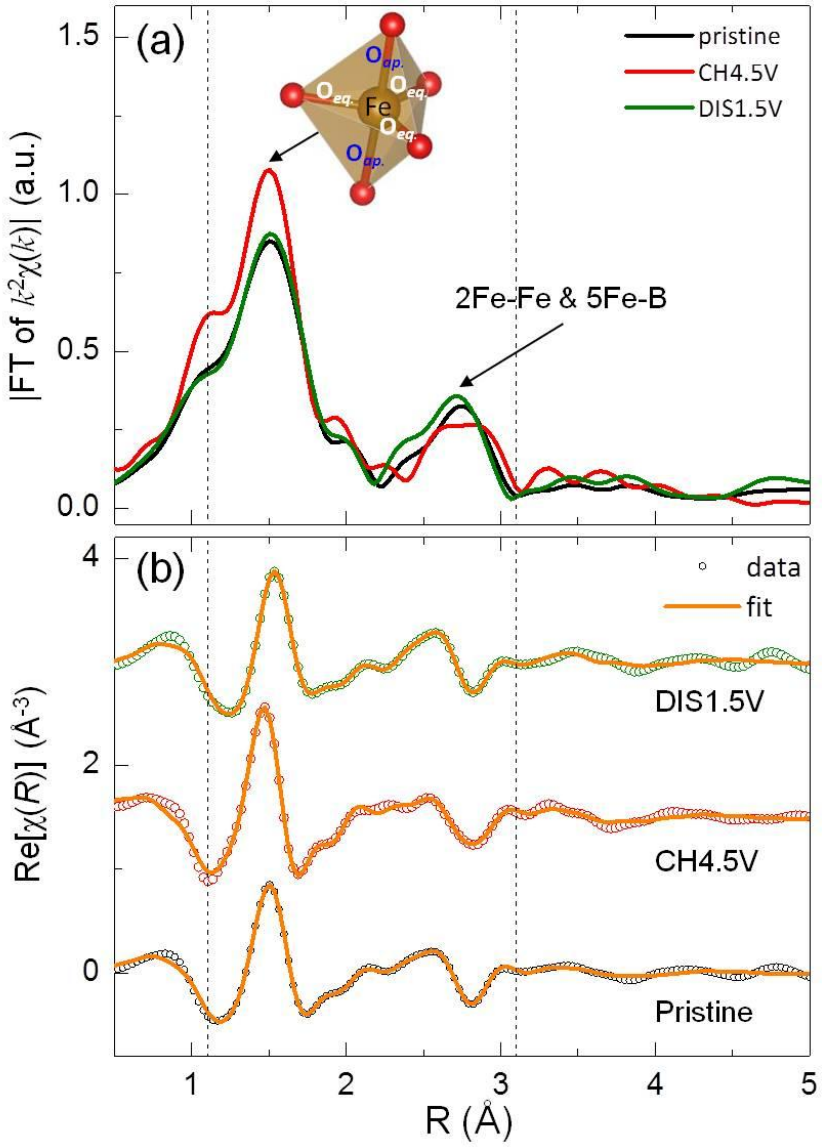

Figure 3.2. (a) Fourier-transformed EXAFS $\chi(k)$ magnitude spectra with k^2 weighting for pristine and cycled $LiFeBO_3$, fully charged to 4.5V ("CH4.5V"), and fully changed and then fully discharged to 1.5V ("DIS1.5V"). (b) Real part of the Fourier-transformed data for the same three scans along with the best fit (orange line). Broken lines indicate the range of the fit in real space (1.1 – 3.1 Å). Data was collected and analyzed in collaboration with Dr. Kyung-Wan Nam from Brookhaven National Laboratory. Figure is reproduced with permission from Ref 1.

The magnitude of the Fourier-transformed (FT) EXAFS spectra for all three samples exhibit one strong peak at ~1.5 Å which corresponds to the five Fe-O bonds in the FeO_5 trigonal bipyramids and another weaker and broader peak at ~2.7 Å which includes both Fe-Fe and Fe-B contributions (Fig. 3.2a). Since the FT was not phase-corrected, the actual bond lengths are expected to be substantially longer (0.3 - 0.5 Å) than these values. Beyond these two FT peaks, no constructive contribution is observed above the noise level. There is no evidence for the formation of metallic Fe since the characteristic Fe-Fe correlations at 2.2 Å (not phase corrected) are not observed in the FT EXAFS spectrum of the fully discharged sample, thus refuting one hypothesis that Fe conversion chemistry (*i.e.*, reduction of Fe^{2+} to Fe metal) may be responsible for the low voltage process observed during the electrochemical cycling of $LiFeBO_3$ (1.5 – 4.5 V).

Insights into the changes in the Fe-O coordination environment that occur during electrochemical cycling were obtained through least-square fitting of the real-part of the EXAFS spectra (Fig. 3.2b). The average Fe-O bond length for the pristine electrode is 2.04 Å. On charging to 4.5 V, this is reduced to 2.01 Å. The subsequent discharge increases the average Fe-O bond length to 2.06 Å. The average Fe-O distance in the fully discharged state appears to be even larger than in the as-prepared electrode (2.06 Å *vs.* 2.04 Å), indicating that the Fe valence has been reduced below its starting value after the discharge to 1.5 V.

The reduction in Fe valence after lithiation (discharge) can be directly resolved by following the shifts in the absorption edge in the XANES portion of the same *in situ* Fe K-edge X-ray absorption data. The progression of phases during the discharge process is presented in Fig. 3.3. At the end of charge (4.5 V), the edge position (B) shifts to higher energy, in comparison to the pristine spectrum, indicating an increase in average Fe oxidation state

approaching 3+ after the charge process. However, based on comparisons with the edge position of reference spectra for $Fe^{II}Cl_2$ and $LiFe^{III}O_2$, Fe is not fully oxidized to Fe^{3+} after charging to 4.5 V, consistent with the incomplete Li extraction shown by the specific capacity (Fig. 3.1). During discharge, the edge position (B) shifts back to lower energy indicating a decrease of the average Fe oxidation state of $LiFeBO_3$. Interestingly, when discharged below 2.5 V (the XANES spectrum of discharged to 2.5 V overlaps with that of the pristine sample), the edge position shifts to energies that are even lower than the position of pristine $LiFeBO_3$. At the end of discharge, the edge position is almost identical to that of the reference $Fe^{II}Cl_2$ compound suggesting that the electrode contains essentially just Fe^{2+}. This shows that the extra capacity obtained below 2.5 V during the first discharge is due to the reduction of higher valence iron species that existed in the original as-prepared electrode.

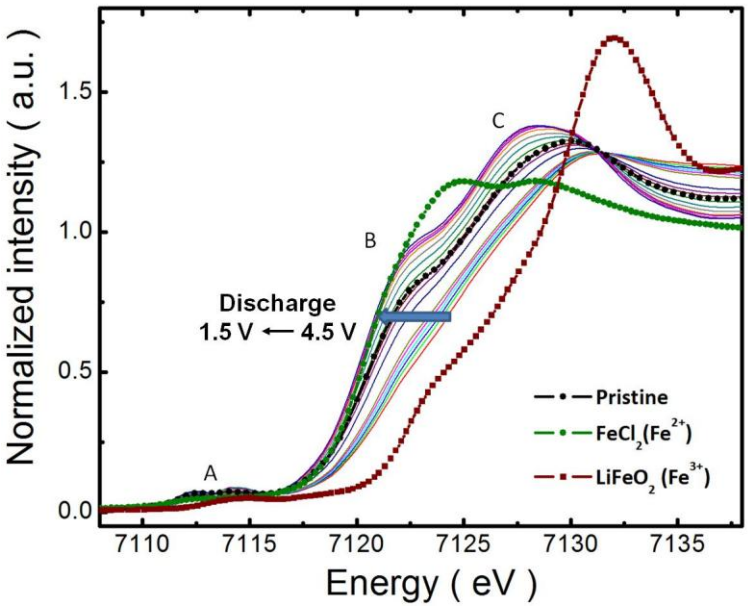

Figure 3.3. *In situ* XANES spectra of $LiFeBO_3$ during the discharge. The spectra of pristine $LiFeBO_3$ and the reference compounds ($Fe^{II}Cl_2$ and $LiFe^{III}O_2$) are shown for comparison. Data

was collected and analyzed in collaboration with Dr. Kyung-Wan Nam from Brookhaven National Laboratory. Figure is reproduced with permission from Ref 1.

At first glance, there appeared to be several crossing points (circled in Fig. 3.4) in the XANES spectra during the first cycle, though a closer look reveals that these crossing points between successive scans shift in spectra that were collected near the end of charge and discharge, as highlighted in Fig. 3.5. This suggests that two primary types of Fe local environments are present during the cycling process, one associated with Fe^{2+} and the other associated with Fe^{3+}. The presence of crossing points at the early stages of charge might be taken to indicate that lithium extraction proceeds only *via* a two-phase reaction between $LiFeBO_3$ and $FeBO_3$, but our prior GITT data and current ^{7}Li NMR experiments (discussed below) strongly suggest that this is not the case. Difficulties in distinguishing between intermediate phases with very similar local environments have been seen in previous XAS studies [16], a situation which is very applicable to the delithiated phases of $LiFeBO_3$ given the observed similarities in both the local Fe environment seen in the EXAFS spectra discussed previously and in the very small changes in the unit cell lattice parameters determined from *in situ* XRD measurements (discussed later).

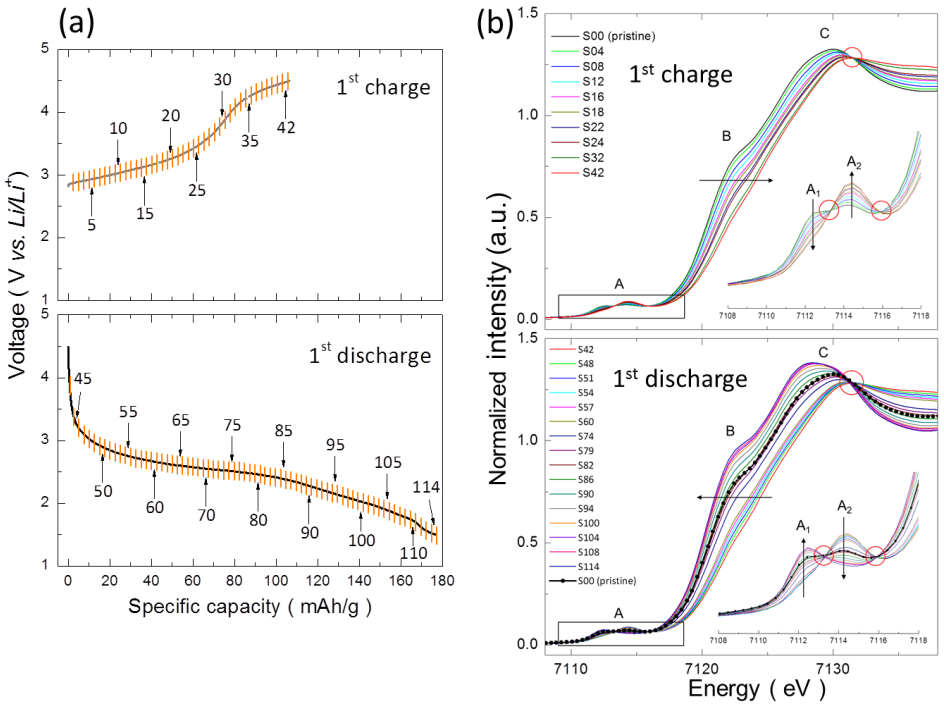

Figure 3.4. (a) Charge and discharge curves and (b) corresponding *in situ* Fe-K edge XANES spectra. The cell was cycled at C/30 (based on theoretical capacity of 220 mAh/g), and *in situ* spectrum numbers are marked on the curves in (a). Data was collected and analyzed in collaboration with Dr. Kyung-Wan Nam from Brookhaven National Laboratory. Figure is reproduced with permission from Ref 1.

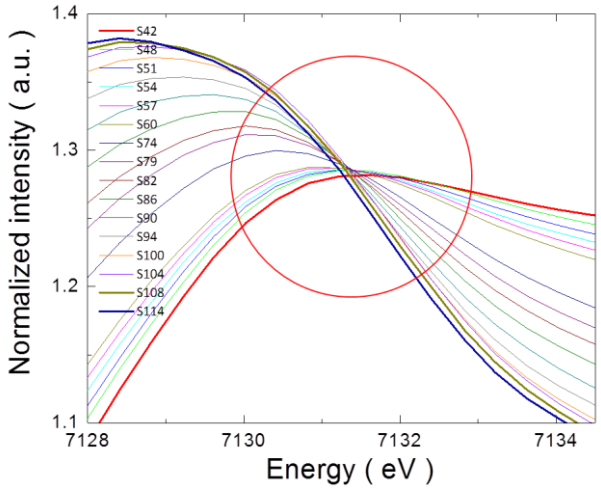

Figure 3.5. Enlarged region of the crossing point at ~7131.5 eV in the *in situ* XANES spectra during discharge. It was found that spectra (highlighted in bold lines) corresponding to both the highest voltages ~ 4.5 V (S108 and S114) and the lowest voltage ~ 1.5 V (S42) were slightly offset from the crossing point, though the latter cannot definitively be assigned as an inherent difference due to a gap in the time of the data collection of S42. Data was collected and analyzed in collaboration with Dr. Kyung-Wan Nam from Brookhaven National Laboratory. Figure is reproduced with permission from Ref 1.

The local environment of Li can be directly probed by the complementary technique of ^{7}Li NMR since the ^{7}Li signal is influenced by both the coordination geometry and valence of nearby Fe ions, and as such is able to very sensitively resolve the succession of phases that occur when $LiFeBO_3$ is cycled. The NMR responses from multiple phases ($LiFeBO_3$, $Li_{1-x}FeBO_3$, and D-Li_dFeBO_3) involved in the electrochemical processes are distinct, and their resonances and stoichiometry assignments will be discussed in the following two paragraphs.

^{7}Li MAS NMR spectra of $LiFeBO_3$ samples prepared by cycling equivalent batteries to different states of charge and discharge are shown in Fig. 3.6. At the initial open circuit voltage (OCV), the sample is characterized by three ^{7}Li resonances, a $LiFeBO_3$ resonance at -233 ppm (yellow line) and two other resonances for secondary phases resulting from the degradation of $LiFeBO_3$: at +218 ppm (red line), the oxidized and degraded phase D-Li_dFeBO_3, and at 0 ppm, a Li-containing diamagnetic phase which contains the Li lost from the $LiFeBO_3$ lattice during degradation. These assignments were made in our previous study by studying samples with different overall contents of the degraded phase [7]. All the other observed peaks are spinning sidebands, which are caused by partially averaging the anisotropic dipolar interaction between Li nuclei and unpaired electrons associated with Fe^{2+} and/or Fe^{3+} *via* the magic angle spinning. Note that any signals from residual electrolyte ($LiPF_6$) and the surface electrolyte interphase (SEI) found in the cycled samples are also diamagnetic and thus have resonances around 0 ppm. These contributions cannot be ignored in interpreting the intensity variation of 0 ppm signal.

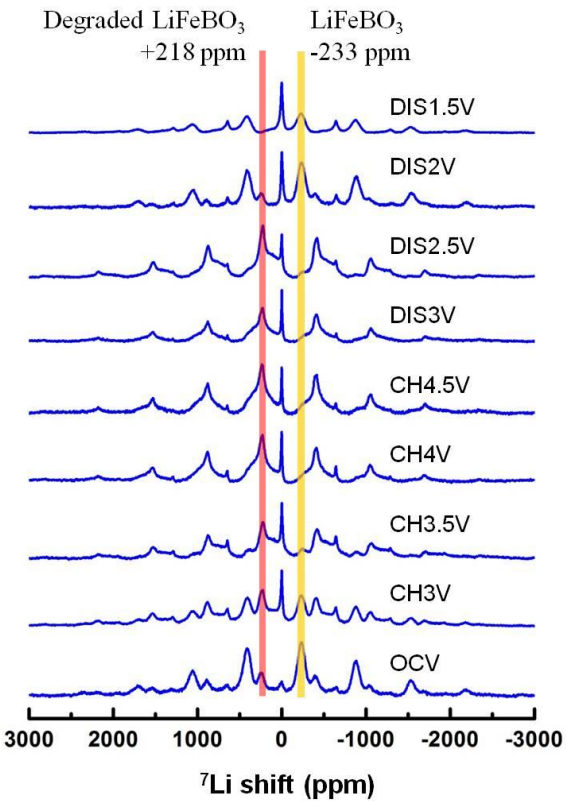

Figure 3.6. ^{7}Li MAS NMR spectra of $LiFeBO_3$ samples at different stages of cycling. Figure is reproduced with permission from Ref 1.

During the cycling process, another broad feature assigned to the partially delithiated phase $Li_{1-x}FeBO_3$ appears (during charge) and disappears (during discharge) in the frequency regime around +218 ppm. This broad feature has a more positive hyperfine shift in comparison to the original $LiFeBO_3$ resonance (-233 ppm), suggesting that it is associated with Fe-containing phase with a higher oxidation state (*i.e.*, > 2).

During the first charge process to 4.5 V, the $LiFeBO_3$ resonance at -233 ppm rapidly decreases in intensity and has almost disappeared at 4.5 V when only 0.6 Li have been removed.

There is no resolvable shift of the $LiFeBO_3$ resonance between the OCV and 4.5 V, in contrast to the shift or distribution of resonances that might be expected if a continuum of phases, *i.e.*, a solid solution $Li_{1-x}FeBO_3$ existed. Also of note is that the broad feature assigned to Li in a partially delithiated ($Li_{1-x}FeBO_3$) lattice appears and grows as a shoulder to the right of the +218 ppm peak (~100 ppm) at early stages of charge (CH3V with a removal of 0.15 Li and CH3.5V with a removal of 0.4 Li). This $Li_{1-x}FeBO_3$ resonance grows to its maximum intensity at around 3.5 V to 4 V (~0.5 Li removal), where the $LiFeBO_3$ resonance nearly disappears. It suggests that delithiation of $LiFeBO_3$ starts with a two-phase reaction whose other end member is suggested to be Li_tFeBO_3 with $t \sim 0.5$ based on capacity estimates and crystal chemistry arguments (represents the simplest periodicity that can be stabilized by charge order). The assignment of a $LiFeBO_3$–$Li_{0.5}FeBO_3$ two-phase region is also consistent with our prior GITT measurements which indicate a clear 2.8 V plateau at both the beginning of charge and at the latter stages of discharge [7].

When the $LiFeBO_3$ battery is charged above 4V, the broad feature shifts to more positive frequency (approximately +250 ppm) as signified by the appearance of a shoulder to the left of the +218 ppm peak. This further shifted resonance is therefore assigned to a further delithiated phase with a general solid solution formula of $Li_{t-x}FeBO_3$ ($0 < x < t$). A closer look at the spectrum of CH4.5V reveals that a small portion of $LiFeBO_3$ still remains at the end of charge, indicating that the solid solution reaction between $Li_{0.5}FeBO_3$ and $Li_{0.5-x}FeBO_3$ starts before $LiFeBO_3$ is fully converted to $Li_{0.5}FeBO_3$. This is consistent with the high overpotential (> 0.5 V, Fig. 3.1) needed to drive the delithiation of $LiFeBO_3$, and the relatively small potential difference between the electrochemical features associated with the $LiFeBO_3$-$Li_{0.5}FeBO_3$ two-phase reaction and the $Li_{0.5}FeBO_3$-$Li_{0.5-x}FeBO_3$ solid-solution reaction (~0.25 V based on prior GITT

data from first discharge) [7]. The large overpotential is likely caused by either the broad size distribution of the pristine $LiFeBO_3$ particles where the core of bigger particles are difficult to delithiate due to transport limitations, or the appearance of secondary phases at the particle surface resulting from degradation or SEI formations which can impede Li^+ and/or e^- transport. All of the NMR hyperfine shift and intensity changes associated with the structural conversions between the pristine phase and the delithiated phases are reversed during the discharge (above 2 V), suggesting that phase progression is the same during charge and discharge, a conclusion consistent with the observed electrochemical behavior of $LiFeBO_3$.

A separate experiment was carried out to determine if $LiFeBO_3$ can be fully delithiated to form "$FeBO_3$". Using a cut-off voltage of 4.5 V, a $LiFeBO_3$ battery was first galvanostatically charged to 4.5 V under a rate of C/30 and then held at 4.5 V until the current decayed to C/3000 about 2 days later (Fig. 3.7). When the resulting product was studied using ^{7}Li NMR to test if Li was still present in an iron borate lattice, the $Li_{0.5-x}FeBO_3$ resonance at ~250 ppm (left shoulder to the +218 ppm peak of the degraded phase) could still be seen confirming that not all Li has left the lattice. This highlights the difficulty of fully delithiating $LiFeBO_3$ to form "$FeBO_3$" (up to 4.5 V). Based on the specific capacity, the final composition after the extended 4.5 V hold is estimated to be $Li_{0.2}FeBO_3$. Even after this extended high voltage hold, the degraded phase ^{7}Li resonance appears unchanged (same chemical shift, peak remains relatively sharp) suggesting that although Li is present in the degraded phase, this Li cannot be electrochemically extracted even under very harsh conditions (*i.e*, prolonged voltage hold at 4.5 V). However, it appears that lithium can be inserted into the degraded phase by discharging to low voltages (< 2 V) since the intensity of the ^{7}Li NMR resonance at +218 ppm was reduced at 2 V and essentially disappeared at 1.5 V during the *ex situ* cycling experiments (Fig. 3.6).

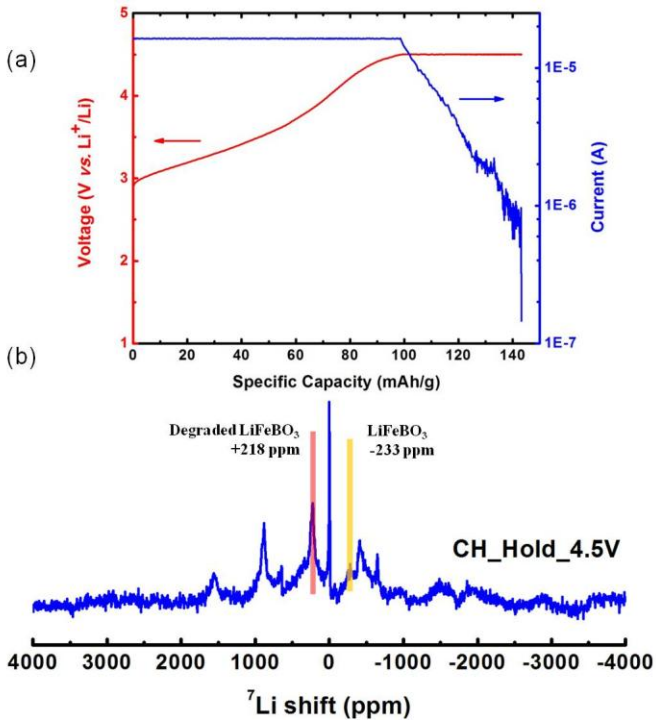

Figure 3.7. (a) Electrochemistry of a $LiFeBO_3$ sample charged to 4.5 V at a rate of C/30 and held at 4.5 V until the current decayed to C/3000 (axis of current is on a logarithmic scale). (b) ^{7}Li MAS NMR of the product after charging. Figure is reproduced with permission from Ref 1.

Synchrotron *in situ* XRD was used to follow the bulk structural changes of $LiFeBO_3$ during cycling (charge to 4.5 V, discharge to 1.5 V, and second charge to 3.5 V) under actual operating conditions without any of the relaxation phenomena associated with *ex situ* experiments. As seen in Fig. 3.8, only very small changes in peak positions and intensities occur, suggesting that the structural framework of $LiFeBO_3$ is retained throughout the cycling. The diffraction data were analyzed through Rietveld refinements to extract two pieces of information: (1) the phase fractions of pristine and delithiated $LiFeBO_3$, and (2) the Li-content dependent lattice parameter variations of delithiated $LiFeBO_3$. The structure of pristine $LiFeBO_3$ is very

well known from single crystal X-ray diffraction experiments and was used without further refinement of atomic parameters or cell parameters though the C2/c approximant was used rather than the full C2/c(½00)00 superspace group. Given the minimal changes in X-ray peak intensities during cycling and the very small scattering power of Li, B, and O, the same $LiFeBO_3$ structural model was also utilized to describe the partially delithiated phase (*i.e.*, $Li_{1-x}FeBO_3$) and the lattice parameters of this phase were refined at each step during electrochemical cycling. The fitting was further aided by (1) very effectively modeling the cell background in a parametric manner, and (2) utilizing a robust refinement algorithm [17,18] to minimize the adverse impact of components not formally included in the refinement (in particular, the variable composition degraded phase).

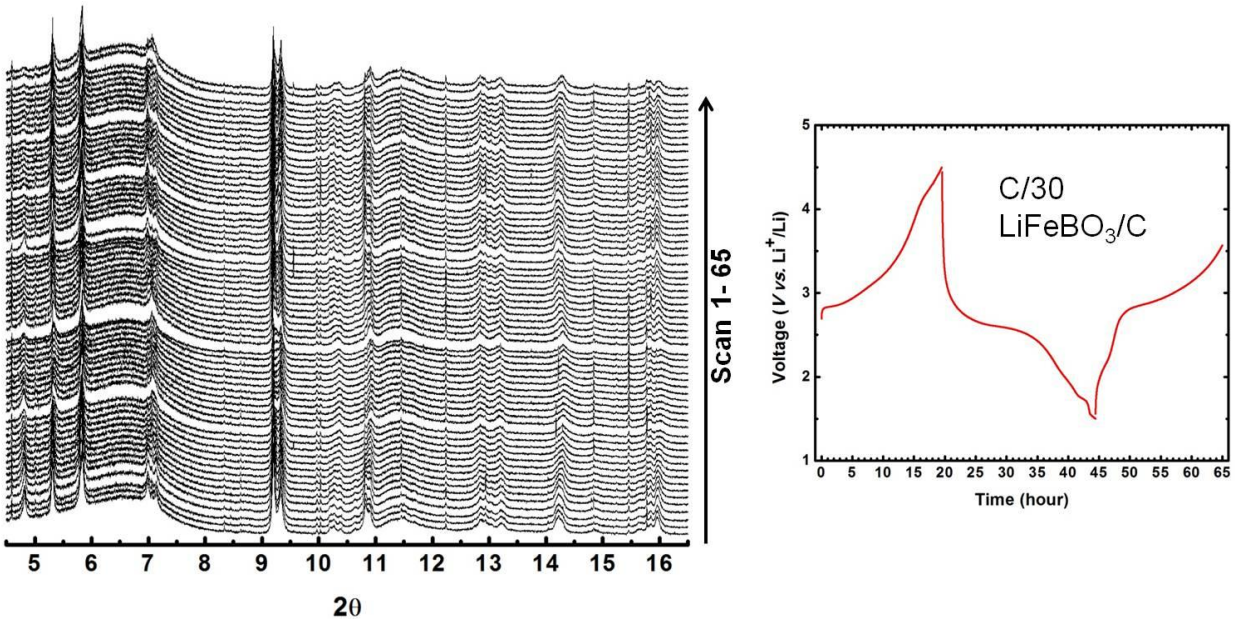

Figure 3.8. *In situ* XRD patterns of $LiFeBO_3$ during cycling (left) and the corresponding electrochemical response (right). Data were collected every one hour with a wavelength of ~0.41 Å. Figure is reproduced with permission from Ref 1.

The phase fractions of three phases present in electrodes ($LiFeBO_3$, $Li_{1-x}FeBO_3$ and Fe_3BO_5) are shown in Fig. 3.9, while the graphical fits of some selected scans are presented in Fig. 3.10. As expected, the fraction of the pristine phase decreases during the charge process (to a minimum value of ~10%) and increases during discharge, while the trend of the delithiated phase is inverted. Although freely refined, it can be seen that the mass fraction of the Fe_3BO_5 impurity remains constant (within 2%), indicating that the refinement is well behaved and that amorphization of the electrochemically active phases is not occurring. At voltages below 2 V, there is no change in the phase fractions of $LiFeBO_3$ and $Li_{1-x}FeBO_3$, indicating that the low voltage electrochemical processes (<2 V) do not involve $LiFeBO_3$, and instead result from electrochemically induced changes in the degraded phase D-Li_dFeBO_3, a conclusion confirmed by the ^{7}Li NMR data that is described in Fig. 3.11.

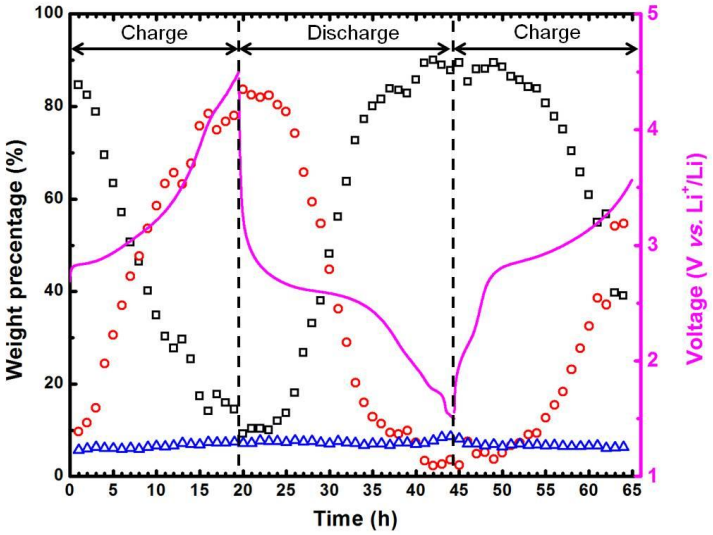

Figure 3.9. Weight percentages of $LiFeBO_3$ (black), $Li_{1-x}FeBO_3$ (red) and Fe_3BO_5 (blue) during cycling in the *in situ* run. The electrochemistry profile is shown in magenta with the voltage axis on the right. Figure is reproduced with permission from Ref 1.

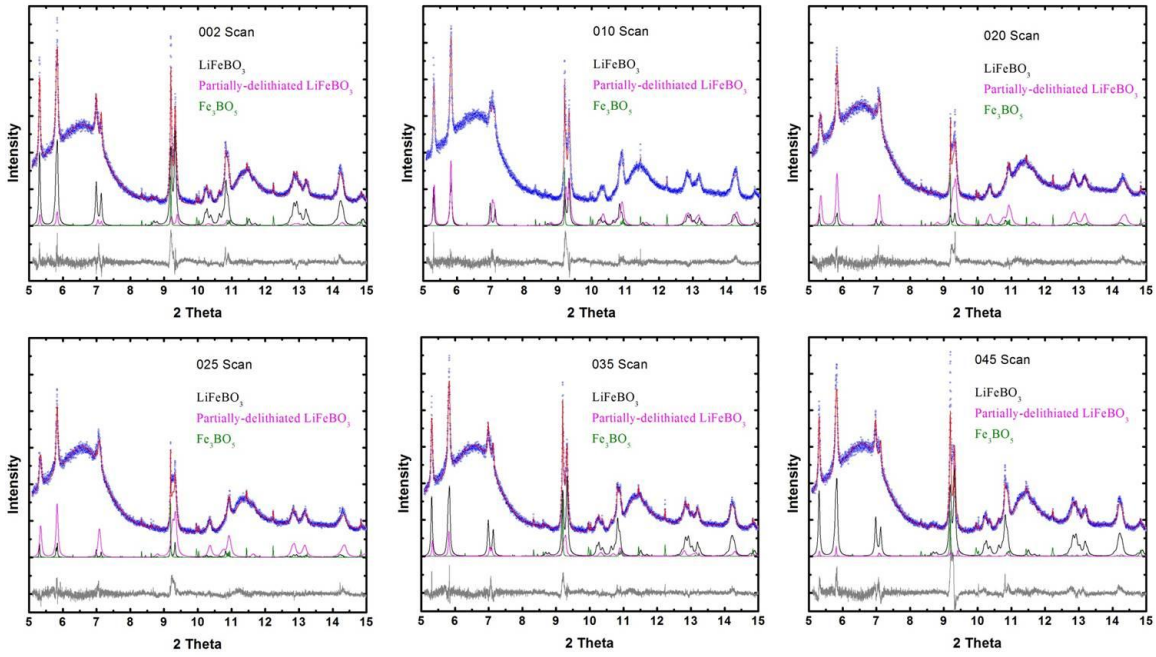

Figure 3.10. Rietveld refinement of the diffraction patterns for the first $LiFeBO_3$ charge (scans 002, 010, and 020) and discharge (025, 035, 045). Observed, calculated, and difference curves

are in blue, red and grey respectively. The separate contributions of $LiFeBO_3$, partially delithiated $Li_{1-x}FeBO_3$, and Fe_3BO_5 are plotted in black, magenta and dark green, respectively. Figure is reproduced with permission from Ref 1.

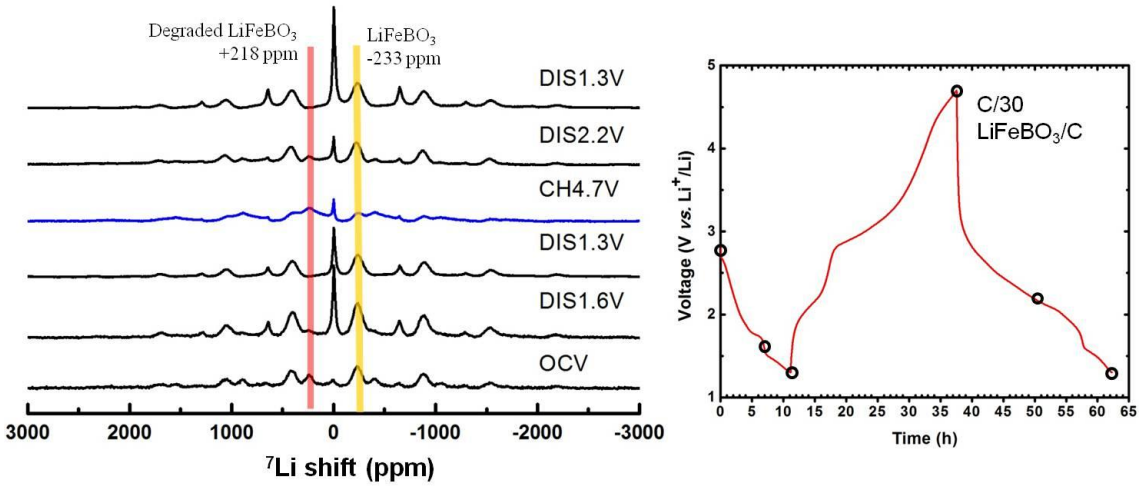

Figure 3.11. ^7Li MAS NMR spectra of $LiFeBO_3$ samples at different states of charge and discharge. The cell was discharged first in order to remove the degraded $LiFeBO_3$ (Li_dFeBO_3). This discharge process almost completely removed the ^7Li signature of Li_dFeBO_3. The electrode was then charged to 4.7 V and discharged again to 1.3 V. The disappearance of the Li_dFeBO_3 resonance during the first and second discharge, and its reappearance during charge (seen more clearly on the subsequent discharge to 2.2 V) demonstrate the reversibility of the electrochemistry process involving the degraded phase, Li_dFeBO_3. Figure is reproduced with permission from Ref 1.

The lattice parameters and unit cell volume of delithiated $Li_{1-x}FeBO_3$ at voltages above 2 V (where the weight percentage of the $Li_{1-x}FeBO_3$ phase is 10% or more) are plotted in Fig. 3.12.

It can be seen that the cell volume is reduced by no more than 1.6% relative to pristine $LiFeBO_3$, and that the majority of the change occurs for the *b*-axis. Although the changes in the β angle are small, they represent a substantial movement towards the ideal value of 90 °. These results are consistent with both theory and prior experimental measurements [2, 9], and again demonstrate that there are minimal changes in the $LiFeBO_3$ lattice during cycling.

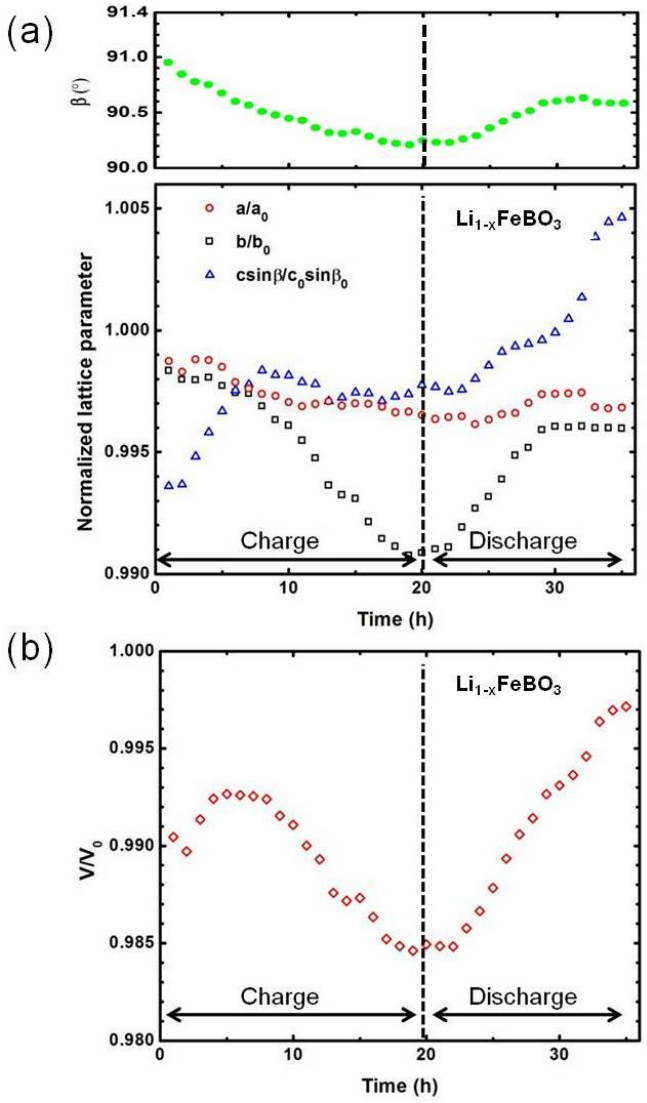

Figure 3.12. (a) Normalized lattice parameters of $Li_{1-x}FeBO_3$ during cycling. The distance *c*sinβ is plotted instead of *c* since this product is the interlayer spacing. The top panel displays the

progression of the β angle during cycling. The normalized volume is shown in (b). The normalization is against lattice parameters of $LiFeBO_3$ (a_0 = 5.1627 Å, b_0 = 8.9217 Å, c_0 = 10.1746 Å, β_0 = 91.381 °and V_0 = 468.50 $Å^3$). Figure is reproduced with permission from Ref 1.

The structural changes that occur during cycling in the low voltage process are not amenable to refinement due to the small volume fraction of the degraded phase (further discussed in the next section) and strong peak overlap with the major phase. The overall changes in peak position and intensity are quite small. However, it appears that discharge below 2 V causes a small increase in the *c*-lattice parameter of the electrochemically active phase during the lithiation process. This is evidenced by the reversible shift of the *004* peak (in the *C2/c* subcell setting) in the XRD scans covering the low voltage redox process (scans 40-50, highlight in red in Fig. 3.13).

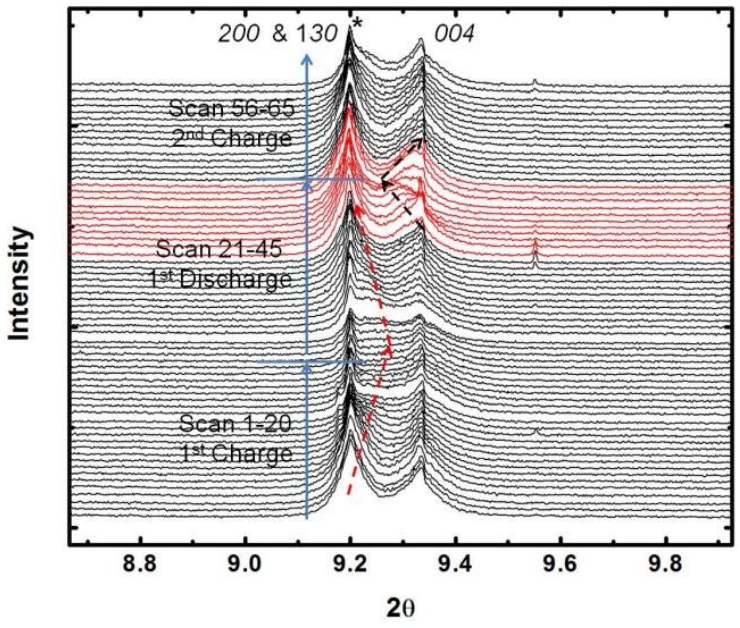

Figure 3.13. In situ XRD patterns of $LiFeBO_3$ during electrochemical cycling (65 scans in total), with a wavelength of ~0.41 Å. The black curves represent the electrochemical processes occurring for $Li_{1-x}FeBO_3$ which primarily involve shifts of the *130* peak (obscured by the Fe_3BO_5 peak indicated by the * at 9.2 °). This shift (indicated by red dotted line) is primarily induced by a change in the *b*-axis length for a monoclinic cell with a β angle close to 90 °. The red curves (scans 40 - 50) highlight electrochemical processes occurring in D-Li_dFeBO_3 which involve *004* peak shifts. This shift (indicated by black dashed line) is driven by changes in the c-axis length. Figure is reproduced with permission from Ref 1.

3.3.2 Electrochemical activity of degraded $LiFeBO_3$

Evidence for the electrochemical activity of the degraded phase, D-Li_dFeBO_3, is provided by the ^{7}Li NMR, *in situ* XRD, and electrochemical cycling experiments discussed above. This redox process occurs at low voltages (< 2V), and the D-Li_dFeBO_3 – D-$Li_{d+y}FeBO_3$ redox couple

is therefore expected to be the source of the 1.8 V plateau in the GITT data reported previously[7]. In order to better understand this electrochemical process, experiments focused on this low voltage region have been carried out to investigate the reversibility of this process, to probe the structural and compositional changes that this process induces, and to explore the structural transformation pathways between the degraded and pristine phases. Accordingly, experiments have been carried out both on electrodes prepared from pristine $LiFeBO_3$, and on highly degraded samples prepared by heating $LiFeBO_3$ in air at 100 ℃ (for over a week) until the characteristic X-ray diffraction peaks of the pristine phase were suppressed.

The electrochemical performance of electrodes prepared from highly degraded samples (Fig. 3.14) share some common features with those prepared from pristine $LiFeBO_3$, even though there are substantial differences in the observed response. The degraded sample exhibits a net capacity of 140 mAh/g, which is divided between high voltage (~2.8 V) and low voltage processes (~1.8 V) in a manner similar to pristine samples, but with a substantially larger fraction of the total capacity occurring at low voltage. The charge curves during the first nine cycles are closely superimposed, indicating good reversibility. In contrast, the initial discharge curves deliver a significantly reduced voltage relative to later cycles indicating that the battery performance substantially improves upon cycling. These changes are much more pronounced in the high voltage regime (~2.8 V) associated with the pristine phase than in the low voltage regime (~1.8 V) associated with the degraded phase.

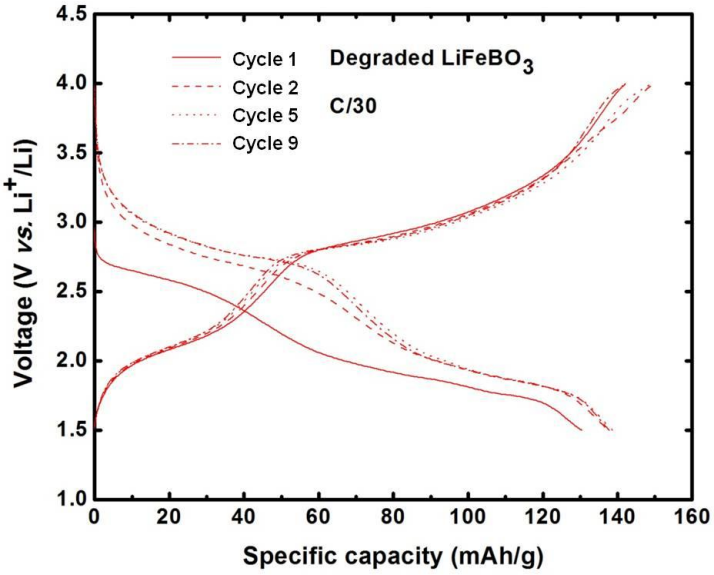

Figure 3.14. Electrochemical performance of highly degraded $LiFeBO_3$. Starting with discharge, the cell was cycled between 1.5 V and 4 V at a rate of C/30 calculated based on an assumed capacity of 220 mAh/g (*i.e.*, full capacity of $LiFeBO_3$). Figure is reproduced with permission from Ref 1.

The differences between pristine and degraded $LiFeBO_3$ can be highlighted in dQ/dV plots (Fig. 3.15). For the pristine sample, the primary ~2.8 V electrochemical features show up on charging at 2.82 V (sharp peak, likely associated with a two-phase reaction between $LiFeBO_3$ and $Li_{0.5}FeBO_3$) and at 2.98 V (broad peak, likely associated with $Li_{0.5}FeBO_3$–$Li_{0.5-x}FeBO_3$ solid solution), but these features shift substantially lower to 2.48 V on discharge and are found further from the thermodynamic plateau of ~2.8 V observed in GITT measurements. The degraded sample also shows electrochemical features in this potential range , which are attributed to the presence of a substantial quantity of $LiFeBO_3$ that has been oxidized (delithiated) but not degraded. Interestingly, the sharp features associated with the pristine $LiFeBO_3$ redox process

(~2.8 V) on charge (2.83 V) and discharge (2.74 V) are separated less in the degraded sample than in the pristine sample suggesting that a barrier to Li insertion has been removed. This is either caused by the use of lower cutoff voltage for charging, or likely by the further reduction of particle size of the pristine $LiFeBO_3$ phase *via* the degradation process.

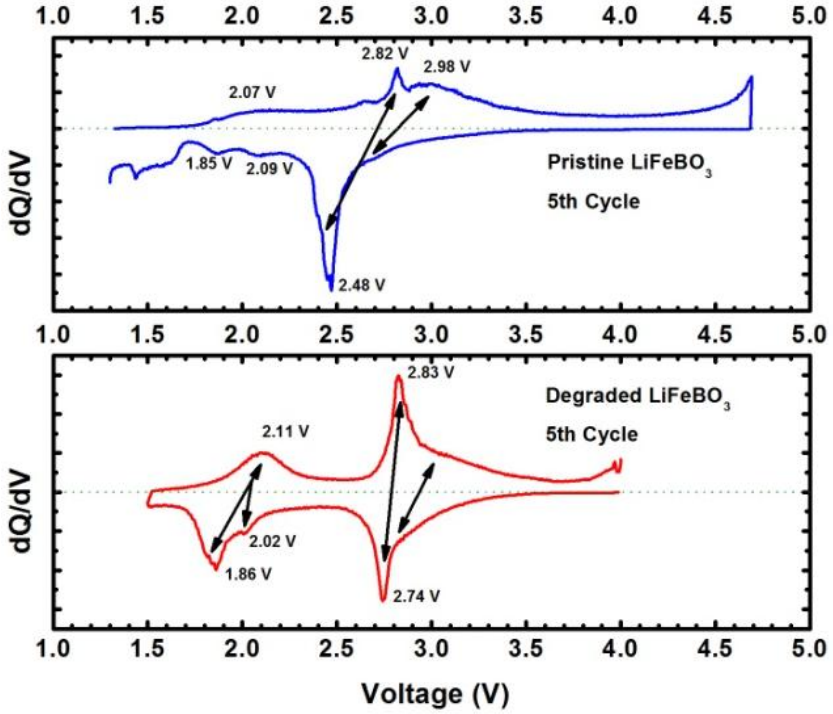

Figure 3.15. Comparison of 5th cycle *d*Q/*d*V data for electrodes prepared from pristine $LiFeBO_3$ (blue) and highly degraded $LiFeBO_3$ (red) showing that common high voltage (~2.8 V) and low voltage (~1.8 V) processes occur in both. Arrows indicate related charge and discharge events. Figure is reproduced with permission from Ref 1.

The low voltage (~1.8 V) processes ascribed to the degraded phase are present in electrodes prepared from both pristine and degraded $LiFeBO_3$, though they are more clearly

resolved in the degraded phase dQ/dV data, presumably due to the larger volume fraction of this low-voltage process. These features suggest that the degraded phase is present even in electrodes carefully prepared from the pristine phase, in agreement with the NMR results. Furthermore, the low voltage processes are very closely aligned for the two different samples and do not exhibit the large shift seen for the ~2.8 V process. The low operating voltage of the degraded $LiFeBO_3$ phase limits its potential use as a cathode candidate although the substitution of Fe by other ions (Mn or Co) which have redox processes at higher voltages might result in electrochemistry suitable for battery applications.

3.3.3 Structure of degraded $LiFeBO_3$

The product of $LiFeBO_3$ degradation appears to be a phase that is structurally very similar to pristine $LiFeBO_3$, yet there is no evidence that pristine $LiFeBO_3$ can be regenerated from degraded $LiFeBO_3$ *via* electrochemical Li insertion at room temperature. The similarity of these phases can be inferred both from present and prior X-ray diffraction measurements that find only minor peak shifts and intensity changes when pristine $LiFeBO_3$ is subjected to degradation-inducing conditions. In the case of nanoparticles, this could be just prolonged air exposure, though for larger particles (> 1 micron) heat treatment (100 – 200 ℃) is generally required to eliminate the presence of X-ray diffraction peaks characteristic of pristine $LiFeBO_3$. The very different kinetics for different particle sizes suggests that the degradation process involves Li diffusion and Li loss through oxidation. We also find that the degradation process requires exposure to O_2, but not to H_2O, and therefore is unlikely to involve the formation of hydroxides or other hydrogen-containing species (Fig. 3.16). This is further supported by neutron

diffraction data collected on the degraded phase, which show no evidence of incoherent scattering from hydrogen in the background.

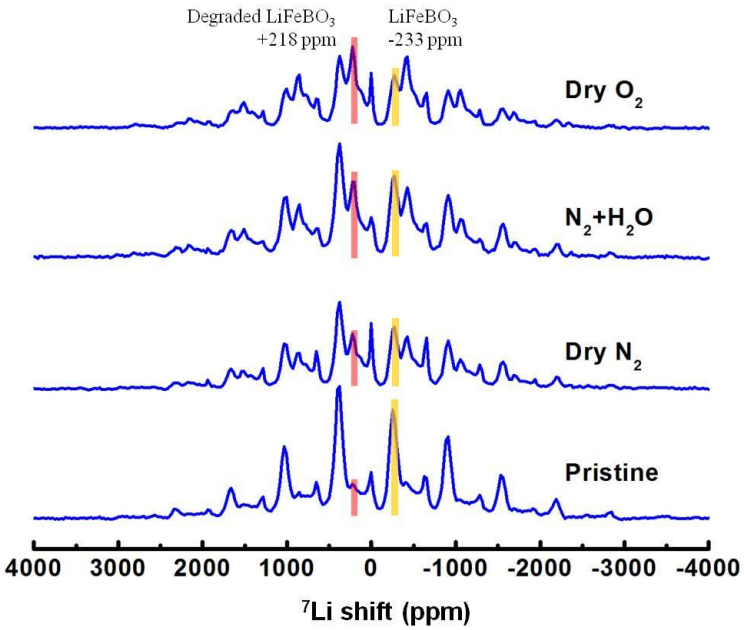

Figure 3.16. ^{7}Li MAS NMR spectra of pristine $LiFeBO_3$ and samples that were heated at 100 ℃ overnight under different atmospheres (Dry N_2, N_2 + H_2O and Dry O_2). Figure is reproduced with permission from Ref 1.

The structural similarity of pristine and degraded $LiFeBO_3$ on the local scale is apparent in neutron pair distribution function (PDF) studies, which were carried out on isotopic $^{7}LiFe^{11}BO_3$ samples to avoid problems with absorption. In contrast to X-ray scattering experiments which are far more sensitive to Fe than the other elements in $LiFeBO_3$, neutron scattering techniques provide good sensitivity to Fe, B, and O but not Li (coherent scattering lengths in fm are: ^{7}Li: -2.22; Fe: 9.45; ^{11}B: 6.65; O: 5.80). A comparison of the pair distribution

function, G(r), generated from the total scattering analysis of neutron diffraction data from both pristine and degraded $LiFeBO_3$ is given in Fig. 3.17. The pairwise atomic correlations (*i.e.*, peak positions) of these two samples in the real space G(r) data are similar at all length scales. While peak intensities remain quite similar at distances corresponding to the local nearest neighbor coordination shells (1.3 Å for B-O bonds, 2.0 to 2.2 Å for Fe-O bonds, 2.4 Å for O-O pairs, and 3.1 Å for Fe-B neighbors in the cation planes), there are more noticeable differences in peak intensity at distances beyond 5Å. The Fe-O bond lengths appear to be reduced after degradation, as expected for an oxidative process which will result in higher valence iron with a smaller ionic radius. There is no evidence of peak shifts that would indicate a large change in the coordination environment of Fe, B, or O. The change in G(r) peak intensities can therefore be attributed to small shifts in position or changes in occupancy of the original atomic sites in pristine $LiFeBO_3$.

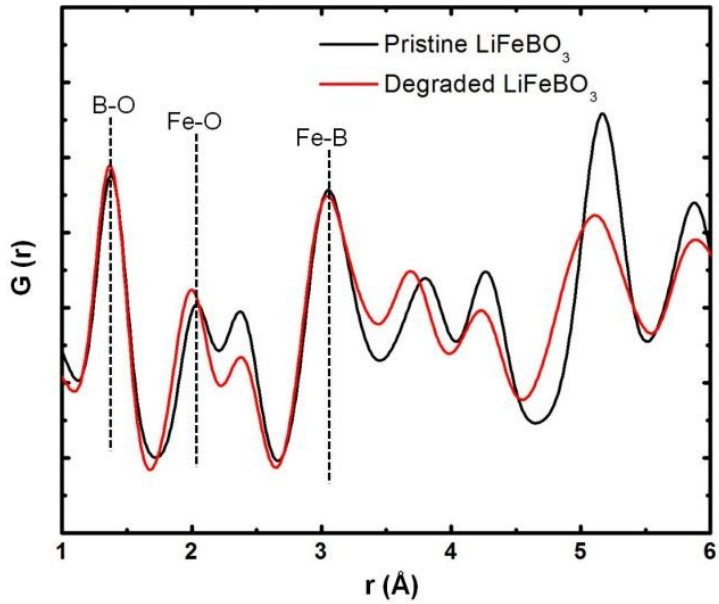

Figure 3.17. Neutron PDF data from pristine (black) and degraded (red) $LiFeBO_3$ powders which were degraded by heating at 100 ℃ for 4 days until diffraction peaks from the pristine phase disappeared. Figure is reproduced with permission from Ref 1.

Since both the Fe local environment and the overall nature of the borate framework appear to be essentially unchanged by the degradation process, the dramatically lower redox potential of the degraded phase (~1.8 V vs. ~2.8 V in the pristine $LiFeBO_3$) cannot be simply explained. The radical change in electrochemical properties is almost certainly related to structural changes that occur during the degradation process. Neutron diffraction experiments were therefore undertaken with the goal of determining the structure of the degraded phase. These refinements were made challenging by the relatively broad peaks and relatively weak diffraction peaks of the degraded phase, as well as the unavoidable co-existence of a delithiated phase whose diffraction peaks strongly overlap with those of the degraded phase. The inhomogeneity (*i.e.*, the multiphase nature) of the degradation process can be clearly seen when

$LiFeBO_3$ is heated isothermally at 200 and 240 ℃ under dry flowing O_2 (Fig. 3.18). It can be seen in both cases that the reaction rate unexpectedly accelerates in the midst of the isothermal hold, suggesting that the initial partial oxidation of $LiFeBO_3$ (mass gain ~2.0% which is substantially less than the expected gain of 6.6% for full oxidation) unlocks a distinct second oxidative process which can occur more rapidly despite the constant sample temperature. The conclusion that both degraded and delithiated $LiFeBO_3$ form during the degradation process is also supported by $^{7}Li/^{11}B$ NMR measurements, which will be discussed in the following paragraphs.

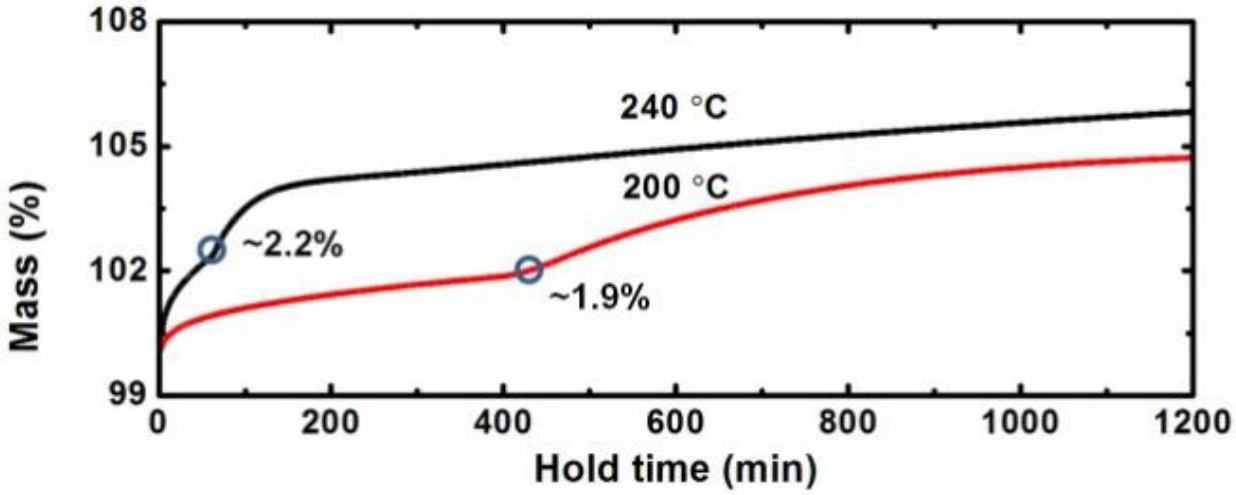

Figure 3.18. Thermogravimetric data of pristine $LiFeBO_3$ (micron-sized) collected isothermally under dry O_2 (25 mL/min) at 200 ℃ (red curve) or 240 ℃ (black curve). The rate of mass gain increases at ~2.0% mass gain during these two isothermal holds suggests a common structural transition associated with either delithiation or degradation. Figure is reproduced with permission from Ref 1.

The close similarity of the degraded and delithiated phase motivated an additional set of NMR experiments with the resolution to distinguish between the two phases using a newly-developed pj-MATPASS pulse sequence to gain information from both ^{7}Li and ^{11}B spectra, the latter which has not previously been utilized to study this compound. The purpose of this NMR study is to identify whether lithiation of Li_dFeBO_3 would produce $LiFeBO_3$. Electrodes of degraded $LiFeBO_3$ (100 ℃ in air for one week) were therefore prepared and studied by ^{7}Li and ^{11}B NMR both before cycling (OCV) and after lithiation induced by discharging to 1.5 V at a C/30 rate (based on an assumed 220 mAh/g capacity), with the results shown in Fig. 3.19. Using the pj-MATPASS pulse sequence, the isotropic spectrum can be reconstructed (black spectrum, top) from the individual NMR spectra in this 2D experiment (colored spectra in lower square) that individually probe the contributions from spinning sidebands of different orders, providing a sum projection after a shear transformation of the F_2 dimension.

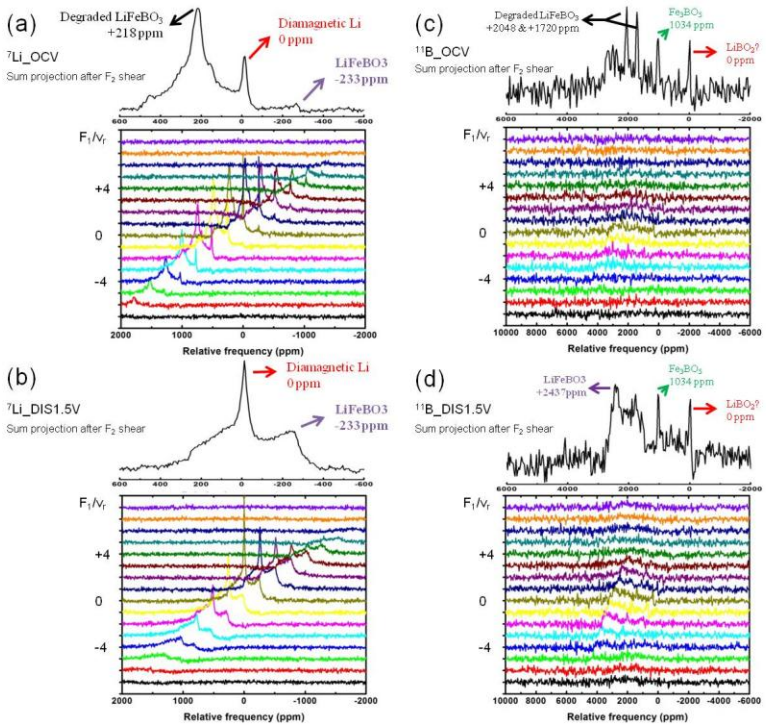

Figure 3.19. ^{7}Li NMR spectra of the highly degraded $LiFeBO_3$ electrodes (a) at OCV and (b) after discharge to 1.5 V collected by using a pj-MATPASS pulse sequence. ^{11}B NMR spectra of the highly degraded $LiFeBO_3$ electrodes (c) at OCV and (d) after discharge to 1.5 V collected by using a pj-MATPASS pulse sequence with a magnetic field of 11.7 T. Figure is reproduced with permission from Ref 1.

The ^{7}Li NMR spectrum of the original material (Fig. 3.19a) contains a degraded $LiFeBO_3$ resonance (+218 ppm), a diamagnetic Li resonance (0 ppm), a weak $LiFeBO_3$ resonance (-233 ppm), a broad resonance under the sharper +218 ppm resonance and several weaker peaks. The degradation reaction is almost complete as signified by the very weak $LiFeBO_3$ resonance. While the +218 ppm and 0 ppm resonances were assigned to degradation products, the appearance of several other resonances underscores the complexity of this degradation reaction. Note that broad

resonances are also observed during the (de)lithiation processes. Their appearance in the highly degraded $LiFeBO_3$ sample therefore suggests that this "degradation" reaction is in fact a combination of a delithiation and a degradation, producing phases such as $Li_{0.5}FeBO_3$ and $Li_{0.5-x}FeBO_3$, along with the degraded phase, Li_dFeBO_3.

Assignment of the ^{11}B NMR resonances was performed by comparing the spectra of a pristine $LiFeBO_3$ sample and partially degraded $LiFeBO_3$ sample, as shown in Fig. 3.20. Strong resonances associated with the degraded $LiFeBO_3$ phase were found at ~2048 and ~1720 ppm in the original material, while a weak resonance corresponding to $LiFeBO_3$ (a complex peak shape centered at ~2460 ppm) can also be discerned (Fig. 3.19c). A resonance at ~1034 ppm is tentatively assigned to Fe_3BO_5, a known minor impurity phase in these samples, but this has not been confirmed through studies on pure Fe_3BO_5.

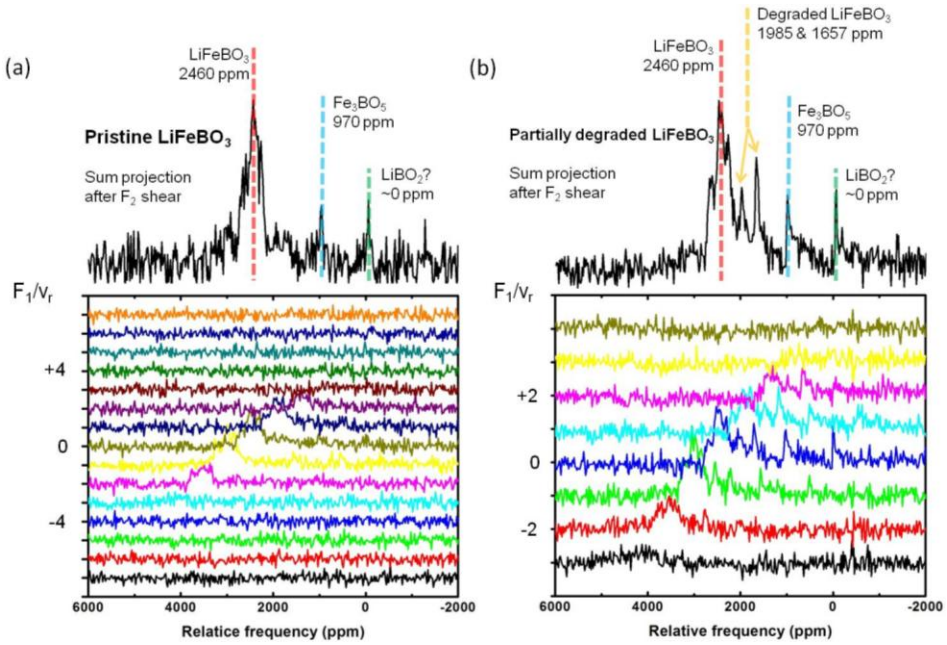

Figure 3.20. ^{11}B pj-MATPASS NMR spectra of pristine and partially degraded $LiFeBO_3$. Data were collected with a magic angle spinning speed of 50 kHz, and a magnetic field of 7.1 T. The pristine sample contains Fe_3BO_5 as suggested by XRD studies. Therefore, one resonance with a hyperfine shift of ~ 970 ppm was tentatively assigned to B in the Fe_3BO_5 lattice. The dominant ~2460 ppm resonance was assigned to $LiFeBO_3$, which also agrees well with our earlier DFT calculation of the hyperfine shift for $LiFeBO_3$. The ~ 0 ppm resonance corresponds to a boron-containing diamagnetic phase, which could be unreacted $LiBO_2$ precursor or other types of lithium borate that formed during the process of synthesizing $LiFeBO_3$. In contrast to the pristine $LiFeBO_3$, two other resonances appear in the degraded sample (~1985 and ~1657 ppm), which were therefore assigned to B in a degraded $LiFeBO_3$ lattice (Li_dFeBO_3). Figure is reproduced with permission from Ref 1.

After discharge to 1.5 V, the $LiFeBO_3$ ^{7}Li resonance (at approximately -233 ppm) and the ^{11}B resonance (at approximately 2460 ppm) grow in intensity, which we ascribe to the lithiation of $Li_{1-x}FeBO_3$ (Fig. 3.19b and Fig. 3.19d). The sharper, more distinct resonances assigned to degraded $LiFeBO_3$ (Li_dFeBO_3) resonance disappear in the ^{7}Li NMR spectrum, and are significantly broadened in the ^{11}B NMR spectrum. A new very broad resonance appears (with a center of gravity of about 0 ppm in the ^{7}Li NMR spectrum, and 1000 ppm in the ^{11}B NMR spectrum) which can be assigned to the lithiated form of the degraded $LiFeBO_3$. This demonstrates that, contrary to the reversible delithiation reactions of $LiFeBO_3$ (forming partially delithiated $Li_{1-x}FeBO_3$), the transformation of $LiFeBO_3$ to Li_dFeBO_3 is irreversible.

The multiphase nature of the degradation reaction is also evident in neutron diffraction studies. The neutron diffraction data (Fig. 3.21) from a degraded sample (200 ℃, 5-day treatment) could not be appropriately fit to a single monoclinic phase in Le Bail refinements, indicating the presence of an additional phase. Two-phase Le Bail refinements assuming the presence of both degraded (D-Li_dFeBO_3) and delithiated ($Li_{t-x}FeBO_3$) phases were successful in modeling the observed diffraction pattern with two separate lattices whose dimensions were both close to that of the pristine $LiFeBO_3$ monoclinic C2/c subcell. One phase (a = 5.1393(15) Å, b = 8.7654(22) Å; c = 10.1254(23) Å; β = 90.332(26)°; V = 456.12(20) $Å^3$), later identified in Rietveld refinements as the degraded phase, had a refined crystallite size which was two times larger than the other delithiated phase (*a* = 5.1333(18) Å; *b* = 8.8891(30) Å; *c* = 10.1633(21) Å; β = 90.351(19)°; V = 463.75(24) $Å^3$).

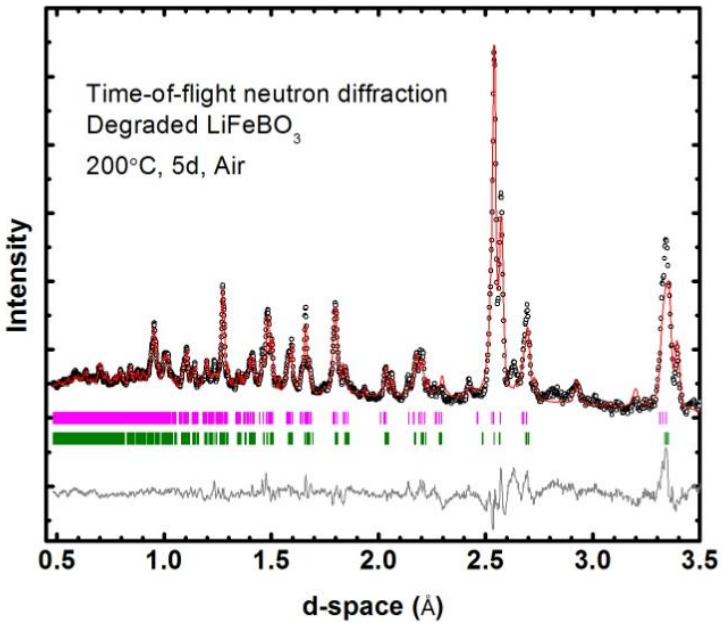

Figure 3.21. Rietveld refinements of degraded $LiFeBO_3$ by time-of-flight neutron diffraction (POWGEN). For clarity, only tick marks from the two main phases, degraded and delithiated $LiFeBO_3$, are shown in magenta and olive, respectively. Figure is reproduced with permission from Ref 1.

After identifying these two distinct phases, efforts were then made to explicitly model their diffraction peak intensities through Rietveld refinement. While the delithiated phase could be satisfactorily modeled by refining only the atomic positions of the non-Li atoms and the (reduced) site occupancies of the split Li sites, this was not the case for the degraded phase. The degraded phase modeled intensities only agreed with the experimental diffraction data when the occupancy of the Fe site was allowed reduced substantially below one, with a final refined site occupancy of 0.76(2). This indicates that the degradation process involves the displacement of Fe ions. This is fully consistent with the nature of the conditions that promote degradation (heating, oxidation in air). The smaller ionic radius and different coordination preferences of Fe^{3+}

relative to the Fe^{2+} in pristine $LiFeBO_3$ are expected to provide a thermodynamic driving force, while mild heating provides extra activation energy for iron ions to escape their potential wells. This degradation pathway may also likely to be accessible for other transition metal borates which are isostructural to $LiFeBO_3$, and perhaps may contribute to the source of the very poor electrochemical performance for both $LiMnBO_3$ and $LiCoBO_3$, although other factors such as poorer electronic conductivity and/or the presence of the Jahn-Teller ion Mn^{3+} on charging $LiMnBO_3$ may also play a role.

There are two possible final resting places for the Fe ions that are lost from the Fe site of $LiFeBO_3$ during the degradation process. One likely position is at vacant Li sites, while the other possibility is the loss of Fe from the $LiFeBO_3$ framework. The original Li site becomes accessible primarily due to Li loss during the degradation process forming diamagnetic species surrounding the parent $LiFeBO_3$ particles, although a small amount of Li/Fe anti-site disorder may also occur. When Fe was placed on the Li site in Rietveld refinements, the refined occupancy of this Fe site was 0.11(2), corresponding to only half of the ions lost from the majority site. Minimal differences in the quality of the refinement were found when this site was alternately tested to be fully vacant or to contain all of the Fe lost from the majority site. It is therefore not possible to discriminate between these two structural models (*i.e.*, disordering of Fe onto the Li site and Fe loss) from the present neutron diffraction data. The same model for Fe occupying the Li site was also tested against the neutron PDF data (Fig. 3.22), the refined distribution (0.56 Fe on the original Fe site and 0.11 Fe on the original Li site) was very similar to that obtained from Rietveld refinement of X-ray and neutron diffraction data. The Rietveld refinement results for degraded $LiFeBO_3$ are given in Tables 3.1-3. Structural information is also obtained for the delithiated phase that was also included in the refinement, though small fraction

of this phase (13 wt%) severely limits the accuracy of this refinement. Intriguingly, it was found that one of two split Li sites was fully occupied while the other was fully depopulated, providing both a putative stoichiometry($Li_{0.5}FeBO_3$) and rational for the two-phase end member of the delithiation of $LiFeBO_3$. Although this result must be considered tentative given the limitations of the diffraction data, it does provide a trial structure whose importance to the delithiation process can be tested by density functional theory calculations.

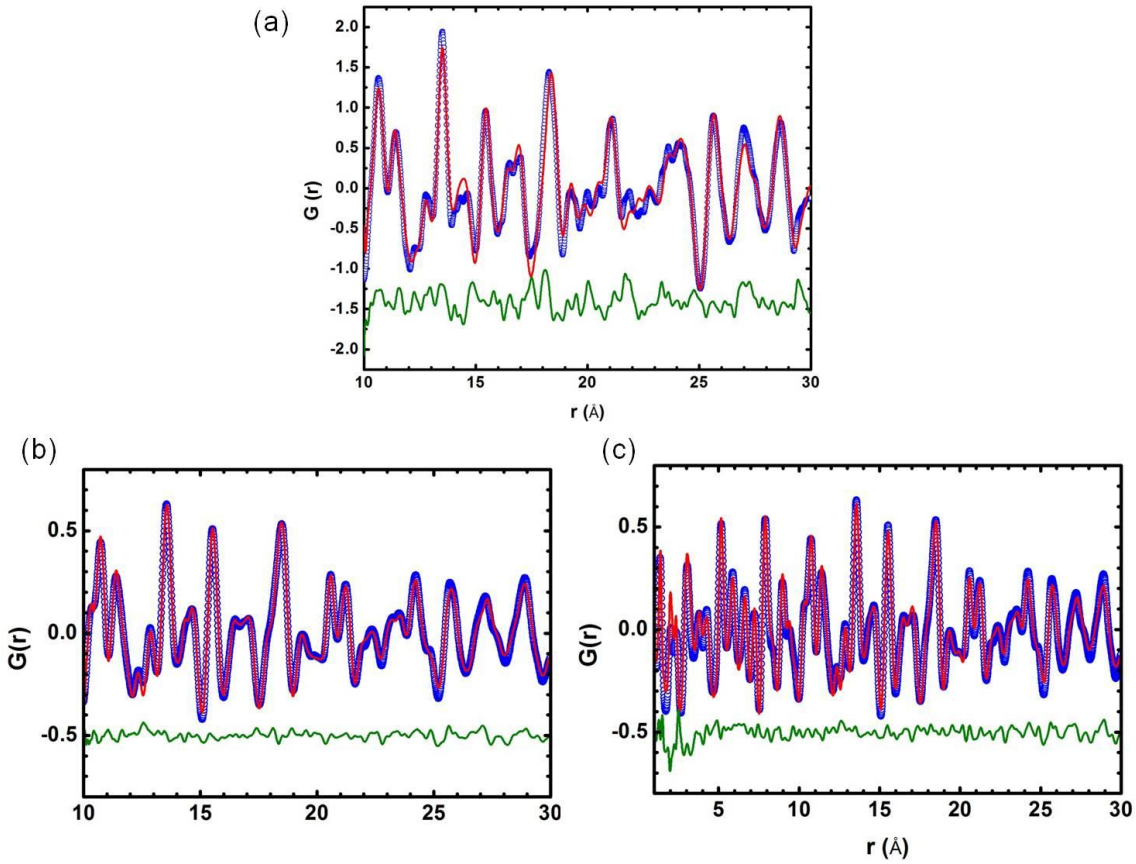

Figure 3.22. (a) Neutron PDF refinement (R_w = 0.23)of a highly degraded sample that was treated at 100 ℃ for 4 days. The observed data is shown in blue, the calculated pattern in red and the difference pattern in olive. Two phases (pristine $LiFeBO_3$ and degraded $LiFeBO_3$) were used in the refinement, with all the structural parameters of pristine $LiFeBO_3$ fixed to the values

refined using PDF data of an essentially single phase $LiFeBO_3$ sample (b), and with the structural parameters for the degraded phase allowed to freely vary during the refinement. The calculated ratio of Fe on the original Fe and Li sites is 56:11, which qualitatively agrees with the Bragg diffraction analysis. When the start of the fitting range for the degraded phase was lowered from 10 Å to 1 Å, the fitting quality was substantially degraded (R_w = 0.29). This is mostly likely due to the presence of inhomogeneity in the degraded structure, as well as other amorphous Li-rich components that may be produced external to the iron borate phase during the degradation process. It should be further noted that the fit quality is also poor at low distances (r < 5 Å) is in the PDF refinement (c) of the highly pure pristine $LiFeBO_3$ sample (R_w = 0.10 for 10-30 Å, and R_w = 0.17 for 1-30 Å), presumably because a simple average structure of $LiFeBO_3$ (50/50 split Li sites, one Fe site) was utilized rather than the fully modulated (or 4-dimensional) structure which has four different local coordination environments for every atomic site in the simpler average structure. Figure is reproduced with permission from Ref 1.

Table 3.1. Crystallographic data for the degraded $LiFeBO_3$ based on time-of-flight (TOF) neutron diffraction

Radiation	TOF neutron (POWGEN, SNS)
Crystal system	Monoclinic
Space group	*C2/c* (#15)
Lattice parameters	a=5.1390(15)Å, b=8.7650(22)Å, c=10.1240(23) (26) Å, β=90.341(26) °
Cell volume	456.01(21)$Å^3$
Density (calculated)	3.12518 g/cm^3
λ	0.7955 Å- 1.8655 Å
R_{wp}	2.640%
R_p	3.192%
χ^2	4.295

Table 3.2. Atomic coordinates and thermal parameters of the degraded $LiFeBO_3$ (TOF neutron)

Atom	Wyck.	*x/a*	*y/b*	*z/c*	Occ.	B_{iso} ($Å^2$)
Fe@Li site	8f	0.172(22)	-0.003(14)	0.134(14)	0.11(2)	2.65
Fe	8f	0.3588(20)	0.1657(16)	0.3698(16)	0.76(2)	1.1619
B	8f	0.16839(28)	0.32536(14)	0.12062(28)	1	0.5348
O1	8f	0.08376(30)	0.32852(91)	0.42332(69)	1	0.7690
O2	8f	0.26141(59)	0.18911(19)	0.16620(31)	1	0.7690
O3	8f	0.28441(52)	0.46489(18)	0.13167(65)	1	N/A*

* O3 has the largest modulation amplitude when describing $LiFeBO_3$ in the modulated structure with a superspace group of *C2/c* (α0γ)00 (α = 1/2 and γ = 0). When using the average structure (*C2/c*), the modulation of the O3 atom can be best described with anisotropic thermal parameters. This has been demonstrated in our prior single crystal work (Ref. 8 in the main text), and the anisotropic thermal parameters associated with this site in Rietveld refinements were fixed to the values (U_{11}= 0.0094, U_{22}= 0.00698, U_{33}= 0.0185, U_{12}= 0.00183, U_{13}= -0.00246, U_{23}= -0.00060) previously obtained from single crystal diffraction data.

Table 3.3. Selected bond distances (Å) for the degraded $LiFeBO_3$ (Li_dFeBO_3)

	TOF neutron, Li_dFeBO_3
Fe1 - O1*	2.03(12)
Fe1 - O2	1.77(12)
Fe1 - O3	2.01(11)
Fe1 - O3	2.40(14)
Fe2 - O1	2.082(14)
Fe2 - O1	2.114(17)
Fe2 - O2	1.998(11)
Fe2 - O2	2.128(16)
Fe2 - O3	1.908(14)
B - O1	1.3649(24)
B - O2	1.3656(26)
B - O3	1.3649(24)

* For clarity, Fe @ Li site is denoted as Fe1 and Fe at the original Fe site is denoted as Fe2.

Complementary information into the degradation process was obtained through high-resolution transmission electron microscopy (HRTEM) imaging of a single particle of the degraded phase (Fig. 3.23). The interior of a degraded $LiFeBO_3$ particle can be very effectively modeled (Box I) using the pristine $LiFeBO_3$ subcell in either a fully lithiated or partially delithiated state (the image contrast is weakly sensitive to the Li content). This is consistent with prior EELS studies, which find divalent iron at the center of particles but more highly oxidized iron at the particle exterior [7]. Even accounting for changes in sample thickness, the next shell out from the particle center (Box II) cannot be modeled with the same pristine structural model.

However, this area can be very effectively modeled by a degraded structure in which iron is fully disordered (50/50) over the Fe and Li sites. The smaller degree of disorder suggested by Rietveld refinement (76/24) is also ineffective in modeling this region, suggesting that when there is a sufficient driving force to push Fe onto a Li site, there will be full randomization locally. Finally, the thin (~2 nm) outermost shell of the particle has less bright/dark contrast than the region assigned to the degraded phase. The very symmetrical HRTEM pattern here can perhaps be better simulated using a mixture of the hexagonal lattice of α-Fe_2O_3 (hematite) and the degraded $LiFeBO_3$ structure, as shown in Fig. 3.24. The hexagonal structure of α-Fe_2O_3 has an in-plane lattice parameter of 5.04 Å, which is only 2% smaller than the pseudohexagonal lattice of pristine $LiFeBO_3$, and which almost perfectly matches the D-Li_dFeBO_3 lattice (5.07 Å in-plane for pseudohexagonal setting). It is possible that this outer layer contains Li, which has some solubility in α-Fe_2O_3 [19] [20] , though it is highly unlikely that borate groups are compatible with the close-packed oxygen framework of α-Fe_2O_3. The electrochemical behavior previously reported for α-Fe_2O_3 is not consistent with the voltage and capacities observed for $LiFeBO_3$ after degradation, further supporting the assignment of the 1.8 V electrochemical feature to the degraded $LiFeBO_3$ framework rather than a secondary phase of hematite.

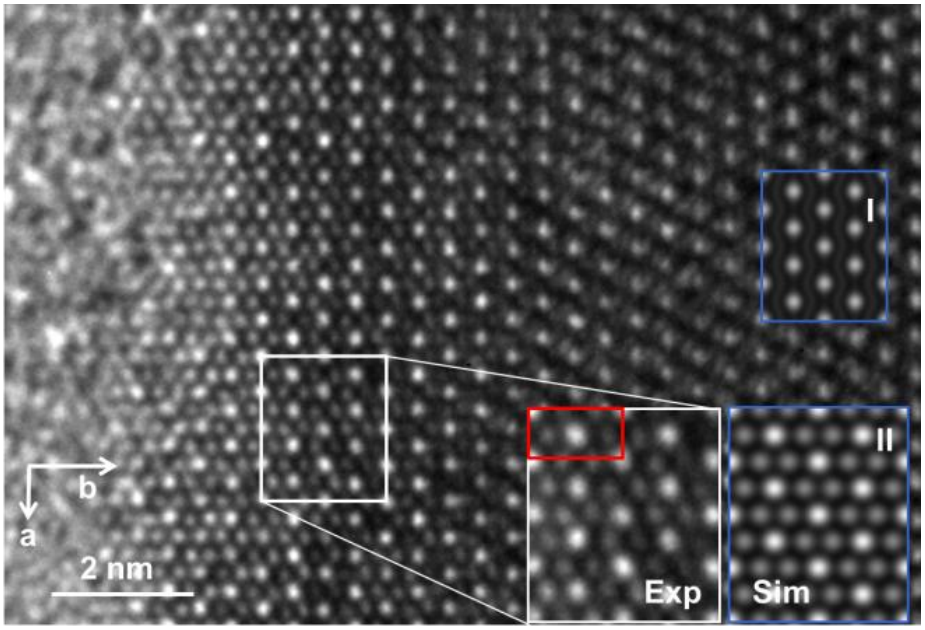

Figure 3.23. HRTEM) image of a degraded $LiFeBO_3$ particle viewed in the [001] zone axis. Simulations are shown for pristine (I) and degraded (II) $LiFeBO_3$, with a zoom of the image shown next to the latter including a red box marking the relationship of the $LiFeBO_3$ unit cell to the image. Data was collected and analyzed in collaboration with Dr. Lijun Wu, Dr. Lihua Zhang and Dr. Feng Wang from Brookhaven National Laboratory.Figure is reproduced with permission from Ref 1.

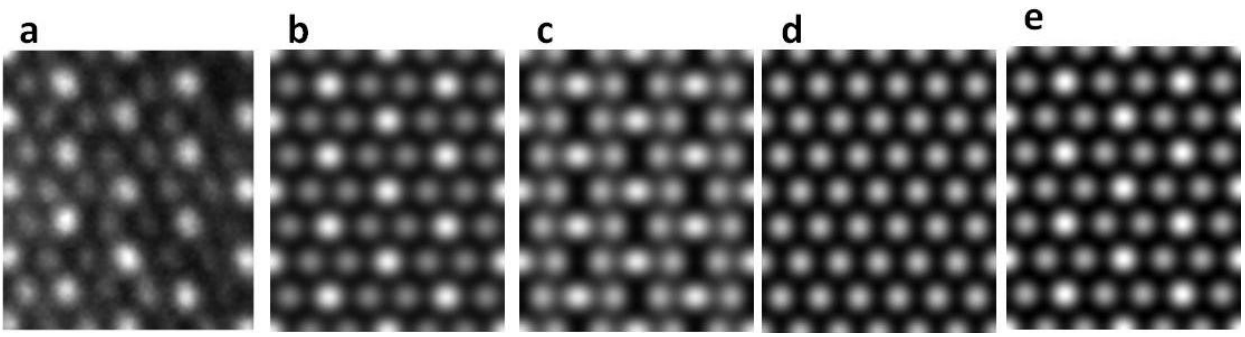

Figure 3.24. (a) HRTEM image from the degraded area. (b-d) Image simulation by multislice method with thickness=9.1 nm, defocus=-30 nm based on the same degraded structural model, but with varying degrees of Fe disordering onto the Li site: (b) 0.5 occupancy of Fe at Fe site, 0.5 Li / 0.5 Fe occupancy at Li site, (c) 0.75 occupancy of Fe at Fe site, 0.75 Li / 0.25 Fe occupancy at Li site and (d) α-Fe_2O_3 (hematite). (e) Image by adding (b) and (d). Data was collected and analyzed in collaboration with Dr. Lijun Wu, Dr. Lihua Zhang and Dr. Feng Wang from Brookhaven National Laboratory. Figure is reproduced with permission from Ref 1.

3.4 Conclusions

As summarized in Fig. 3.25, it is found that the delithiation of $LiFeBO_3$ proceeds reversibly through first a two-phase reaction between $LiFeBO_3$ and Li_tFeBO_3 (t ~ 0.5) at ~2.8 V *vs.* Li^+/Li and then through a solid solution between Li_tFeBO_3 and $Li_{t-x}FeBO_3$ ($0 < x < t$) at slightly higher potentials (2.8 – 3.2 V), though the full delithiation of $LiFeBO_3$ to form "$FeBO_3$" has not yet been experimentally demonstrated. For typical battery cells and normal cycling conditions, the solid-solution reaction begins well before the two-phase reaction is complete as a result of the large overpotentials commonly experienced. The degradation of $LiFeBO_3$ involves at least two separate processes that produce distinct degraded and delithiated phases, both of which share the same monoclinic framework as pristine $LiFeBO_3$. A key structural aspect of the

degraded phase is the loss of iron from its original trigonal bipyramidal crystallographic site. TEM studies support the conclusion that the missing iron has moved onto what was formerly a Li site, though the complete loss of iron from the degraded phase (in the form of -Fe_2O_3) cannot be definitively excluded. The degraded phase is oxidized relative to the pristine phase but still contains Li and can be reduced to contain only divalent iron when Li is intercalated at low voltages (< 1.8 V). This degradation pathway is also expected to be accessible for other transition metal borates such as $LiMnBO_3$ and $LiCoBO_3$, and could be responsible for the poor electrochemical performance of these phases if the degradation pathway of loss of transition metal from the bipyramidal site can occur at room temperature.

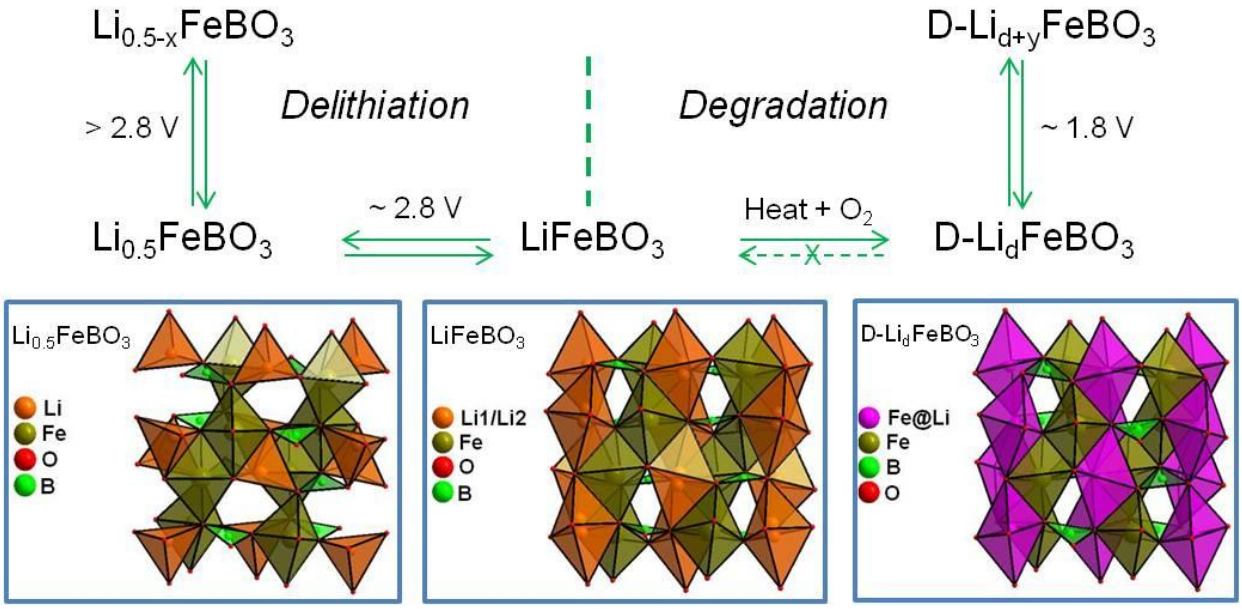

Figure 3.25. Summary of the structural transformation pathways of $LiFeBO_3$ during delithiation and degradation. Figure is reproduced with permission from Ref 1.

3.5 References

1. Bo, S. H.; Nam, K. W.; Borkiewicz, O. J.; Hu, Y. Y.; Yang, X. Q.; Chupas, P. J.; Chapman, K. W.; Wu, L. J.; Zhang, L. H.; Wang, F.; Grey, C. P.; Khalifah, P. G., Structures of delithiated and degraded $LiFeBO_3$, and their distinct changes upon electrochemical cycling. *Inorg Chem* **2014**.

2. Yamada, A.; Iwane, N.; Harada, Y.; Nishimura, S.; Koyama, Y.; Tanaka, I., Lithium Iron Borates as High-Capacity Battery Electrodes. *Adv. Mater.* **2010,** *22* (32), 3583-3587.

3. Barpanda, P.; Yamashita, Y.; Yamada, Y.; Yamada, A., High-Throughput Solution Combustion Synthesis of High-Capacity $LiFeBO_3$ Cathode. *J Electrochem Soc* **2013,** *160* (5), A3095-A3099.

4. Kim, J. C.; Moore, C. J.; Kang, B.; Hautier, G.; Jain, A.; Ceder, G., Synthesis and Electrochemical Properties of Monoclinic $LiMnBO_3$ as a Li Intercalation Material. *J Electrochem Soc* **2011,** *158* (3), A309-A315.

5. Yamada, A.; Iwane, N.; Nishimura, S.; Koyama, Y.; Tanaka, I., Synthesis and electrochemistry of monoclinic $Li(Mn_xFe_{1-x})BO_3$: a combined experimental and computational study. *Journal of Materials Chemistry* **2011,** *21* (29), 10690-10696.

6. (a) Legagneur, V.; An, Y.; Mosbah, A.; Portal, R.; La Salle, A. L.; Verbaere, A.; Guyomard, D.; Piffard, Y., $LiMBO_3$ (M = Mn, Fe, Co): synthesis, crystal structure and lithium deinsertion/insertion properties. *Solid State Ionics* **2001,** *139* (1-2), 37-46; (b) Dong, Y. Z.; Zhao,

Y. M.; Shi, Z. D.; An, X. N.; Fu, P.; Chen, L., The structure and electrochemical performance of $LiFeBO_3$ as a novel Li-battery cathode material. *Electrochimica Acta* **2008,** *53* (5), 2339-2345.

7. Bo, S. H.; Wang, F.; Janssen, Y.; Zeng, D. L.; Nam, K. W.; Xu, W. Q.; Du, L. S.; Graetz, J.; Yang, X. Q.; Zhu, Y. M.; Parise, J. B.; Grey, C. P.; Khalifah, P. G., Degradation and (de)lithiation processes in the high capacity battery material $LiFeBO_3$. *Journal of Materials Chemistry* **2012,** *22* (18), 8799-8809.

8. Janssen, Y.; Middlemiss, D. S.; Bo, S. H.; Grey, C. P.; Khalifah, P. G., Structural Modulation in the High Capacity Battery Cathode Material $LiFeBO_3$. *J. Am. Chem. Soc.* **2012,** *134* (30), 12516-12527.

9. Seo, D. H.; Park, Y. U.; Kim, S. W.; Park, I.; Shakoor, R. A.; Kang, K., First-principles study on lithium metal borate cathodes for lithium rechargeable batteries. *Physical Review B* **2011,** *83* (20).

10. Grey, C. P.; Dupre, N., NMR studies of cathode materials for lithium-ion rechargeable batteries. *Chem Rev* **2004,** *104* (10), 4493-4512.

11. Ravel, B.; Newville, M., ATHENA, ARTEMIS, HEPHAESTUS: data analysis for X-ray absorption spectroscopy using IFEFFIT. *Journal of Synchrotron Radiation* **2005,** *12*, 537-541.

12. Borkiewicz, O. J.; Shyam, B.; Wiaderek, K. M.; Kurtz, C.; Chupas, P. J.; Chapman, K. W., The AMPIX electrochemical cell: a versatile apparatus for in situ X-ray scattering and spectroscopic measurements. *J Appl Crystallogr* **2012,** *45*, 1261-1269.

13. Neuefeind, J.; Feygenson, M.; Carruth, J.; Hoffmann, R.; Chipley, K. K., The Nanoscale Ordered MAterials Diffractometer NOMAD at the Spallation Neutron Source SNS. *Nucl Instrum Meth B* **2012,** *287*, 68-75.

14. Hung, I.; Zhou, L. N.; Pourpoint, F.; Grey, C. P.; Gan, Z. H., Isotropic High Field NMR Spectra of Li-Ion Battery Materials with Anisotropy > 1 MHz. *J Am Chem Soc* **2012,** *134* (4), 1898-1901.

15. Kirkland, E. J., Advanced Computing in Electron Microscopy, Plenum, New York, 1998.

16. Le Toquin, R.; Paulus, W.; Cousson, A.; Prestipino, C.; Lamberti, C., Time-resolved in situ studies of oxygen intercalation into $SrCoO_{2.5}$, performed by neutron diffraction and X-ray absorption spectroscopy. *J. Am. Chem. Soc.* **2006,** *128* (40), 13161-13174.

17. David, W. I. F., Robust Rietveld refinement in the presence of impurity phases. *J Appl Crystallogr* **2001,** *34*, 691-698.

18. Stone, K. H.; Lapidus, S. H.; Stephens, P. W., Implementation and use of robust refinement in powder diffraction in the presence of impurities. *J Appl Crystallogr* **2009,** *42*, 385-391.

19. Larcher, D.; Bonnin, D.; Cortes, R.; Rivals, I.; Personnaz, L.; Tarascon, J. M., Combined XRD, EXAFS, and Mossbauer studies of the reduction by lithium of alpha-Fe_2O_3 with various particle sizes. *J Electrochem Soc* **2003,** *150* (12), A1643-A1650.

20. Larcher, D.; Masquelier, C.; Bonnin, D.; Chabre, Y.; Masson, V.; Leriche, J. B.; Tarascon, J. M., Effect of particle size on lithium intercalation into alpha-Fe_2O_3. *J Electrochem Soc* **2003,** *150* (1), A133-A139.

Chapter 4

Thin film and bulk investigations of $LiCoBO_3$ as a Li-ion battery cathode [1]

4.1 Introduction

Li*M*BO_3 (*M* = Mn, Fe, Co) cathode materials have generated recent excitement in the battery community due to their high theoretical specific capacities (~220 mAh/g) relative to the very extensively studied olivine $LiFePO_4$ system (170 mAh/g)[2, 3]. Among Li*M*BO_3 compounds, the best performance thus far has been achieved for $LiFeBO_3$, a compound for which multiple groups have demonstrated half-cell batteries in which more than 75% of the theoretical capacity can be achieved reversibly [5-8]. However, the rate performance of this system lags behind that of most commercialized systems and the overall $LiFeBO_3$ energy density is limited by the relatively low potential associated with the Fe^{3+}/Fe^{2+} redox couple (~2.8 V *vs.* Li+/Li) and has yet to show improvement beyond that achieved for $LiFePO_4$. Furthermore, this system is known to rapidly degrade on exposure to air [4, 5], in a process which has recently been demonstrated to involve disorder between the Li and Fe sites [6].

Density functional theory calculations predict that substantially higher voltages can be achieved for $LiMnBO_3$ (3.6-3.7 V) and $LiCoBO_3$ (4.0-4.1 V) than for $LiFeBO_3$ [8, 10-11]. Experimental studies on $LiMnBO_3$ to date have only resulted in about half of the $LiMnBO_3$ theoretical capacity being realized, and show a very large degree of polarization (> 1 V) which has prevented the accurate experimental assessment of the redox potential associated with this phase. It has been suggested that Mn dissolution at higher states of charge may be a factor limiting the realization of the theoretical capacity of $LiMnBO_3$, as it has been observed that

$LiMnBO_3$ exposed to NO_2BF_4 experiences a complete loss of crystallinity [7]. Relative to pure $LiFeBO_3$, solid solutions of $LiMnBO_3$ with $LiFeBO_3$ require higher potentials to charge and display higher OCV voltages but unfortunately do not produce any substantial improvements in discharge voltages, which occur almost entirely below 3 V [7]. It has proven even more difficult to reversibly cycle $LiCoBO_3$ than $LiMnBO_3$. The best reported discharge capacities of about 30 mAh/g were observed for nanoscale preparations (primary particle size of 50-100 nm, though with a substantially larger secondary particle size), and the rate of Co dissolution at oxidizing potentials was high enough to observe the deposition of Co metal on the Li anode in half-cell experiments [8].

Smaller particle sizes are expected to lead to improved performance for $LiCoBO_3$ due to (1) smaller Li diffusion lengths and (2) a reduction in the overpotential needed for charging due to the shorter electron transport distances. Physical vapor deposition processes offer the ability to precisely control film thickness, and can allow the performance of $LiCoBO_3$ to be evaluated at shorter length scales than was previously possible. Films of $LiCoBO_3$ were therefore prepared by reactive magnetron sputter deposition techniques, and their electrochemical and electronic properties were studied to investigate whether the present performance limitations of the $LiCoBO_3$ system can be overcome in batteries incorporating uniformly small grain sizes of $LiCoBO_3$. Detailed characterization of the bulk and local structure of $LiCoBO_3$ were carried out in tandem with impedance spectroscopy measurements to explore whether the major factors limiting reversible capacity were structural (anti-site defects) or kinetic (poor Li-ion or electronic conductivity) in nature. Finally, optical studies on powders and thin-film samples provided an opportunity to compare experimental results with prior DFT predictions, especially since the latter are not always well-behaved for 3d transition metal systems.

4.2 Experimental

Synthesis of $LiCoBO_3$ powder: $LiCoBO_3$ powder syntheses were tested under a variety of conditions, including different combinations of starting materials ($LiBO_2$ + CoO, $LiBO_2$ + Co_3O_4, addition of 10% citric acid to preceding mixtures), reaction temperatures (600, 700, and 800 ℃), reaction time (12, 20, 22, and 25 hours), crucible types (alumina, quartz and graphite), and atmospheres providing different oxygen chemical potentials (air, N_2, Ar, and forming gas of 5% H_2 / 95% N_2). Typically, stoichiometric amounts of precursors sufficient to prepare 5 g of product were weighed and then milled in a stainless steel high-energy ball mill jar for at least 30 minutes (SPEX SamplePrep8000 Mixer/Mill). The optimal procedure for producing $LiCoBO_3$ was found to consist of the reaction of $LiBO_2$ and CoO at 600 ^oC for 20 hours under N_2 in graphite crucibles. More reducing conditions (*i.e.*, the addition of 10% citric acid in the starting material or the use of 5% H_2 / 95% N_2 atmosphere) favored the reduction of ionic Co to Co metal, preventing the formation of $LiCoBO_3$.

Thin film preparation: Al_2O_3 substrates of 1 cm diameter and 380 μm thickness (99.6%, Valley Design) were coated on both sides with 0.5 μm Pt using direct current (DC) magnetron sputtering to form the cathode current collector. $LiCoBO_3$ thin films were deposited onto the Pt-coated Al_2O_3 substrates by radio frequency (RF) magnetron sputtering using a homemade $LiCoBO_3$ target (general methods can be found elsewhere) [9, 10] . The target was prepared by pressing enough powder to form a 2” diameter disk (1/8” thick). This pellet was fired for 3 h at 700 ℃ under argon gas and bonded to a Cu plate. RF sputtering was carried inside a chamber with a base pressure of 10^{-6} Torr, using an Ar plasma operated at 80 W power and 20 mTorr pressure. A quartz microbalance was used before and after the deposition to measure the amount of mass deposited by unit of time. After deposition, the as-produced thin films were post-

annealed in flowing argon at 600 °C for 1 hour in a tube furnace. After preparation, the samples were stored under an Ar atmosphere (typically inside an Ar-filled glovebox) until used for measurements. For impedance measurements, a second 1 mm thick Pt electrode was deposited (DC magnetron sputtering) on the annealed thin film sample to provide the second electrical contact.

XRD: X-ray diffraction (XRD) patterns of powder samples were collected on a Bruker D8 Advance laboratory diffractometer (Cu K_α), equipped with a 192-channel Lynx-Eye linear strip detector. For the collection of Rietveld refinement quality data, a fixed divergence slit of 0.3 ° was used in place of the normal variable slits, and a deeper zero-background Si holder with a well depth of 0.3 mm (rather than the typical 0.05 mm) was utilized to minimize preferred orientations of the crystallites. The Rietveld refinement was carried out using the TOPAS v4.2 software package. Distance restraints for the BO_3 group were implemented so that chemically reasonable bond lengths (B-O bond distances of 1.37 ± 0.02 Å) would be maintained in the refined structural models. The displacement parameters of $LiCoBO_3$ were fixed to the values experimentally determined for $LiFeBO_3$ from the refinement of higher-resolution time-of-flight neutron diffraction data for a highly pure $^{7}LiFe^{11}BO_3$ pristine sample [6], since they essentially share the same framework and the laboratory X-ray diffraction data used in the present study did not permit the accurate determination of displacement parameters for light atoms. Powder XRD measurements on thin film electrodes were performed using a Scintag Pad V X-ray Diffractomer with a Cu K_α source and a thin Ni filter.

Scanning Electron Microscopy (SEM): SEM images were collected on a JEOL 7600F high-resolution microscope. The as-prepared $LiCoBO_3$ powder was attached onto a 12.5 mm graphite mount (Ted Pella, Inc.) using a diluted colloidal graphite water solution (Ted Pella, Inc.).

Compositional Analysis: Li:Co molar ratios of thin films were determined using a Thermo Jarrell Ash IRIS inductively coupled plasma-optical emission spectrometer (ICP-OES). 2 mL of freshly prepared aqua regia (3:1 mixture of hydrochloric acid and nitric acid) were used to dissolve the films for analysis followed by dilution in 18.3 M deionized water. A series of ICP standards were prepared by the serial dilution of standards purchased from Alfa Aesar.

TGA: Thermogravimetric analysis (TGA) studies were carried out on a Q5000IR system (TA instruments). TGA scans were run under flowing O_2 (25 mL/min) with a heating rate of 0.25 ℃/min on heating and an isothermal hold at 650 ℃ for 1 h, before cooling down and stabilizing the system at room temperature, allowing the net mass change to be determined without correcting for buoyancy.

Diffuse reflectance: Higher energy diffuse reflectance data was collected on a Perkin-Elmer Lambda 950 UV-VIS spectrometer incorporating a 60 mm diameter Spectralon integrating sphere over a wavelength range of 200 nm – 860 nm. Samples were packed to a depth of ~10 mm in a black cup with a thin quartz window (1.50 mm thick) mounted vertically in the instrument, and intensities were referenced to a $BaSO_4$ standard (Alfa Aesar, 99.998%). Lower energy bidirectional reflectance data were collected using a custom bidirectional reflection spectrometer with an ASD detector system capable of analyzing data collected over the

wavelength range of 350 – 2500nm. The RS^3 spectral acquisition software from ASD Inc. was used for reflectance data collection. Powder samples were filled to a depth of 1 – 2 mm in a flat black dish. The incident beam and detector were oriented at angles of 0 and 30 degrees, respectively, relative to the vertical normal vector of the dish. Light was collected over a relatively small angular range using an optical lens with a circular opening corresponding to a 7 ° aperture. Absorbances were estimated using the Kubleka-Munk transform, $\alpha_{KM} / s = (1-R)^2 / 2R$, where R is the measured diffuse reflectance and *s* is an unknown sample scattering coefficient, which is sample-preparation dependent and strongly depends on particle size. Direct gaps were fit to the functional form: $\alpha(E) = A(E - E_g)^2/E$, where the E in the denominator accounts for the typical variation in semiconductor optical coefficients near the gap. The Urbach tail region was fit using the functional form: $\alpha = Ae^{-(E-E_g)/E_U}$, where E_g an approximate gap and E_U is a characteristic Urbach energy that describes the breadth of the transition.

NMR: For ^{7}Li magic angle spinning (MAS) NMR measurements, a 1.3 mm HX probe (Samoson) was utilized in a wide-bore Oxford 500 MHz (11.7 T) Varian Infinity Plus spectrometer. A rotor-synchronized spin echo sequence (π/2-τ-π-τ-acquisition) was utilized with a spinning speed of 50 kHz. The Larmor frequency of ^{7}Li is 194.24 MHz. A pulse width of 1.6 μs (π/2) and a recycle delay of 100 ms were used. 1 M LiCl was used as an external chemical shift reference (0 ppm). To better separate the manifold of spinning sidebands, a recently developed pulse sequence, projection-magic angle turning phase adjusted spinning sidebands (pj-MATPASS) was also employed. The pj-MATPASS pulse sequence was adopted from previous work [11] and the starting t_1 was set to be 2/3 of a rotor period to minimize pulse ring-down effects before detection. The π/2 projection pulse was 1.6 μs.

Electrochemistry: Electrochemical characterization was conducted at 25°C inside a thermostatic incubator using 2-electrode coin cells (2032 hardware, 316L, Hohsen) prepared inside an Ar-filled glovebox. The cells consisted of a pure Li (Alfa Aesar) counter electrode, 1.2 M $LiPF_6$ in dimethyl carbonate (DMC) and ethylene carbonate (EC) (Novolyte) as the electrolyte, Celgard 2500 separators, and the thin film as the working electrode. Galvanostatic cycling was performed on a Maccor 4000 Series from 2.5 to 4.5 V. Impedance measurements were performed using a Solartron 1400 CellTest system (0.1 Hz – 1 MHz). Cyclic voltammetry measurements were performed using a Biologic VSP potentiostat scanned at a rate of 5 mV/s. The current density was converted into a C rate based on the $LiCoBO_3$ theoretical capacity of 215 mAh/g.

4.3 Results and discussion

4.3.1 Synthesis and structural studies

A first step toward the goal of producing and characterizing $LiCoBO_3$ thin films was the development of a bulk synthesis procedure for producing large amounts of $LiCoBO_3$ powders which can be pressed into a target for a reactive magnetron sputter deposition film growth. Although a variety of synthesis procedures for producing nanoscale $LiFeBO_3$ have been previously developed which utilize carbon to help inhibit grain growth and sintering[4-5, 12], these synthesis methods cannot in general be directly applied to the production of $LiCoBO_3$. The best method for the synthesis of bulk $LiCoBO_3$ in the present study was found to be the reaction of $LiBO_2$ and CoO precursors at 600 ℃ under inert gas (flowing N_2 or Ar), which readily produced nearly single phase $LiCoBO_3$, but often with a slight amount of a Co_3O_4 impurity phase (Fig.

4.1). The addition of citric acid as a precursor resulted in the observation of $LiBO_2$ and Co metal (mixture of hexagonal and cubic close packed polytypes) as reaction products, and the same overly reduced products were observed when citrate-free precursors were used under more strongly reducing conditions (5% H_2 / 95% N_2 gas at 600 ℃), as shown in Figure 4.2.

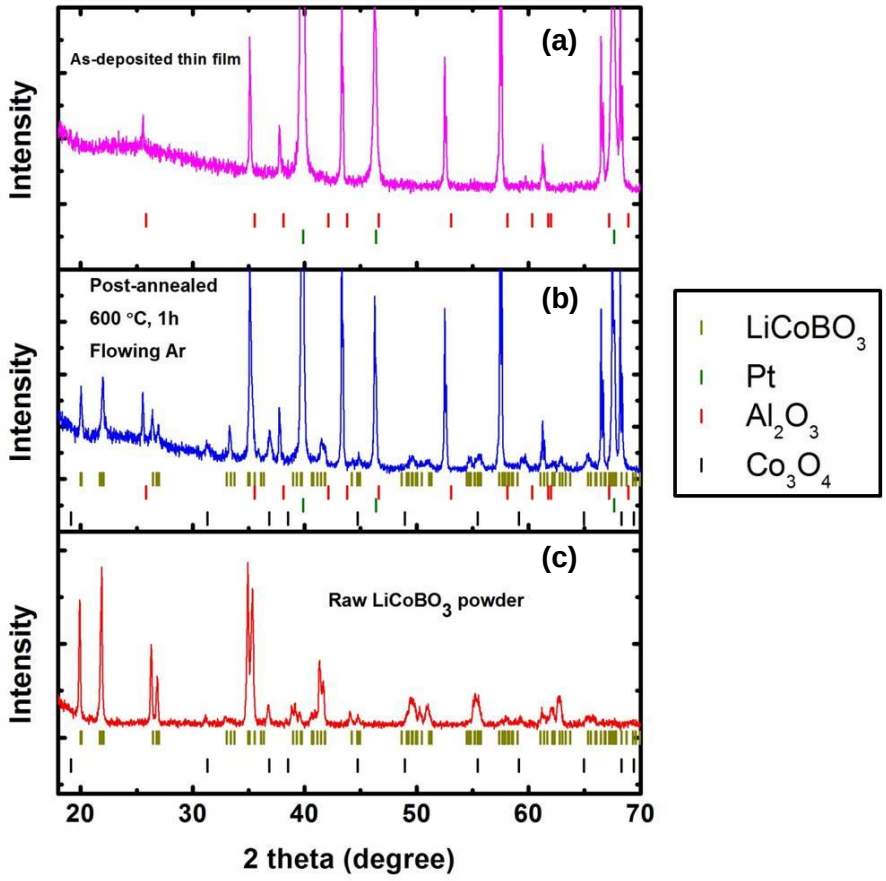

Figure 4.1. XRD patterns of (a) as-deposited film on Pt-coated Al_2O_3 substrates exhibiting no peaks other than those associated with the substrate, (b) post-annealed films (600 °C, 1 hr), exhibiting the expected $LiCoBO_3$ diffraction peaks, and (c) powder $LiCoBO_3$ prepared from reacting $LiBO_2$ and CoO under N_2 at 600 °C. Data was collected and analyzed in collaboration

with Dr. Gabriel Veith from Oak Ridge National Lab. Figure is reproduced with permission from Ref 1.

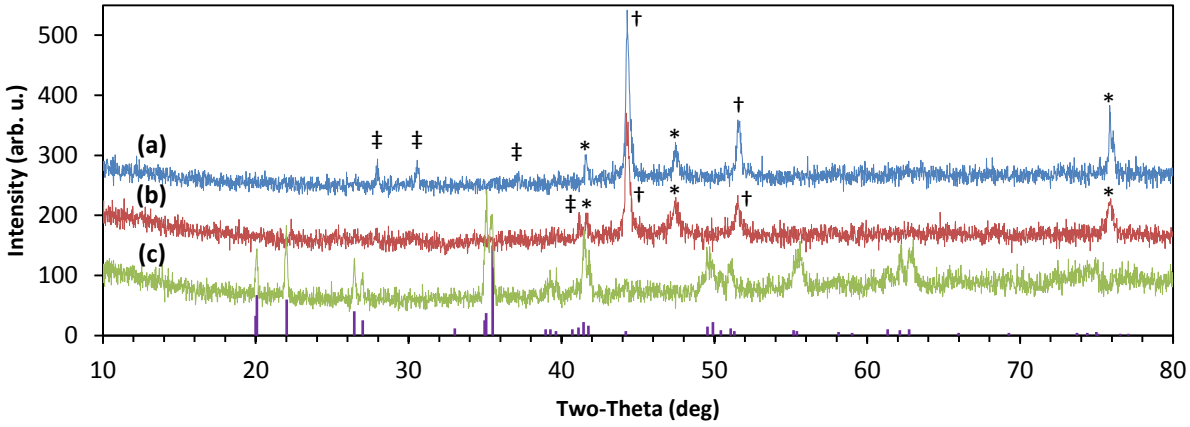

Figure 4.2. XRD patterns of syntheses of nominal $LiCoBO_3$ using (a) $LiBO_2$ + CoO + 10% citric acid in N_2 at 600 ^oC, (b) $LiBO_2$ + CoO in 5% H_2 / 95% N_2 at 600 ^oC, and (c) $LiBO_2$ + CoO in N_2 at 600 ^oC. Pure $LiCoBO_3$ phase is shown in purple overlay. Impurity phases of (*) hcp Co, (†) ccp Co, and (‡) $LiBO_2$ are marked. Data was collected and analyzed in collaboration with Mr. Micheal Saccomanno from Stony Brook University. Figure is reproduced with permission from Ref 1.

It should be noted that more reducing conditions were successfully utilized in the recently developed synthesis of Yamashita *et al.* for producing nanoparticles of $LiCoBO_3$ [8], a method which utilized a $Co_2B_2O_5$ precursor containing divalent Co and included a conductive carbon additive rather than complex carbohydrates (sugar, citrate, *etc.*). This alternative method produced CoO rather than Co_3O_4 impurities at the optimal temperatures of 400 – 450 ℃, and

gave Co metal as a major reaction product at temperatures as low as 500 ℃. However, particle size reduction was not an important goal of the present synthesis, and the approximate particle size of <10 microns observed in SEM studies (Figure 4.3) was sufficiently small to allow the powders to be pressed into dense pellets that could serve as targets for the production of films by sputter deposition.

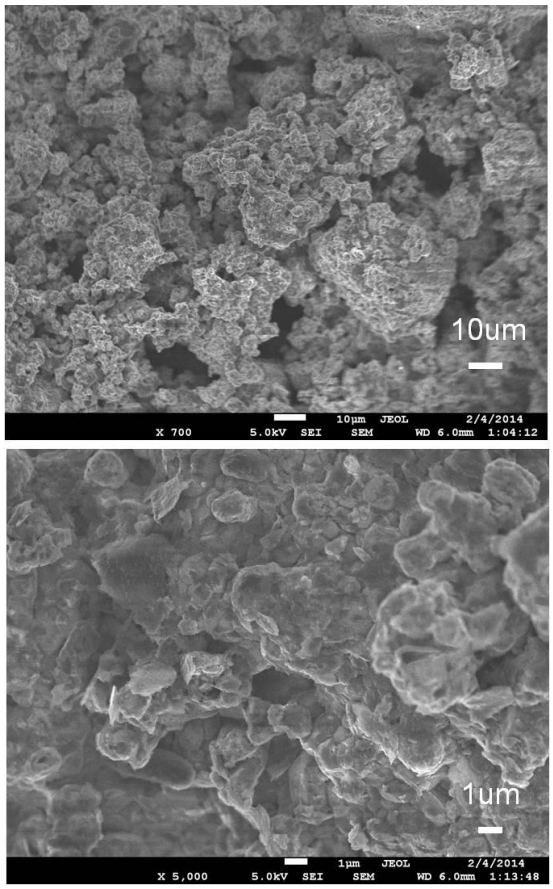

Figure 4.3. SEM images of $LiCoBO_3$ powder prepared from reacting $LiBO_2$ and CoO under N_2 at 600 °C. Particles form a dense agglomerate with a primary particle size smaller than 10 microns. Figure is reproduced with permission from Ref 1.

Bulk powders (~25 g) of $LiCoBO_3$ prepared in the optimal manner were cold pressed into a 2" diameter pellet, sintered, and then bonded to a copper plate to serve as a stoichiometric single-phase target for RF magnetron sputtering. Films were deposited either directly onto a sapphire substrate or onto a sapphire-supported underlayer of electronically conductive Pt film prepared by DC magnetron sputtering. The $LiCoBO_3$ deposition rate was calibrated using a quartz microbalance and Referenced to the total mass of a reference sample obtained by ICP analysis, allowing the actual mass loading (mg/cm^2) and nominal thickness (assuming 100% density) of subsequent films to be calculated. Although the thinnest films (as low as 15 nm nominal thickness) were the most desirable for electrochemical studies, thicker films were also prepared under similar conditions to determine which phases were present in the as-deposited films and in films treated by post-annealing. As seen in Figure 4.1, the as-deposited nominal $LiCoBO_3$ films only exhibited diffraction peaks associated with the Al_2O_3 substrate and the Pt underlayer, suggesting the absence of the desired crystalline $LiCoBO_3$ phase. However, post-annealing films in Ar at 600 ℃ for 1 hour resulted in the production of crystalline $LiCoBO_3$, together with a small impurity phase of Co_3O_4 and one weak additional un-indexed diffraction peak, potentially associated with Li_2O. ICP compositional analysis (averaged over three films prepared at different times over a 3 month span) found that the Li:Co ratio was 1.09:1 with an esd of 0.05, suggesting that the films may have a slight excess of Li. Lithium enrichment is known to occur during the deposition of some Li-ion battery materials due to differences in sputtering rates of the Li and transition metal[9].

In order to study the structure of bulk $LiCoBO_3$, Rietveld refinements were carried out using long powder diffraction scans collected on a laboratory diffractometer (d_{min} ~ 0.9 Å). It has been recently shown that both the delithiation and the degradation of $LiFeBO_3$ results in

structural variants of $LiFeBO_3$ which can be indexed to a monoclinic lattice that is nearly indistinguishable from that of the stoichiometric pristine phase [6]. As seen in Figure 4.4, the structure of $LiCoBO_3$ can be very well fit by Rietveld refinements using the simplified average structure of pristine $LiFeBO_3$ (two half-occupied Li sites of non-ideal tetrahedral symmetry, one single unsplit transition metal site which is a nearly ideal trigonal bipyramid, shown in inset) derived from the more complex modulated superstructure of $LiFeBO_3$ [13]. The refined lattice parameters in space group *C2/c* (#15) are: a = 5.1319(3) Å, b = 8.8495(6) Å, c = 10.1404(5) Å, and β = 91.281(3)°, with the full results of the Rietveld refinement and relevant structural parameters provided in Tables 5.1-4.3. There was no evidence of the anti-site disorder between the Li and transition metal sites that was found to be the key characteristic of degraded $LiFeBO_3$, though higher resolution data (such as synchrotron X-ray or time-of-flight neutron diffraction) could much more definitively rule out alternative structural models such as this one. It is not surprising that $LiCoBO_3$ does not degrade upon air exposure since $LiFeBO_3$ degradation was found to be an oxidative process which may readily occur for compounds like $LiFeBO_3$ which have modest voltages (~2.8 V), but is not expected to occur for high voltage compounds like $LiCoBO_3$ whose raised potentials preclude significant oxidation by the molecular species present in air (O_2, H_2O, *etc.*).

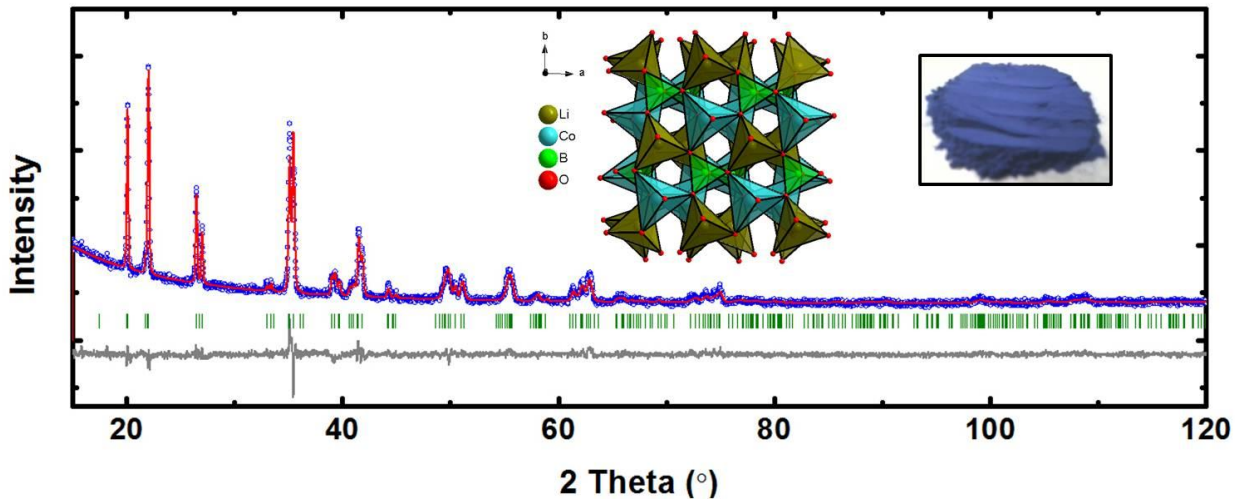

Figure 4.4. Rietveld refinement of laboratory XRD pattern from powder $LiCoBO_3$ sample. Inset: $LiCoBO_3$ crystal structure (viewed along [001] direction to emphasize the pseudo-trigonal nature of the framework) and a picture of the intense blue color of powders. Figure is reproduced with permission from Ref 1.

Table 4.1. Crystallographic data for $LiCoBO_3$. Table is reproduced with permission from Ref 1.

Radiation	Cu K_α
Crystal system	Monoclinic
Space group	*C2/c* (#15)
Lattice parameters	a = 5.1319(3)Å, b = 8.8495(6)Å,
	c = 10.1404(5) (26) Å, = 90.281(4) °
Cell volume	460.41(5) $Å^3$
Density (calculated)	3.66197 g/cm^3
λ	1.54 Å
R_{wp}	4.135%
R_{bragg}	2.803%
χ^2	1.289

Table 4.2. Atomic coordinates and thermal parameters of $LiCoBO_3$. Table is reproduced with permission from Ref 1.

Atom	Wyck.	*x/a*	*y/b*	*z/c*	Occ.	B_{iso} ($Å^2$)
Li1	8f	0.163	0.005	0.157	0.50	0.8679
Li2	8f	0.161	0.003	0.588	0.50	2.5721
Co	8f	0.1583(7)	0.3348(4)	0.1230(4)	1	1.1619
B	8f	0.351 (1)	0.1655(9)	0.354(1)	1	0.5348
O1	8f	0.225 (1)	0.3027(6)	0.342(1)	1	0.7690
O2	8f	0.409(1)	0.163 (1)	0.0836(9)	1	0.7690
O3	8f	0.182(1)	0.0438(4)	0.370(1)	1	anisotropic*

* Anisotropic thermal parameters associated with this O3 site in Rietveld refinements were fixed to the values:

U_{11} = 0.0094, U_{22} = 0.00698, U_{33} = 0.0185, U_{12} = 0.00183, U_{13} = -0.00246, U_{23} = -0.00060.

Table 4.3. Selected bond distances (Å) for $LiCoBO_3$. Table is reproduced with permission from Ref 1.

Li1 - O1	1.817(7)
Li1 - O2	1.881(5)
Li1 - O3	2.034(9)
Li1 - O1	2.19(1)
Li2 - O1	1.867(7)
Li2 - O3	1.943(9)
Li2 - O2	1.944(6)
Li2 - O1	2.25(1)
Co - O1	2.024(7)
Co - O2	2.025(8)
Co - O3	2.04(1)
Co - O3	2.116(9)
Co - O2	2.26(1)
B - O3	1.372(9)
B - O2	1.379(9)
B - O1	1.39(1)

The stability of $LiCoBO_3$ against oxidation was directly probed in TGA studies (Figure 4.5). When heated under dry flowing O_2, the onset of oxidation is found to occur at 460 ℃, suggesting that $LiCoBO_3$ is very resistant to oxidation as might be expected from the high voltage calculated for this compound. The mass gain appears to occur through two processes

rather than one, and the sample mass reaches a maximum around 575 ℃, before slightly decreasing on further heating to the maximum program temperature of 650 ℃. XRD analysis shows a spinel phase with the lattice parameters expected for Co_3O_4 as the only crystalline product after heating. The net mass change after oxidation is +4.23%, a result that is very consistent with the calculated mass change of +4.30% for the oxidation of Co^{2+} to the higher valence of $Co^{2.67+}$ expected for Co_3O_4 ($LiCoBO_3$ + 1/6 O_2 → 1/3 Co_3O_4 + $LiBO_2$). Taken together, these results suggest that $LiCoBO_3$ is very stable until it is thermally oxidized, at which point it rapidly decomposes to a spinel structure. These results suggest that oxidized $LiCoBO_3$ (*i.e.*, Li_xCoBO_3) is not thermodynamically stable at elevated temperature, in contrast to the $LiFeBO_3$ system, where Li_xFeBO_3 intermediate compositions are accessible upon heating.

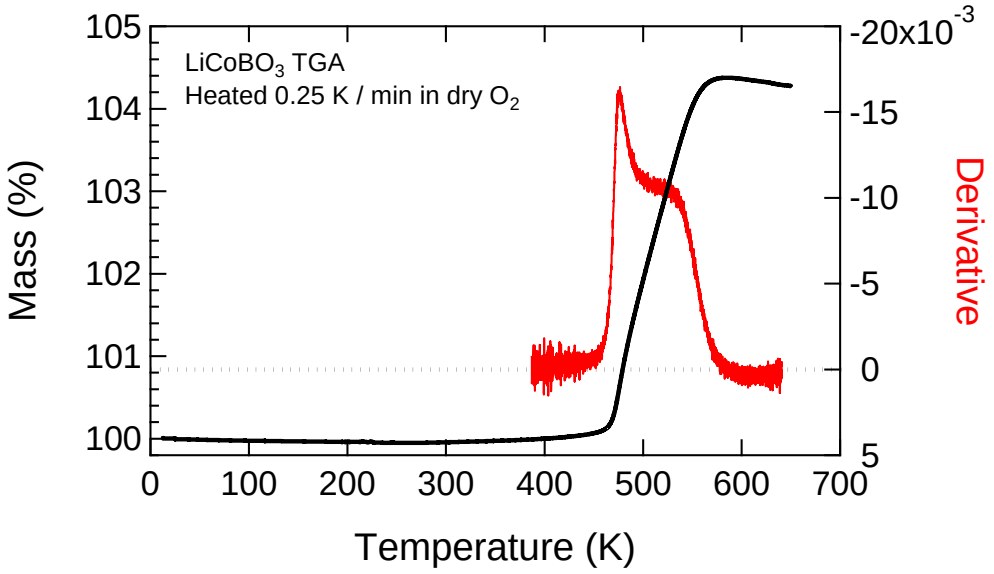

Figure 4.5. Thermogravimetric response of $LiCoBO_3$ powder heated under flowing oxygen at 0.25 ℃/ min. Derivative curve (red) indicates presence of at least two distinct mass gain processes. Figure is reproduced with permission from Ref 1.

The local structure of Li in the $LiCoBO_3$ framework also was directly probed using ^{7}Li solid state NMR. As shown in Figure 4.6, the ^{7}Li NMR spectrum of $LiCoBO_3$ is significantly broadened by the dipolar interactions between Li and the unpaired electrons associated with Co^{2+} [14]. When using a standard chemical shift spin echo (csecho) sequence, it is extremely difficult to identify the isotropic shift of Li in $LiCoBO_3$ due to the severe overlap of spinning sideband manifolds. However, the isotropic shift can be clearly resolved using a pj-MATPASS pulse sequence[11]. Compared to structural analogue of monoclinic $LiFeBO_3$, the isotropic peak of $LiCoBO_3$ is much broader (~100 KHz) and has a much smaller hyperfine shift (-40 ppm for $LiCoBO_3$, -233 ppm for $LiFeBO_3$ [4]). The smaller hyperfine shift of $LiCoBO_3$ is almost certainly a result of the smaller spin of Co^{2+} (S = 3/2) relative to Fe^{2+} (S = 2), as the extra d-electron in this ion (d^7 configuration) results in fewer unpaired electrons within the trigonal bipyramidal ligand environment. This trend of hyperfine shift variations in Li*M*BO_3 compounds can be rationalized based on the *M*-O-Li bond pathway decompositions [15], and is qualitatively consistent with the Li*M*PO_4 olivine system [16]. One possible source of broadening of the $LiCoBO_3$ isotropic resonance is structural disorder that results in a wider distribution of Li local environments. Since moderate levels of heating are known to cause Li/Fe anti-site disorder in the related compound $LiFeBO_3$, comparative measurements before and after an overnight air anneal at 100 ℃ of (1) the as-prepared $LiCoBO_3$ powders and (2) the as-prepared $LiCoBO_3$ electrode films were attempted to vary the extent of disorder. There is no observable change in the ^{7}Li NMR responses of these two $LiCoBO_3$ samples, suggesting that the framework of $LiCoBO_3$ remains unaltered (Figure 4.6). A second potential source of the observed broadening arises from the bulk anisotropic magnetic susceptibility broadening. This originates from the unquenched angular momentum associated with Co^{2+} [17] caused, in this case, by the mixing in of ground and excited

states by the spin-orbit coupling. This will generally result in line broadening that cannot be completely removed by magic angle spinning.

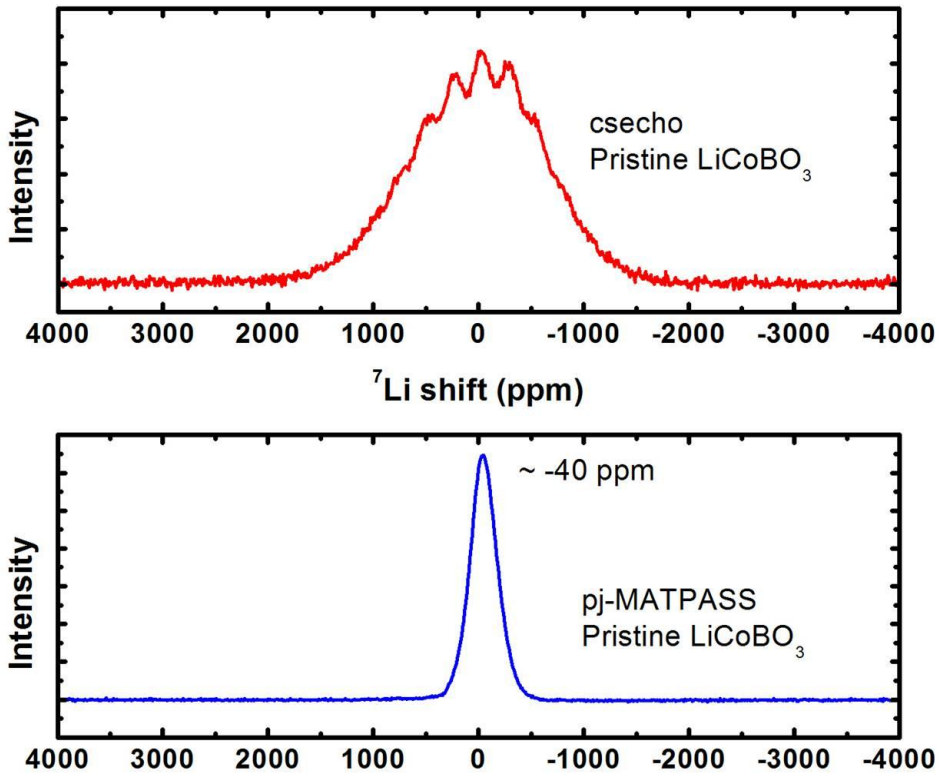

Figure 4.6. ^{7}Li NMR spectra of pristine $LiCoBO_3$ collected with the use of pj-MATPASS (bottom) and csecho (top) pulse sequences. Figure is reproduced with permission from Ref 1.

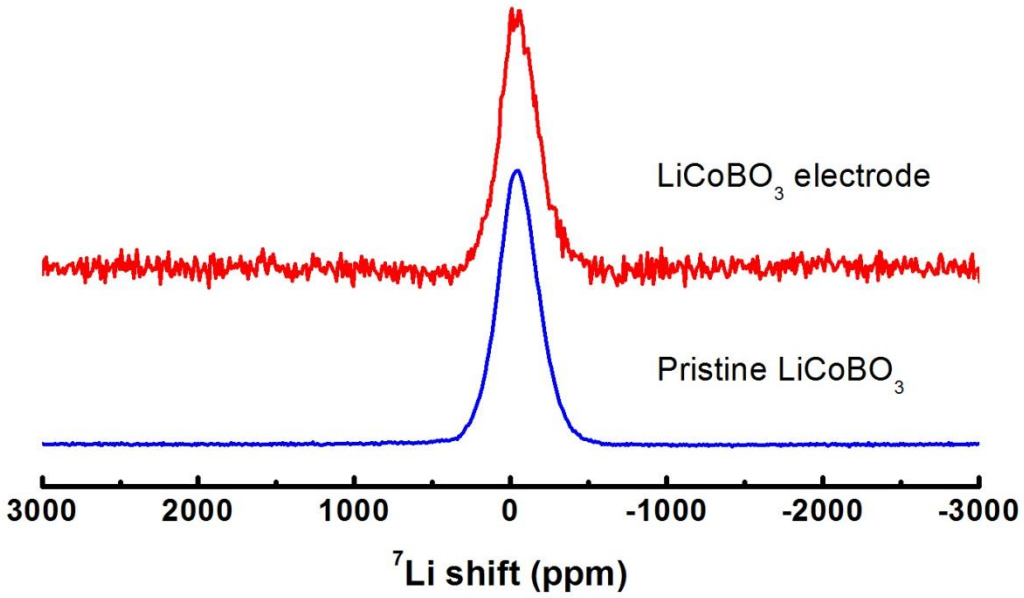

Figure 4.7. ^{7}Li NMR spectra of pristine $LiCoBO_3$ powder (bottom), and the $LiCoBO_3$ electrode film prepared after annealing at 100 ℃ in air (top). Figure is reproduced with permission from Ref 1.

4.3.2 Electrochemical and electrical studies

Preliminary electrochemical studies were first carried out using electrodes fabricated from powder samples of $LiCoBO_3$. The electrochemical performance of the as-prepared $LiCoBO_3$ ceramic powder was characterized by galvanostatic cycling from 2.0 - 4.5 V at a rate of C/100 (Figure 4.8). Similar to the observations by Legagneur *et al.* [18], the first charge exhibits a flat plateau (~5 mAh/g) that is promising in voltage, but corresponds to less than 2% of the theoretical capacity and which shows tremendous polarization on discharge where the initial electrochemical response begins at about 2.3 V. A slightly different response is observed for the second charge cycle (plateau region at ~3 V and sloped region above 3.5 V), though the second discharge is very much like the first. Although these features are not characteristic of robust

reversible electrochemistry, the large particle size of this powder and the tremendous theoretical specific energy density provide motivation for a more detailed investigation of samples with smaller particles sizes.

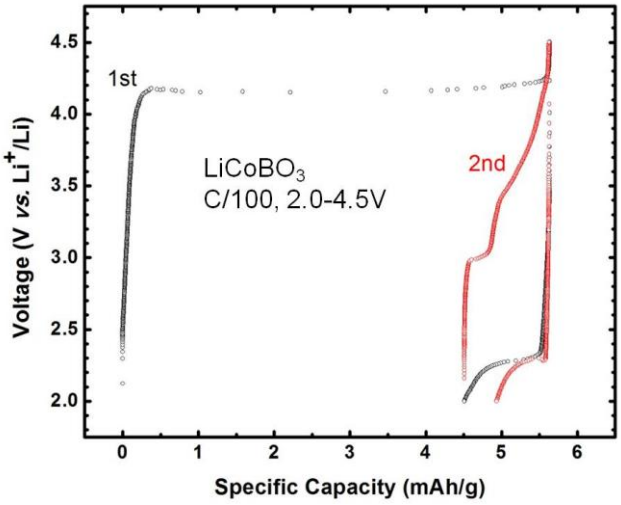

Figure 4.8. Electrochemical performance of micron-sized $LiCoBO_3$ powder sample. The battery was cycled between 2.0 and 4.5 V (*vs.* Li^+/Li) at a rate of C/100. Figure is reproduced with permission from Ref 1.

In contrast to the recent approaches adopted by other groups to prepare very fine powders of $LiCoBO_3$/C nanocomposites for electrochemical characterization [8, 19], we have chosen to instead prepare thin films by reactive magnetron sputter deposition to achieve greater control over the $LiCoBO_3$ electrode thickness. In the present study, film loadings as low as 14 $\mu g/cm^2$ have been prepared that correspond to vertical thicknesses as low as 15 nm (assuming a fully dense sample), allowing access to much smaller diffusion lengths than in powder studies. Although the net active material loading of sputtered films will be lower than that of cast films, sputtered films have the great advantage of having all of the crystalline grains in very close

proximity to the current collector, and should therefore in better electronic contact than films of cast powders.

Representative cycling data measured for a 40 nm thick $LiCoBO_3$ film is shown in Figure 4.9. Similar weight normalized capacities and voltage profiles were also measured for a number of additional samples with thicknesses varying from 15 nm to 2.2 μm thick (Figure 4.10). In all cases, during the first charge step a plateau was observed around 4.0 – 4.2 V *vs.* Li^+/Li. A corresponding plateau was not observed in the discharge plateau, which instead exhibited a highly sloped and nearly linear drop in voltage from 3.5 to 2.5 V. Subsequent cycles showed lower capacities which further decreased with cycling. In all cases the weight normalized capacities were around 1 – 2 mAh/g. This capacity is much lower than theoretically predicted for $LiCoBO_3$. Given that this capacity is consistent found for all $LiCoBO_3$ samples with various thicknesses, the low capacity observed for bulk ceramic powders is likely intrinsic to $LiCoBO_3$, and is perhaps capacitive in nature. For the thinnest films with the lowest net capacities, parasitic reactions occurring on the current collectors and cell hardware become a significant component in the observed electrochemical data. CV data measured for Pt coated Al in a typical coin cell configuration (Figure 4.9, inset), shows a significant oxidation current upon charging over 3.7 V. This suggests that the observed high voltage electrochemical response in the charge/discharge data from films is likely dominated by reactions between the current collectors and the electrolyte, a conclusion also supported by the anomalous behavior during the first charge cycle see in both powder and thin film studies of $LiCoBO_3$.

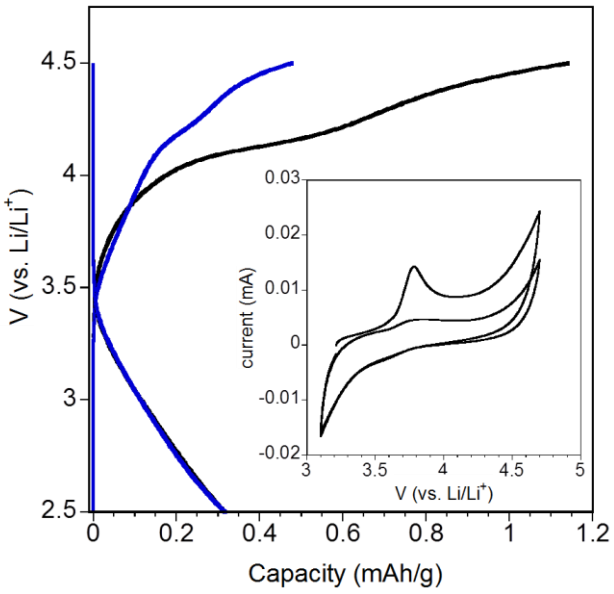

Figure 4.9. Electrochemical data collected for $LiCoBO_3$ film (40 nm nominal thickness) cycled against Li during the first (black) and second (blue) cycle with a 5 μA current. Inset: Cyclic voltammetry data collected for Pt films cycled against Li in the same electrolyte. Data was collected and analyzed in collaboration with Dr. Gabriel Veith from Oak Ridge National Lab. Figure is reproduced with permission from Ref 1.

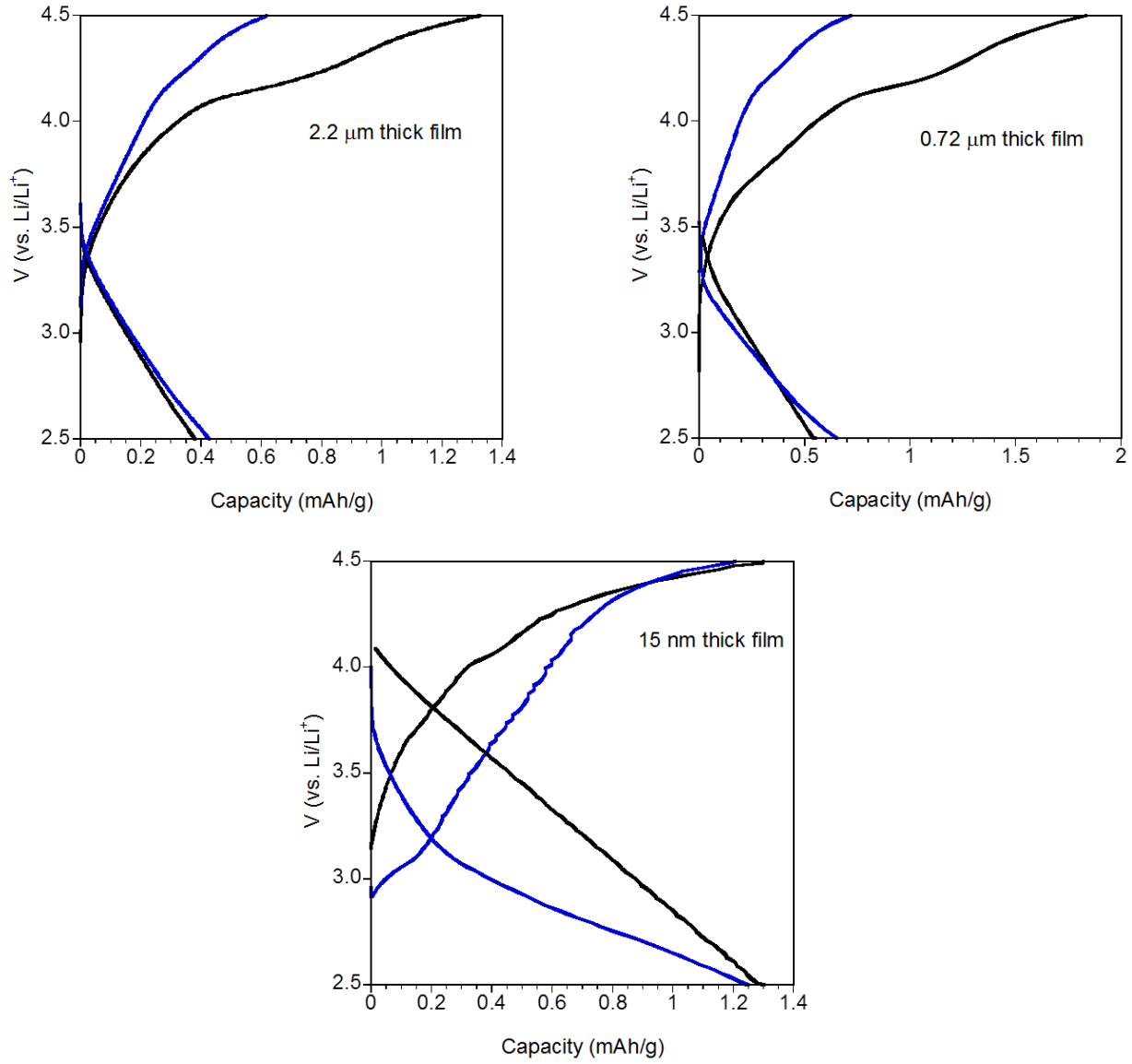

Figure 4.10. Electrochemical data collected for $LiCoBO_3$ films of various thicknesses cycled against Li during the first (black) and second (blue) cycle with a 5 μA current. Data was collected and analyzed in collaboration with Dr. Gabriel Veith from Oak Ridge National Lab. Figure is reproduced with permission from Ref 1.

In order to understand the origin of the apparent low capacity of the $LiCoBO_3$ films, $Pt/LiCoBO_3/Pt$ thin films (600 – 1000 nm thick) were prepared and evaluated using impedance

spectroscopy (Figure 4.11) after the standard annealing treatment at 600 ℃ in inert gas. The total conductivity for the $LiCoBO_3$ films obtained after normalizing for the sample area and thickness was in all cases around 1 x 10^{-12} S/cm. This conductivity value is approximately 7 orders of magnitude lower than $LiFePO_4$ [20] and as such can be the origin of the electrochemical inertness of even the thinnest films (~15 nm).

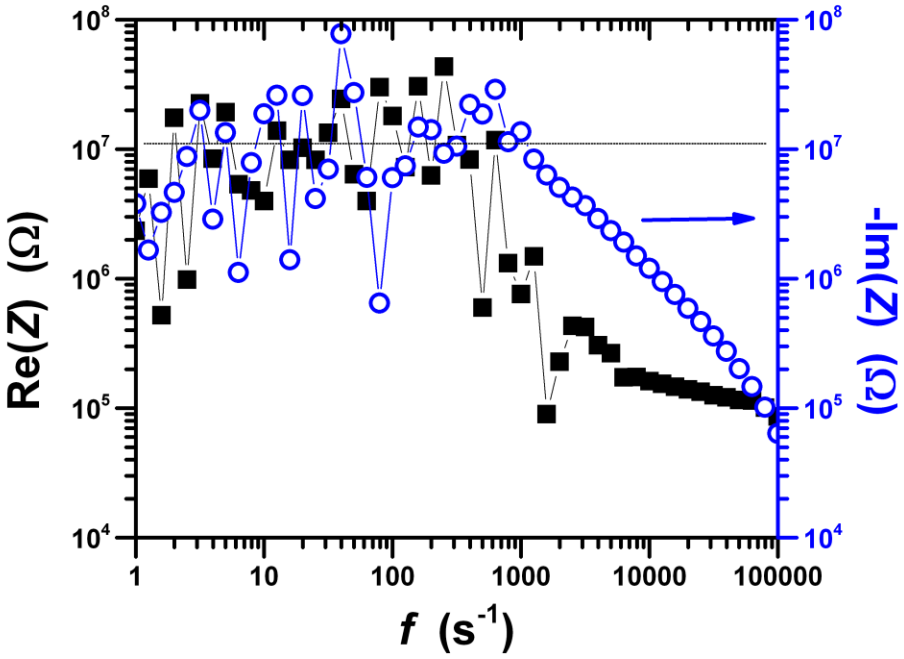

Figure 4.11. Impedance spectrum of a $LiCoBO_3$ thick film (~1 micron) collected at room temperature. Data was collected and analyzed in collaboration with Dr. Robert Sacci from Oak Ridge National Lab. Figure is reproduced with permission from Ref 1.

4.3.3 Optical studies

Direct feedback about the electronic states of transition metal compounds can be obtained from their optical properties. One of the simplest probes is diffuse reflectance spectroscopy,

which was used to study powders of both $LiCoBO_3$ and reference $LiFeBO_3$. The relative absorption coefficients of these two compounds in the ultraviolet and visible regime are shown in Figure 4.12. It should be remembered that diffuse reflectance spectroscopy is most sensitive to weakly absorbing features, and that the saturation of absorption at $\alpha_{KM} \sim 10$ is almost certainly due to a saturation of the instrumental response rather than an actual feature associated with these materials. A sharp onset of strong absorption characteristic of a direct excitation between the filled oxygen 2p states and the unoccupied transition metal d-electron states exists in both compounds, with a characteristic energy obtained by curve fitting of 3.21 eV for $LiFeBO_3$ and 4.22 eV for $LiCoBO_3$. This increase approximately corresponds to the expected ~1V increase in redox potential on substituting Co^{2+} for Fe^{2+}. At slightly lower energies, the absorption data can be fit to the logarithmic scaling expected for an Urbach tail, generally associated with sample inhomogeneity leading to a broadening of the main excitation. For both compounds, the estimated gap energy obtained from the Urbach tail fits closely corresponds to the much more precise results obtained from the direct gap fits, as is generally expected (Table 4.4). However, the characteristic energy scale of Urbach broadening is extremely large (1.2 eV for Co; 2.2 eV for Fe), about an order of magnitude broader than we normally observe for semiconductors with closed shells. It is not known whether this extreme broadening is intrinsic (*i.e.*, dynamical scattering processes associated with spins on the transition metal site, IVCT transitions involving neighboring transition metals [21]) or extrinsic (*i.e.*, anti-site disorder between the Li and transition metal, overlap of optical features) in nature.

Table 4.4. Results of Optical Fitting. Table is reproduced with permission from Ref 1.

	Direct fit	Urbach fit		
	E_g (eV)	E_U (eV)	Eg (eV)	A
$LiFeBO_3$	3.21	2.24	3.29	7.25
$LiCoBO_3$	4.22	1.18	4.27	3.92

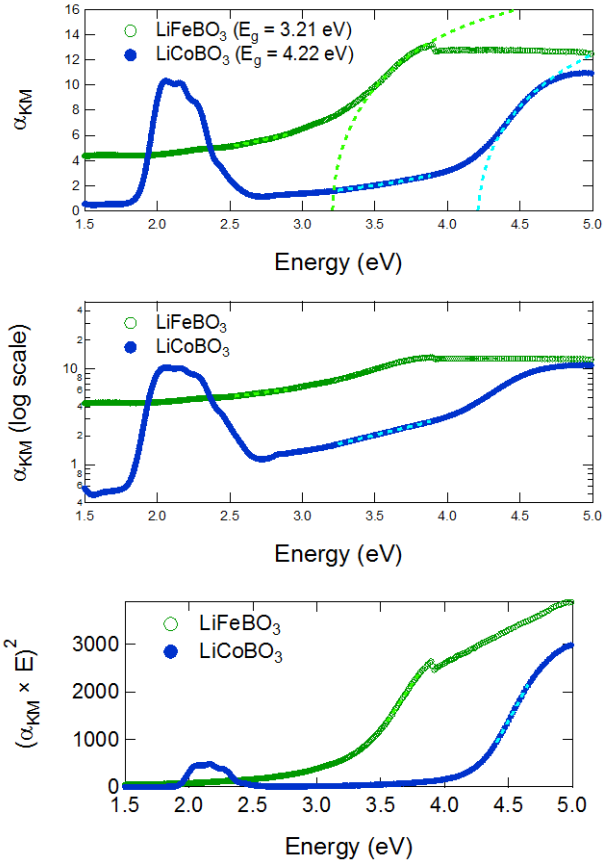

Figure 4.12. Optical response of $LiFeBO_3$ (green) and $LiCoBO_3$ (blue) measured in a diffuse reflectance spectrometer, plotted as a relative absorption (*via* a Kubleka-Munk transform) on a linear scale (top), on a logarithmic scale (center), or rescaled to vary linearly for direct optical transitions (bottom). Fits to a direct transition (above E_g) and Urbach tail response (below E_g)

are overlaid with dashed lines over their relevant energy ranges. Data was collected and analyzed in collaboration with Mr. Huafeng Huang and Mr. Andrew Malingowski. Figure is reproduced with permission from Ref 1.

The blue color of $LiCoBO_3$ is atypical, as most semiconductors are yellow, orange, red, or black, depending on the magnitude of their band gap. Furthermore, this color cannot be associated with the charge transfer gap of $LiCoBO_3$, which occurs at ultraviolet energies (~4.2 eV) according to fits of the diffuse reflectance data. The word "cobalt" is closely associated with the color blue, and one of the key industrial blue pigments is the normal spinel $CoAl_2O_4$, in which the Co^{2+} ion primarily occupies the tetrahedral site, though with a different symmetry and crystal field splitting than the trigonal bipyramidal environment of $LiCoBO_3$. The blue color of $LiCoBO_3$ originates from a discrete spectral feature in the visible regime that is centered at about 2.2 eV. It is expected that this feature is a d → d transition within the manifold of states associated with the trigonal bipyramidal environment of Co^{2+}, an ion with a HS d^7 configuration (Figure 4.13), though there is very limited literature precedent for the spectroscopic analysis of this rare coordination environment. Based on prior work on trigonal bipramidally coordinated Co^{2+} molecular species with nitrogen and other non-oxide ligands [25-26], we can confidently assign a $^4A_2'$ ground state to $LiCoBO_3$. The assignment excited states for the optical transitions of Co^{2+} in a CoN_5 molecular environment were previously reported to be: $^4A_1''$ (0.37 eV – calculated), $^4A_2''$ (0.44 eV – calculated), $^4E''$ (0.72 eV), $^4E'$ (1.83 eV), $^4A_2''$ (2.05 eV), $^4E''$ (2.60 eV), with the last two excitations beings associated with the higher energy ^4P free ion state rather than the lowest energy ^4F free ion state, and with the first two excitations occurring below the energy minimum (0.5 eV) of the experiment. Based on the energy level diagrams calculated for the

CoN_5 complex and the knowledge that O is a weaker field ligand than N, we assign the 2.2 eV excitation in $LiCoBO_3$ to overlapping $^4A_2{}''$ and $^4E''$ transitions as energies of these excitations should increase and decrease, respectively, with decreasing ligand field strength.

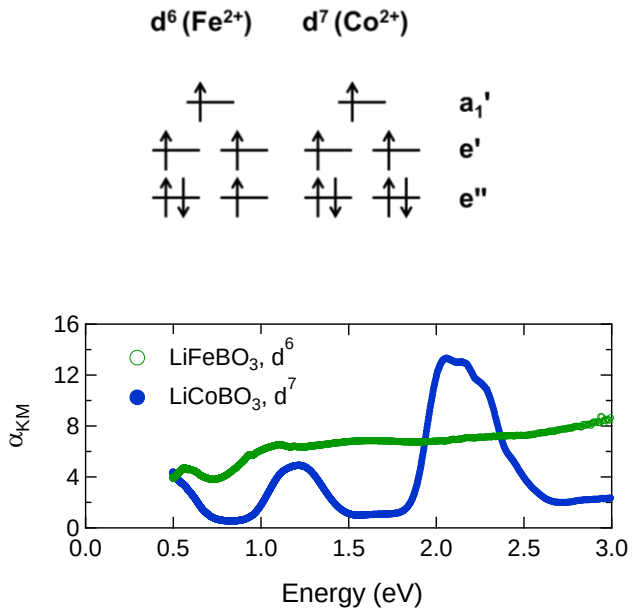

Figure 4.13. Optical response of $LiFeBO_3$ (green) and $LiCoBO_3$ (blue) from 0.5 – 3.0 eV obtained from biaxial reflection data, to which a Kubleka-Munk transform has been applied to coarsely estimate relative absorbances. Data was analyzed in collaboration with Dr. Kevin Kittilstved from University of Massachusetts. Figure is reproduced with permission from Ref 1.

Additional lower energy optical transitions for d^7 trigonal bipyramidal Co2+ can be observed in diffuse reflectance data (Figure 4.13) collected with a biaxial reflectometer that does not utilize an integrating sphere. A lower energy transition at 1.2 eV can be clearly resolved ($^4E'$) , while the high energy tail of an additional transition located slightly below 0.5 eV ($^4E''$) can also

be seen, and these states are assigned by analogy to the transitions observed at somewhat higher energies for the CoN_5 ligand environment. A simple ligand field model using parameters appropriate for an ideal D_{3h} symmetry CoO_5 ligand environment (oxygen e_σ = 0.40, Racah B = 0.10, Racah C = 0.35) predicts excitation energies of 0.33 ($^4A_1''$ + $^4A_2''$), 0.53 ($^4E''$), 1.43 ($^4E'$), 2.16 ($^4A_2''$), and 2.28 eV ($^4E''$), further validating the assignments and providing basic insights into the bonding of Co^{2+} in $LiCoBO_3$. A more advanced analysis should utilize single crystal polarized electronic spectroscopy, and should account for the fact that Co^{2+} occupies a general crystallographic site (8f Wykoff position) in the $LiCoBO_3$ structure and does not possess ideal D_{3h} symmetry. The optical response of d^6 Fe^{2+} in $LiFeBO_3$ in this same energy regime shows absorption from other spin-allowed transitions, but these transitions overlap to a much greater degree (resulting in the previously reported grey-brown color of this compound) and cannot be directly assigned from the present data. It is expected that color produced by Co^{2+} ions in the borate host structure can be effectively tuned by doping with divalent ions to form a solid solution such as $Li(Mg_{1-x}Co_x)BO_3$ or $Li(Zn_{1-x}Co_x)BO_3$, which are anticipated to modify the ligand binding strength as a consequence of lattice strain and/or ion electronegativity effects, thereby changing the hue of the blue color. Based on the light blue color of 100 nm thick films and the medium blue color of 1 micron thick films, the absorption coefficient of the 2.2 eV feature in $LiCoBO_3$ that gives rise to the blue color is coarsely estimated to be nearly 10^4 cm^{-1}, though attempts to more precisely fit the optical constants of films of this phase by spectral ellipsometry were unsuccessful. This strength of optical absorption is consistent with the spin-allowed nature of the transitions assigned to $LiCoBO_3$ in the present study.

4.4 Conclusions

Methods have been developed for the preparation of $LiCoBO_3$ in the form of both micron powders and submicron thin polycrystalline films. Both types of samples have been found to be electrochemically inert (even when films with a thickness of about 15 nm were used for measurements) and suggest that modifications other than particle size reduction are needed before viable performance metrics for a battery cathode can be achieved. No evidence for anti-site disorder is found, and it is suggested that the inertness of this phase is associated with either an excessively low conductivity (10^{-12} S/cm) and/or with a loss of stability that occurs upon oxidation. Optical transitions associated with the unusual blue color of this phase have been assigned to specific d→d transitions associated with the rare trigonal bipyramidal environment of high-spin d^7 Co^{2+} ions. The strong blue color and the good resistance of $LiCoBO_3$ against oxidation, and the previously reported methods for producing this phase in a nanoparticulate form suggest that this phase may have more utility as a pigment than as a cathode.

4.5 References

1. Bo, S.-H.; Veith, G. M.; Saccomanno, M. R.; Huang, H.; Burmistrova, P. V.; Malingowski, A. C.; Sacci, R. L.; Kittilstved, K. R.; Grey, C. P.; Khalifah, P. G., Thin-Film and Bulk Investigations of $LiCoBO_3$ as a Li-Ion Battery Cathode. *ACS Applied Materials & Interfaces* **2014**.

2. Padhi, A. K.; Nanjundaswamy, K. S.; Goodenough, J. B., Phospho-olivines as positive-electrode materials for rechargeable lithium batteries. *J Electrochem Soc* **1997,** *144* (4), 1188-1194.

3. Malik, R.; Abdellahi, A.; Ceder, G., A Critical Review of the Li Insertion Mechanisms in $LiFePO_4$ Electrodes. *J Electrochem Soc* **2013,** *160* (5), A3179-A3197.

4. Bo, S. H.; Wang, F.; Janssen, Y.; Zeng, D. L.; Nam, K. W.; Xu, W. Q.; Du, L. S.; Graetz, J.; Yang, X. Q.; Zhu, Y. M.; Parise, J. B.; Grey, C. P.; Khalifah, P. G., Degradation and (de)lithiation processes in the high capacity battery material $LiFeBO_3$. *J Mater Chem* **2012,** *22* (18), 8799-8809.

5. Yamada, A.; Iwane, N.; Harada, Y.; Nishimura, S.; Koyama, Y.; Tanaka, I., Lithium Iron Borates as High-Capacity Battery Electrodes. *Adv Mater* **2010,** *22* (32), 3583-3587.

6. Bo, S.-H.; Nam, K.-W.; Borkiewicz, O. J.; Hu, Y.-Y.; Yang, X.-Q.; Chupas, P. J.; Chapman, K. W.; Wang, F.; Grey, C. P.; Khalifah, P. G., Structures of delithiated and degraded $LiFeBO_3$, and their distinct changes upon electrochemical cycling. *Inorganic Chemistry* **2014**

7. Yamada, A.; Iwane, N.; Nishimura, S.; Koyama, Y.; Tanaka, I., Synthesis and electrochemistry of monoclinic $Li(Mn_xFe_{1-x})BO_3$: a combined experimental and computational study. *J Mater Chem* **2011,** *21* (29), 10690-10696.

8. Yamashita, Y.; Barpanda, P.; Yamada, Y.; Yamada, A., Demonstration of Co^{3+}/Co^{2+} Electrochemical Activity in $LiCoBO_3$ Cathode at 4.0 V. *Ecs Electrochem Lett* **2013,** *2* (8), A75-A77.

9. Baggetto, L.; Unocic, R. R.; Dudney, N. J.; Veith, G. M., Fabrication and characterization of Li-Mn-Ni-O sputtered thin film high voltage cathodes for Li-ion batteries. *J Power Sources* **2012,** *211*, 108-118.

10. Li, J. C.; Baggetto, L.; Martha, S. K.; Veith, G. M.; Nanda, J.; Liang, C. D.; Dudney, N. J., An Artificial Solid Electrolyte Interphase Enables the Use of a $LiNi_{0.5}Mn_{1.5}O_4$ 5 V Cathode with Conventional Electrolytes. *Adv Energy Mater* **2013,** *3* (10), 1275-1278.

11. Hung, I.; Zhou, L. N.; Pourpoint, F.; Grey, C. P.; Gan, Z. H., Isotropic High Field NMR Spectra of Li-Ion Battery Materials with Anisotropy > 1 MHz. *J Am Chem Soc* **2012,** *134* (4), 1898-1901.

12. Dong, Y. Z.; Zhao, Y. M.; Shi, Z. D.; An, X. N.; Fu, P.; Chen, L., The structure and electrochemical performance of $LiFeBO_3$ as a novel Li-battery cathode material. *Electrochim Acta* **2008,** *53* (5), 2339-2345.

13. Janssen, Y.; Middlemiss, D. S.; Bo, S. H.; Grey, C. P.; Khalifah, P. G., Structural Modulation in the High Capacity Battery Cathode Material $LiFeBO_3$. *J Am Chem Soc* **2012,** *134* (30), 12516-12527.

14. Grey, C. P.; Dupre, N., NMR studies of cathode materials for lithium-ion rechargeable batteries. *Chem Rev* **2004,** *104* (10), 4493-4512.

15. Middlemiss, D. S.; Ilott, A. J.; Clement, R. J.; Strobridge, F. C.; Grey, C. P., Density Functional Theory-Based Bond Pathway Decompositions of Hyperfine Shifts: Equipping Solid-State NMR to Characterize Atomic Environments in Paramagnetic Materials. *Chem Mater* **2013,** *25* (9), 1723-1734.

16. Tucker, M. C.; Doeff, M. M.; Richardson, T. J.; Finones, R.; Cairns, E. J.; Reimer, J. A., Hyperfine fields at the Li site in $LiFePO_4$-type olivine materials for lithium rechargeable batteries: A Li-7 MAS NMR and SQUID study. *J Am Chem Soc* **2002,** *124* (15), 3832-3833.

17. Tao, L.; Neilson, J. R.; Melot, B. C.; McQueen, T. M.; Masquelier, C.; Rousse, G., Magnetic Structures of $LiMBO_3$ (M = Mn, Fe, Co) Lithiated Transition Metal Borates. *Inorg Chem* **2013,** *52* (20), 11966-11974.

18. Legagneur, V.; An, Y.; Mosbah, A.; Portal, R.; La Salle, A. L.; Verbaere, A.; Guyomard, D.; Piffard, Y., $LiMBO_3$ (M = Mn, Fe, Co): synthesis, crystal structure and lithium deinsertion/insertion properties. *Solid State Ionics* **2001,** *139* (1-2), 37-46.

19. Afyon, S.; Mensing, C.; Krumeich, F.; Nesper, R., The electrochemical activity for nano-$LiCoBO_3$ as a cathode material for Li-ion batteries. *Solid State Ionics* **2014,** *256* (0), 103-108.

20. Wang, C.; Hong, J., Ionic/Electronic Conducting Characteristics of $LiFePO_4$ Cathode Materials: The Determining Factors for High Rate Performance. *Electrochemical and Solid-State Letters* **2007,** *10* (3), A65-A69.

21. Furutsuki, S.; Chung, S. C.; Nishimura, S.; Kudo, Y.; Yamashita, K.; Yamada, A., Electrochromism of Li_xFePO_4 Induced by Intervalence Charge Transfer Transition. *J Phys Chem C* **2012,** *116* (29), 15259-15264.

Chapter 5

Defect-tolerant Mg diffusion channels in ribbon-type borates: structure insights into potential battery cathodes $MgVBO_4$ and $Mg_xFe_{2-x}B_2O_5$

5.1 Introduction

While Li-ion battery technology is currently dominant for mobile electronics applications, the growing demand for inexpensive and safe energy storage for powering large-scale devices such as electric vehicles and grid scale storage has motivated renewed efforts to use multivalent ions such as Mg^{2+} in recharge batteries. Mg-ion batteries are expected to have advantages in safety and cost, benefits primarily derived from the usage of Mg metal anodes[1]. There are still many practical challenges which must be overcome before Mg-ion systems are suitable for practical applications, including the challenges of designing good electrolytes, the exceedingly limited mobility of Mg^{2+} ions in most solid state frameworks, and the lack of cathodes with high specific capacities, which are required to achieve the energy densities needed to displace competing technologies already existing for monovalent mobile ions[2]. It is therefore particularly important to search for new Mg-ion cathode materials, though the few examples of existing Mg-ion cathodes with any appreciable capacity provide little guidance in this search[2-5].

Borate based polyanion compounds are promising systems in which to search for novel cathode for battery applications, since (1) oxoanion groups provide an inductive effect that can enhance the operating voltage and thus improve the overall energy density, and (2) among the common oxanion groups (*e.g.*, phosphates, silicates, sulfates), the mass/charge (*m*/*z*) ratio of the borate group is the lightest. There have been a number of recent studies demonstrating the

potential of borate based compounds as high-capacity cathode materials for lithium-ion batteries[6-8]. These studies motivated the present investigation of magnesium metal borates for their potential utility as cathode materials in Mg-ion battery applications.

There are a number of borate structures in which there are known examples of redox-active transition metals coexisting with divalent Mg cations. For the present study, two very similar "ribbon" frameworks which contain 4 parallel chains of edge sharing octahedra (Figure 5.1) were studied. The compound $MgVBO_4$ belongs to an orthoborate structural family (*i.e.*, warwickite) having a general stoichiometry of M_2BO_4 (M = Mg, Sc, Ti and Fe) with isolated BO_3^{3-} polyanion groups connecting the ribbons [9-11]. Most compounds of this type have two or more cations distributed over the M sites. The one compound in this family which has a single M cation is Fe_2BO_4, which has superstructure peaks associated with an unusually strong charge ordering that drives nearly complete separation into sites with valences of either Fe^{2+} or Fe^{3+} below room temperature, has an incommensurate structure at intermediate temperature, and loses all evidence of charge order in the average structure at elevated temperatures [12-13]. The second pyroborate framework has the general stoichiometry $M_2B_2O_5$ with the boron ions found in the form of dimeric $B_2O_5^{4-}$ polyanion blocks that stitch the ribbons together in a slightly different manner. The compounds $Mg_2B_2O_5$ and $Fe_2B_2O_5$ both have the same geometric connectivity, though $Mg_2B_2O_5$ can be synthesized in both a triclinic (suarite type, space group *P-1*, #2) [14], [15] and monoclinic polymorph (space group $P2_1/c$, #14) [16], while $Fe_2B_2O_5$ has only been observed in the triclinic structural type [17]. The monoclinic structure has twice the volume of the triclinic cell, the change resulting from the doubling of the *b*-axis of the triclinic cell.

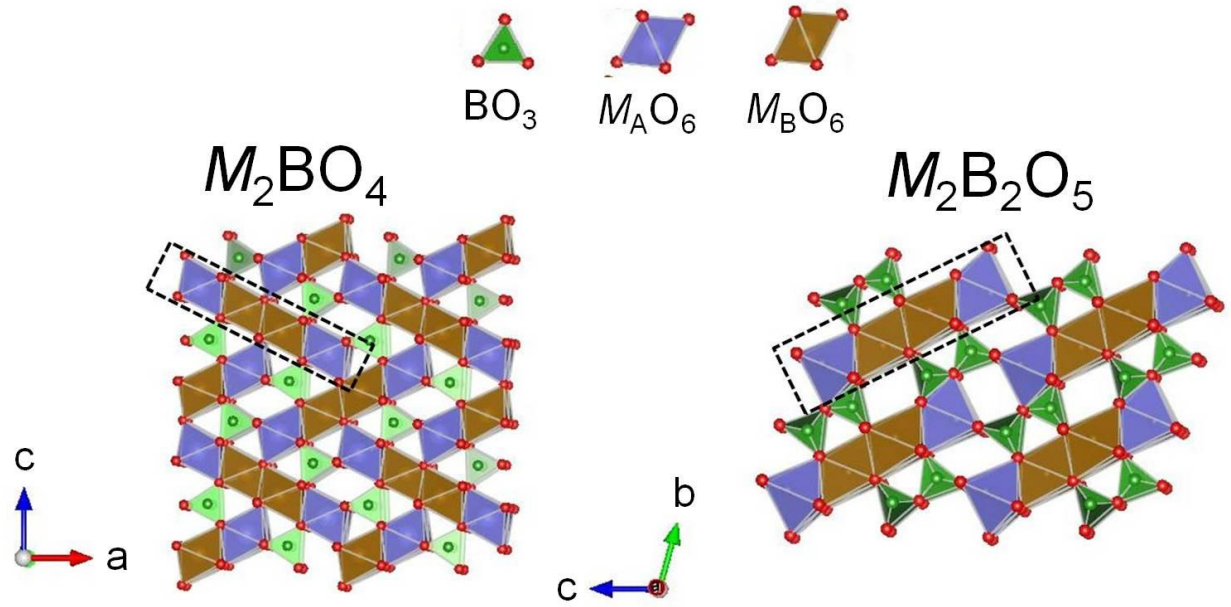

Figure 5.1. Crystal structures of the M_2BO_4 (left, space group *Pnma*) and $M_2B_2O_5$ (right, space group $P\bar{1}$) family of compounds, where *M* stands for transition metal. Dashed rectangles indicate the 4-column ribbons of edge-sharing octahedra in which the Mg^{2+} and *M* cations reside. These ribbons have two distinct crystallographic sites denoted as M_A (blue octahedra) and M_B (brown octahedra). The B^{3+} cations are found at the center of either isolated BO_3^{3-} groups in the Mg*M*BO_4 orthoborates, or in dimeric $B_2O_5^{4-}$ groups in the Mg*M*B_2O_5 pyroborates.

In both the orthoborate and pyroborate structures, there are two crystallographic sites for the *M* cations, indicating two distinct environments for the *M* cations which have different free energies. This has two important implications. First, when two different M cations are used in the structure, there is a possibility of partial or complete ordering over these two distinct sites. Second, the local environment is quite different for both sites and it is therefore expected that the mobility of a given ion may strongly depend on the specific site in which it is found. The outer

two chains of terminal octahedra in the ribbbons are both associated with one crystallographic site, denoted M_A, while the central two chains of octahedra in each ribbon are associated with a second site, denoted M_B. In the pyroborate $M_2B_2O_5$ compounds, the quadruple-chain ribbons are isolated from each other and are arranged parallel to each other with no shared oxygens. In contrast, the ribbons in the orthoborate M_2BO_4 compounds occur in a nearly perpendicular arrangement, with the each terminal M_AO_6 octahedron corner-sharing an oxygen with three central M_BO_6 octahedra in a neighboring ribbon. This shared oxygen site is the only oxygen site which is not part of a BO_3 triangle, and presumably its higher number of neighboring octahedra (four in total) relative to the other oxygen sites is required to satisfy the bonding and valence requirements of this shared site in the absence of bonding contributions from borate groups.

Based on a structural analysis, it is expected that these compounds may be useful for battery applications. It is known that edge-sharing chains of MO_6 octahedra can give rise to metallic conduction, and the chains in these compounds may facilitate sufficient electronic conductivity for electrochemical cycling to be possible. The ability of these borate frameworks to support ionic conduction is as-yet unknown, and it is a goal of the present work to obtain a better understanding of potential ionic diffusion processes in these frameworks. While the focus here is on Mg^{2+} ions, it is also expected that Li^+ ions can be hosted by these structural frameworks. The ability of the ribbon frameworks to support electronic and ionic conduction will certainly depend on the structural distribution of cations over the inequivalent M_A and M_B sites at the edges and centers of the chains, and it is important to quantify the relative proportion of mobile and redox-active cations over these two types of sites. The present work investigates the structures of $MgVO_4$ and the $Mg_xFe_{2-x}B_2O_5$ solid solution, two sets of compounds which contain

Mg^{2+} as potentially the mobile ion, and V^{3+} or Fe^{2+} as the redox-active ion which will be oxidized during Mg removal.

Based on general crystal chemical principles, the presence of disorder at M_A and M_B sites is expected to be most likely when cations are similar in both valence and size. It is therefore expected that Mg^{2+} (0.72 Å) is more likely to be disordered when mixed with Fe^{2+} (0.78 Å) than with V^{3+} (0.64 Å). Disorder has been previously observed for structural analogues of both $MgVO_4$ ($MgTiBO_4$, $MgScBO_4$) and $Mg_xFe_{2-x}B_2O_5$ ($Mg_xMn_{2-x}B_2O_5$) [9-10,18-19]. While the orthorhombic lattice parameters of the orthoborate $MgVO_4$ have previously been determined for samples prepared either through conventional solid state synthesis[20] or by electrolysis[21], there have been no structural studies of the atomic site positions and occupancies in this structure. The triclinic pyroborates $Mg_2B_2O_5$ and $Fe_2B_2O_5$ have been previously synthesized and characterized before, including both X-ray powder diffraction and single crystal diffraction studies[15, 17, 22-23], However, the battery-relevant solid solution compositions of $Mg_xFe_{2-x}B_2O_5$ have not previously been prepared, although closely related $Mg_xMn_{2-x}B_2O_5$ compounds have been previously synthesized [19].

Bond valence sum (BVS) maps were calculated for some control compounds ($FePO_4$, $MgMnSiO_4$ and Mo_6S_8) as well as using our refined structural data for orthoborate $MgVBO_4$ and pyroborate $Mg_xFe_{2-x}B_2O_5$ to investigate the diffusion pathways in these compounds. The bond valence sum (BVS) difference map approach calculates the valence of the target ion at each point in a user-defined three dimensional grid according to a set of empirically parameterized "soft" bond valence parameters, and calculates the absolute value of the difference $|\Delta V|$ between the ideal and calculated valence in order to investigate the positions within a structure that the potentially mobile ion might be able to thermally access [27-28]. In this approach, the valence is

calculated from the distance between the cation and nearby anion sites, with the valence contribution from each bond (in valence units, v.u.) increases exponentially with decreasing cation-anion distance. This method has been successfully applied to a broad spectrum of battery materials to provide specific insights into likely ion diffusion pathways and coarse estimates of their activation barriers. The size of the threshold value of $|\Delta V|$ that is needed to establish a percolation pathway provides a criterion for judging whether the barrier for diffusion is expected to be small, modest, or large. While the BVS difference map method has been commonly applied to study Li-ion diffusion, it has not previously been applied to Mg-ion systems.

In this work, we have synthesized polycrystalline samples of $MgVBO_4$ (theoretical capacity of 360 mAh/g) and $Mg_xFe_{2-x}B_2O_5$ (the highest theoretical capacity of 186 mAh/g based on Fe^{3+}/Fe^{2+} redox couple, and 295 mAh/g based on Fe^{4+}/Fe^{2+} redox couple) and characterized them through the combined Rietveld refinement of synchrotron X-ray and time-of-flight neutron diffraction. This has enabled the preliminary assessment of potential Mg^{2+} diffusion pathways through the calculation of bond valence sum maps. The removal of Mg^{2+} from these compounds has been attempted both by room temperature chemical methods and by high temperature solid state methods, enabling structural studies of demagnesiated ribbon compounds. Based on these results, some general conclusions can be made about the factors influencing the mobility of Mg^{2+} ions within these frameworks.

5.2 Experimental

Synthesis: $MgV^{11}BO_4$ powders (typically ~6 g batches) were prepared using starting materials of magnesium acetate tetrahydrate ($MgAc_2$ $4H_2O$, Spectrum, A. C. S. reagent), V_2O_5

(Alfa Aesar, 99.6 % min) and $^{11}B_2O_3$ (ISOTEC, 99 atom % ^{11}B). Since structural characterization by neutron diffraction was a goal, samples were prepared using ^{11}B instead of natural boron (^{10}B is an extremely strong neutron absorber). These starting materials were mixed with a ratio of 2 : 1 : 1.10 to avoid boron deficiencies in the final product. This ratio was initially optimized for the synthesis of $Mg_2{}^{11}B_2O_5$ under similar reaction conditions, and the need for excess boron is likely associated with the strong hydrophilic nature of B_2O_3 and/or boron volatility during the high-temperature synthesis. The precursor powders were ball milled in a zirconia ball mill jar for 100 minutes with a SPEX SamplePrep8000 Mixer/Mill high energy ball mill. The resulting powder was placed into a graphite crucible and loaded into a tube furnace which was purged with the 5% H_2/95% N_2 ("forming gas") for approximately 30 minutes. The sample was then reacted at 1200 ℃ for 10 hours under flowing forming gas (~30 mL/min). Enriched $Mg_xFe_{2-x}{}^{11}B_2O_5$ (x = 2/3 and 4/3) samples were synthesized in an equivalent manner using $MgAc_2 \cdot 4H_2O$ (Spectrum, ACS grade reagent), $FeC_2O_4 \cdot 2H_2O$ (Alfa Aesar, 99%) and $^{11}B_2O_3$ (ISOTEC, 99 atom % ^{11}B) as starting materials, but with a lower final reaction temperature of 950 ℃. The product of the synthesis was very sensitive to the temperature and gas flow rate as higher temperatures and gas flow rates could drive the reduction of Fe^{2+} to Fe metal.

Diffraction: Laboratory X-ray diffraction for phase identification was carried out in a in a flat plate Bragg-Brentano geometry using a Bruker D8 Advance detector (217.5 mm radius) with a Cu K source and a 192-channel LynxEye detector with coarse energy sensitivity (~25%) that was used with lower level (0.19 V) and window (0.06 V) settings to minimize sample fluorescence for Fe-containing samples. Synchrotron X-ray diffraction data were collected at the 11-BM beamline (λ = ~0.41Å) of the Advance Photon Source (APS) at Argonne National

Laboratory with samples loaded in 0.5 mm diameter Kapton capillaries. Time-of-flight neutron diffraction data were collected at the POWGEN beamline of Spallation Neutron Source (SNS) at Oak Ridge National Laboratory (ORNL). Different aliquots of the same ground powder sample were used for the equivalent X-ray and neutron experiments, as is ideal for data used for co-refinements. The central wavelength for the time-of-flight neutrons was chosen to be 1.066 Å, with a wavelength range of 0.533 Å to 1.599 Å and a minimum *d*-spacing of ~0.28 Å. Data were collected on samples packed in 6 mm vanadium cans. Rietveld refinement of diffraction data was done using the TOPAS v4.2 software package. In the combined refinement utilizing both neutron and X-ray diffraction data, the weighting scheme was adjusted so that X-ray and neutron data contributed equally to the weighted R value (R_{wp}) of the refinement. Although a geometrically correct absorption correction cannot presently be applied to the POWGEN data since a large number of different detector positions are utilized, an empirical implementation of the standard cylindrical wavelength-dependent absorption correction was utilized that could approximately determine the linear absorption coefficient (μ_L) based on calibration against a data set of $La^{11}B_6$ on the same instrument.

5.3 Results and discussion

5.3.1 $MgVBO_4$

The element vanadium is well-suited for cathodes due to both the high voltage it typically generates, and the multiple oxidation states (*i.e.*, 3+, 4+ and 5+) it can access in certain structures [24-25]. One large advantage of the use of divalent Mg^{2+} is that the number of mobile ions which need to be removed from the structure is halved relative to Li analogues, and enhanced specific

capacities associated with accessing multiple valence states of vanadium can be accessed even in compounds with equimolar amounts of mobile and redox-active cations. Thus the theoretical capacity of $MgVBO_4$ is 360 mAh/g. The complete removal of Mg^{2+} from $MgVBO_4$ will result in the oxidation state of V being increased from 3+ to 5+, though it is well known that the demagnesiation of structures is very difficult due to the poor mobility of Mg^{2+}, and it is therefore be expected that it would be difficult to electrochemically drive the formation of VBO_4 from $MgVBO_4$ cathodes at room temperature. The nature of the distribution of Mg and V over the two cation sites in the orthorhombic M_2BO_4 structure type can greatly impact the mobility of Mg^{2+}, and samples of $MgVBO_4$ were therefore prepared to elucidate its structure through powder diffraction studies. Theoretical methods (such as DFT or bond valence sum maps) can be used to estimate the Mg^{2+} diffusion path and the associated barriers.

The structure of $MgVBO_4$ was determined through the combined Rietveld refinement of synchrotron X-ray and time-of-flight neutron diffraction data using polycrystalline samples prepared at 1200 ℃. Although time-of-flight neutron diffraction is by itself often sufficient to obtain accurate structural information, the scattering from V is almost completely incoherent, making V essentially impossible to be resolved by neutron diffraction experiments and necessitating the more complex combined Rietveld refinement with X-ray diffraction data. Isotopic ^{11}B enriched $MgV^{11}BO_4$ was investigated in lieu of a sample with naturally abundant boron to avoid the severe neutron absorption of ^{10}B and the problems associated with this (for brevity, we will omit the isotopic identifier for our $MgV^{11}BO_4$ samples in the subsequent text). The diffraction patterns of as-prepared $MgVBO_4$ was successfully indexed based on the orthorhombic space group (*Pnma*, #62) previously suggested for this phase[20-21], with cell dimensions of a = 9.25129(4) Å, b = 3.10322(1) Å and c = 9.36991(4) Å obtained through

Rietveld refinement (Fig. 5.2). High quality diffraction data were obtained using both X-rays (satisfactory counting statistics to ~0.5 Å) and neutrons (~0.4 Å), allowing structural parameters for the atoms in $MgVBO_4$ to be accurately determined, as reported in Table 5.1. Noting that the use of two different types of radiation does permit the simultaneous refinement of three different species (Mg^{2+}, V^{3+}, and vacancies) on the outer M_A and inner M_B cation sites, no evidence was found for cation vacancies. When the M_A and M_B sites were constrained to be fully occupied, the refined stoichiometry of the sample is $Mg_{1.01}V_{0.99}BO_4$, which does not significantly differ from target composition of "$MgVBO_4$". Therefore, the final refinement was carried out with the cation sites constrained to be fully occupied at the ideal stoichiometry. The outer M_A site had a Mg^{2+} occupancy of 80% while the inner M_B site had a V^{3+} occupancy of 80%, indicating the site preferences of these cations. The same distribution of Mg/V was obtained by either allowing the thermal parameters of M_A and M_B sites to be freely refined, or constraining them to be same (the latter test resulted in a slightly increased R_{wp}). While this data clearly indicates that Mg/V site disorder can be stabilized in a well-crystallized phase, it is not known if alternative thermal treatments (longer heating, different annealing temperatures, and/or rapid quenching) can be applied to eliminate this disorder. Additional future experiments will be required to explore this question. The presence of site disorder is expected to be detrimental to both the electronic and ionic conductivity of this compound, of which the poor ionic conductivity is also supported by the bond valence sum map analysis, as will be discussed later.

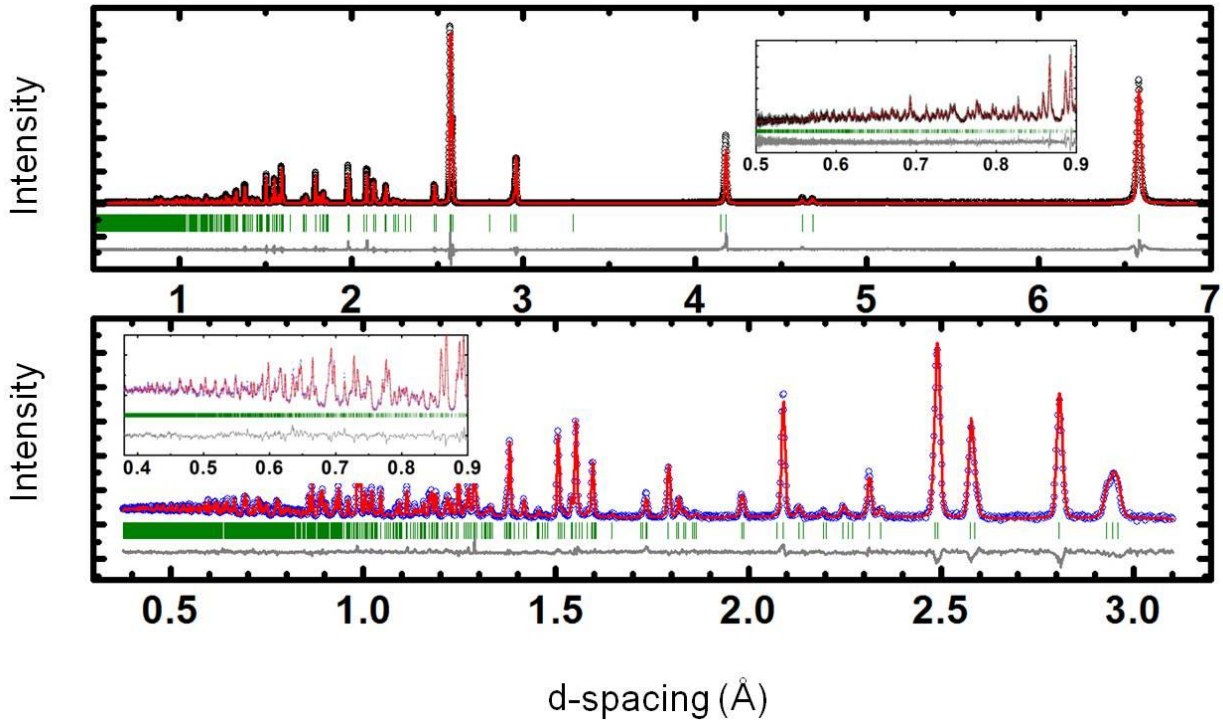

Figure 5.2. Combined Rietveld refinement of a single sample of $MgV^{11}BO_4$ using monochromatic synchrotron (top, λ = 0.41 Å) and polychromatic time-of-flight neutron data. The modeled intensities (red line), difference pattern (gray line), and predicted reflection positions (green ticks) are superimposed on the data points (blue circles).

Table 5.1. Atomic coordinates and thermal parameters of $MgVBO_4$ *(Pnma*, #62)

Atom	**Wyck.**	***x/a***	***y/b***	***z/c***	**Occ.**	**B_{iso} (Å^2)**
M_A	4c	0.10289(5)	0.25	0.69044(5)	Mg = 0.791(2) V = 0.209(2)	1.35(5)
M_B	4c	0.11716(4)	0.25	0.06704(4)	Mg = 0.209(2) V = 0.791(2)	0.50(1)
B	4c	0.1668(1)	0.25	0.3735(1)	1	0.60(1)
O1	4c	0.0205(1)	0.25	0.3673(1)	1	0.46(1)
O2	4c	0.5098(1)	0.25	0.6158(1)	1	0.56(2)
O3	4c	0.2383(1)	0.25	0.5058(1)	1	0.49(1)
O4	4c	0.2473(1)	0.25	0.2476(1)	1	0.44(1)

When the possibility of Mg removal from $MgVBO_4$ was tested through both chemical and thermal means, no evidence for demagnesiation was found in X-ray diffraction and in TGA data (Figure 5.3). The room temperature chemical oxidation of $MgVBO_4$ was performed by immersing powders into a saturated aqueous $K_2S_2O_8$ solution (~0.2 M). Thermal oxidation was carried out both under flowing oxygen gas (TGA) and in ambient air in a box furnace (*ex situ* XRD data). The persulfate solution has the advantage of a stronger electrochemical driving force for the demagnesiation reaction (about 5 V *vs.* Li^+/Li [26]), while thermal oxidation has a very substantial kinetic advantage due to the elevated temperature. The fact that none of these methods produces demagnesiated $MgVBO_4$ suggests that the present disordered $MgVBO_4$ sample is not suitable for electrochemical storage applications, even in devices which utilize solid state electrolytes and can be run at elevated temperatures. These results do not rule out the possibility of observing electrochemical activity for ordered $MgVBO_4$, which is expected to have greatly enhanced electronic and ionic conductivity relative to the present disordered sample.

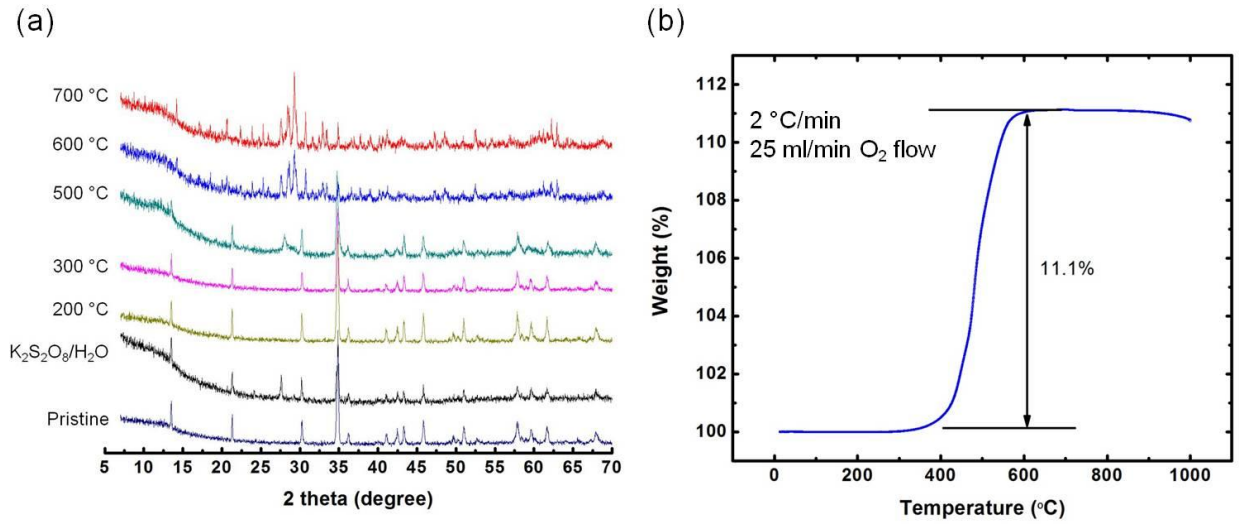

Figure 5.3. XRD patterns (Cu K_α) of pristine $MgVBO_4$, and those after soaking in $K_2S_2O_8/H_2O$ solution or heating at various temperatures under air are shown in (a). We did not observe any

diffraction pattern change corresponding to the $MgVBO_4$ phase after soaking the sample in $K_2S_2O_8/H_2O$ solution for 1 day at room temperature. The additional peak at ~27 ℃ in 2θ can be assigned to residual $K_2S_2O_8$. The diffraction patterns above 500 ℃ show additional peaks suggesting $MgVBO_4$ decomposition (MgV_2O_6 and $Mg_2V_2O_7$ with both having V^{5+}). This XRD result is in excellent agreement with our TGA results shown in (b).

5.3.2 $Mg_xFe_{2-x}B_2O_5$

Although neither $Mg_2B_2O_5$ nor $Fe_2B_2O_5$ have the combination of mobile cations and redox active cations needed for battery functionality, these compounds share the same structure type [15,17] and a solid solution of these two end members might be expected to form and to be suitable for electrochemical storage applications. Both a Fe-rich sample ($Mg_{2/3}Fe_{4/3}B_2O_5$, x = 2/3) and a Mg-rich sample ($Mg_{4/3}Fe_{2/3}B_2O_5$, x = 4/3) were prepared in the ^{11}B enriched form to evaluate the possibility of Mg-removal from this structure type (where ^{11}B is used to avoid the neutron absorption issue). The Fe-rich compound has a better possibility of achieving a Fe-percolating network within the ribbons that supports good electronic conductivity while the Mg-rich compound has a better possibility of a percolating network for ionic conductivity. The Fe-rich compound $Mg_{2/3}Fe_{4/3}B_2O_5$ has the highest theoretical capacity for one-electron Fe redox chemistry (186 mAh/g), with a hypothetical end product of $Fe_{4/3}B_2O_5$ after full oxidation of Fe^{2+} to Fe^{3+}, and is therefore the focus of the current study.

Both the x = 2/3 and x = 4/3 phases could be prepared by solid state reaction, as evaluated from their synchrotron X-ray diffraction patterns (Figure 5.4). The introduction of Fe into the x = 2 end member of $Mg_2B_2O_5$ clearly changed the intensity of the observed X-ray

diffraction peaks, but did not alter the triclinic crystal system of $Mg_2B_2O_5$. The x = 0 end member of $Fe_2B_2O_5$ powder is more difficult to produce due to the need to control the Fe valence, and this compound was not prepared and evaluated in the course of this work. However, the lattice parameters of $Fe_2B_2O_5$ from prior report were included in the current analysis [17]. As shown in Figure 3b, the unit cell volume of $Mg_xFe_{2-x}B_2O_5$ decreases with increasing Mg content, as expected for the smaller ionic radius of Mg^{2+} (0.72 Å) relative to Fe^{2+} (0.78 Å), and this change is nearly linear in accord with Vegard's law.

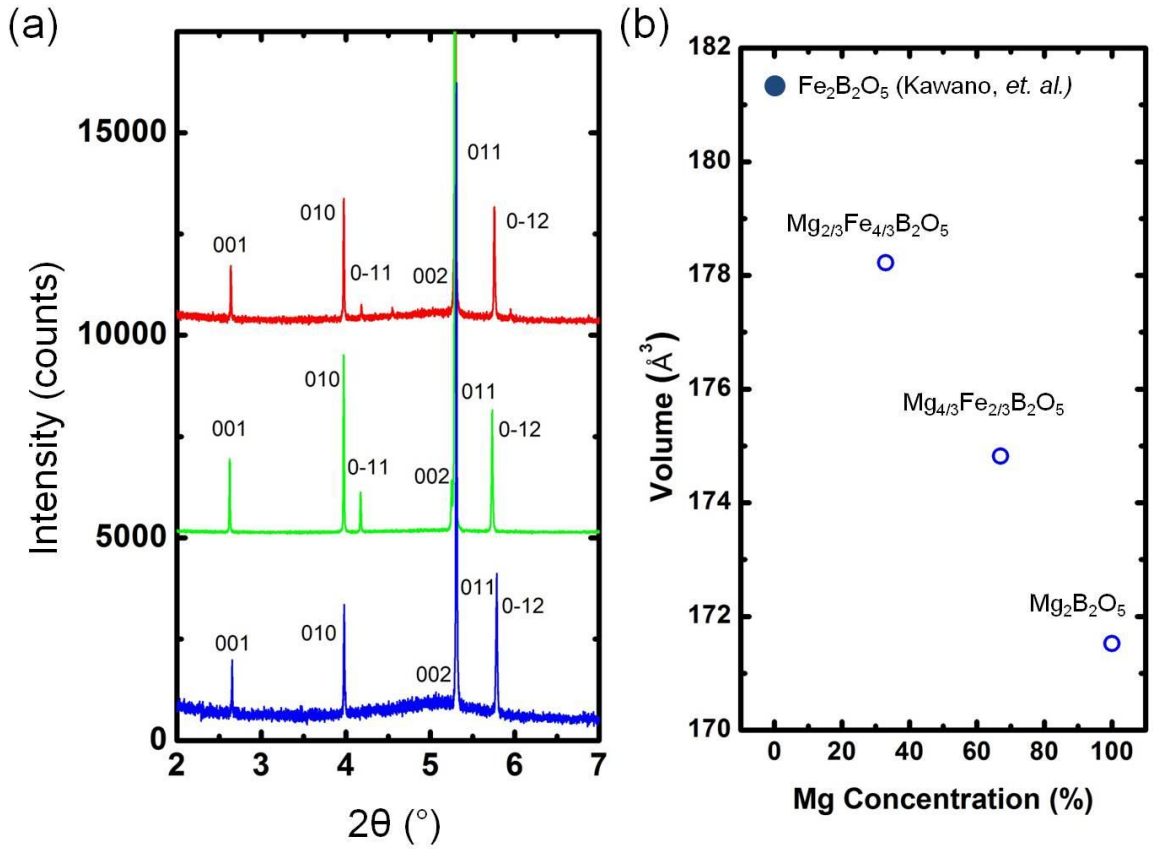

Figure 5.4. (a) Diffraction patterns of $Mg_{2/3}Fe_{4/3}B_2O_5$ (red), $Mg_{4/3}Fe_{2/3}B_2O_5$ (green) and $Mg_2B_2O_5$ (blue) (λ ~ 0.41 Å) (b) Dependence of unit cell volume on cation fraction of Mg, defined as [Mg] / ([Mg] + [Fe]). The volume data for $Fe_2B_2O_5$ was obtained from ref 17.

The structures of $Mg_{2/3}Fe_{4/3}B_2O_5$ and $Mg_{4/3}Fe_{2/3}B_2O_5$ were further investigated through the Rietveld refinement of time-of-flight neutron diffraction, which provides good sensitivity for all elements contained in these compounds (coherent scattering lengths in fm are Mg, 5.38; Fe, 9.45; ^{11}B, 5.30; O, 5.80) and which benefits from probing the more localized nucleus rather than the more delocalized electron cloud that X-rays are primarily sensitive to. It was found that the $P\bar{1}$ structure previously determined for the end members of $Mg_2B_2O_5$ and $Fe_2B_2O_5$ was effective for describing both the x = 2/3 and the x = 4/3 phases. The refinement and structural parameters obtained for these phases are given in Tables 5.2-5. Compared to the Mg/V distribution in $MgVBO_4$ where a majority of Mg occupies the M_A site in the 4-column ribbon framework, Mg^{2+} is found to be nearly randomly distributed between the M_A and M_B crystallographic sites in $Mg_{2/3}Fe_{4/3}B_2O_5$ (0.37/0.30 vs. 0.33/0.33 for random mixing) and $Mg_{4/3}Fe_{2/3}B_2O_5$ (0.72/0.61 vs. 0.67/0.67 for random mixing) when the site occupancies and displacement parameters are both freely refined. Since these two sites are crystallographically inequivalent, it is thermodynamically impossible for a truly random distribution to be the lowest free energy state. However, the actual site occupancies will be indistinguishable from a fully random distribution if the relative energies of ordered and disordered states are small relative to kT at the synthesis temperature (950 ℃ = 105 meV). The best R-value was obtained when the refinement is constrained to have partially disordered cations, which is significantly lower than that obtained when an ordered distribution of Mg and Fe is assumed (R_{wp} of 5.326 vs. 5.718). However, a complete random mixing of Mg and Fe only resulted in a marginally increase of R_{wp} from 5.326 to 5.330, as opposed to the partially disordered model. Therefore, we concluded that the Fe and Mg are randomly mixed in the $Mg_xFe_{2-x}B_2O_5$ phases.

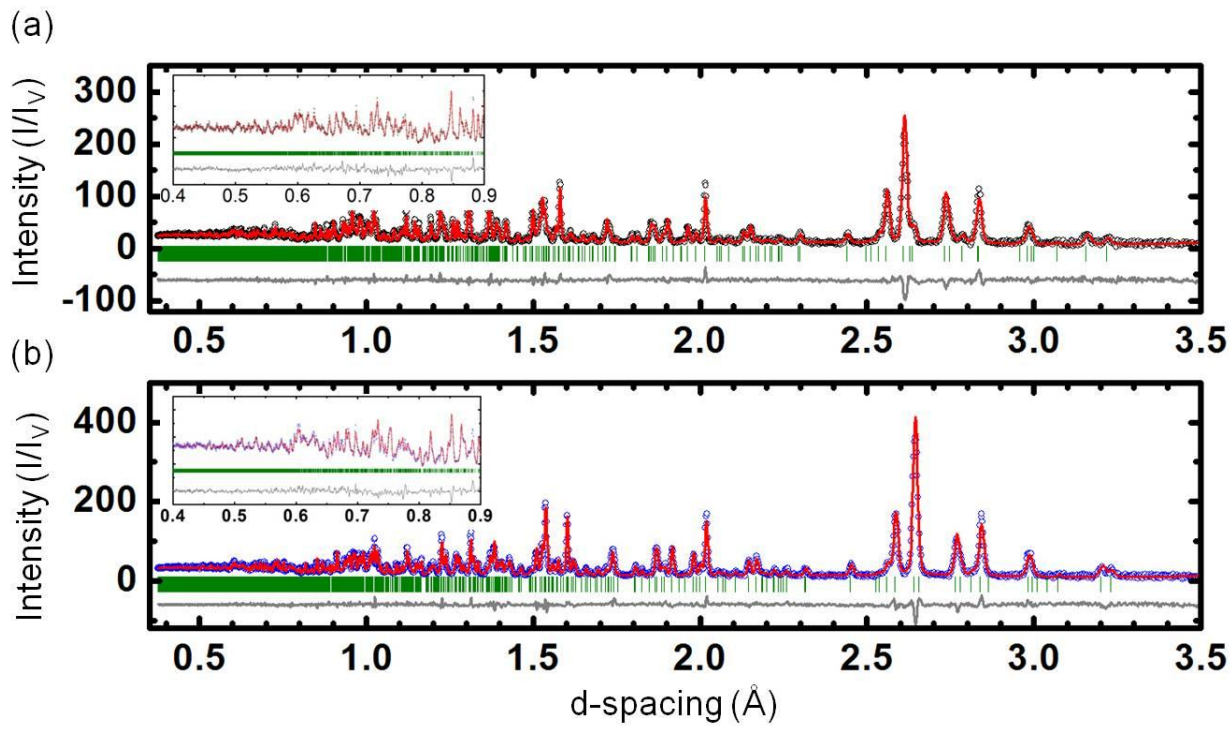

Figure 5.5. Rietveld refinement of $Mg_{2/3}Fe_{4/3}B_2O_5$ (bottom), $Mg_{4/3}Fe_{2/3}B_2O_5$ (top) based on TOF neutron diffraction data.

Table 5.2. Crystallographic data for $Mg_{2/3}Fe_{4/3}B_2O_5$ based on time-of-flight (TOF) neutron diffraction

Radiation	TOF neutron (POWGEN, SNS)
Crystal system	Triclinic
Space group	$P\bar{1}$ (#2)
Lattice parameters	a= 3.2030(6) Å, b= 6.165(1) Å, c= 9.332(2) Å, α= 104.563 (3) °, β= 90.858(2)°, γ= 91.767(2)°
Cell volume	178.24(5) $Å^3$
Density (calculated)	3.6029 g/cm^3
λ	0.533 Å- 1.599 Å
R_{wp}	5.326%
R_p	6.121%
χ^2	3.961

Table 5.3. Atomic coordinates and thermal parameters for $Mg_{2/3}Fe_{4/3}B_2O_5$

Atom	Wyck.	*x/a*	*y/b*	*z/c*	Occ.	B_{iso} (Å^2)
M_A	2i	0.73578(98)	0.21075(49)	0.36063(32)	Mg = 0.33(2) Fe = 0.67(2)	1.32(8)
M_B	2i	0.23470(97)	0.36714(48)	0.10089(33)	Mg = 0.33(2) Fe= 0.67 (2)	1.34(6)
B1	2i	0.34108(75)	0.87608(28)	0.17230(19)	1	0.50(6)
B2	2i	0.30524(83)	0.31795(27)	0.64720(19)	1	0.66(7)
O1	2i	0.2273(11)	0.09037(33)	0.18203(38)	1	0.91(5)
O2	2i	0.2641(13)	0.69526(42)	0.05473(28)	1	0.94(6)
O3	2i	0.44269(84)	0.14383(33)	0.70234(21)	1	0.87(5)
O4	2i	0.2414(13)	0.27643(61)	0.49812(22)	1	1.04(6)
O5	2i	0.7422(12)	0.47473(37)	0.25935(37)	1	0.73(5)

Table 5.4. Crystallographic data for $Mg_{4/3}Fe_{2/3}B_2O_5$ based on time-of-flight (TOF) neutron diffraction

Radiation	TOF neutron (POWGEN, SNS)
Crystal system	Triclinic
Space group	$P\bar{1}$ (#2)
Lattice parameters	a= 3.1590(5) Å, b= 6.159(1) Å, c= 9.271(1) Å, α= 104.504(3) °, β= 90.716(3)°, γ= 91.887(2)°
Cell volume	174.52(5) $Å^3$
Density (calculated)	3.30654 g/cm^3
λ	0.533 - 1.599 Å
R_{wp}	5.577%
R_p	6.663%
χ^2	3.578

Table 5.5. Atomic coordinates and thermal parameters for $Mg_{4/3}Fe_{2/3}B_2O_5$

Atom	Wyck.	*x/a*	*y/b*	*z/c*	Occ.	B_{iso} (Å^2)
M_A	2i	0.7300(12)	0.21133(58)	0.35881(35)	Mg = 0.67(2) Fe = 0.33(2)	2.6(2)
M_B	2i	0.2331(11)	0.36866(60)	0.10205(40)	Mg = 0.67(2) Fe= 0.33(2)	2.9(3)
B1	2i	0.33785(76)	0.87689(28)	0.17121(19)	1	0.61(4)
B2	2i	0.30312(87)	0.31534(27)	0.64633(19)	1	0.80(5)
O1	2i	0.2246(13)	0.09221(33)	0.18081(44)	1	0.92(5)
O2	2i	0.2606(13)	0.69340(51)	0.05436(33)	1	0.75(6)
O3	2i	0.43698(82)	0.14137(33)	0.70343(21)	1	0.77(5)
O4	2i	0.2383(14)	0.27171(65)	0.49577(22)	1	1.17(6)
O5	2i	0.7440(13)	0.47735(37)	0.25971(40)	1	0.81(6)

The demagnesiation of the x = 2/3 and x = 4/3 samples were attempted by both chemical and thermal treatments. While there was no evidence from color changes or from the lattice parameters determined from X-ray diffraction suggests that aqueous persulfate ions were able to drive the removal of Mg from either structure at room temperature, the thermal oxidation of these samples induced substantial changes that suggested Mg removal is likely occurring. Preliminary analysis on a sample of intermediate composition (x = 1) by TGA and *ex situ*

laboratory diffraction suggested that oxidation could occur without decomposition of the lattice over an approximate temperature range of 200 – 500 ℃ (Fig. 5.6). More detailed structural studies were therefore carried out on the x = 2/3 and x = 4/3 samples heated at either 250 ℃ or 400 ℃ for 24 hours.

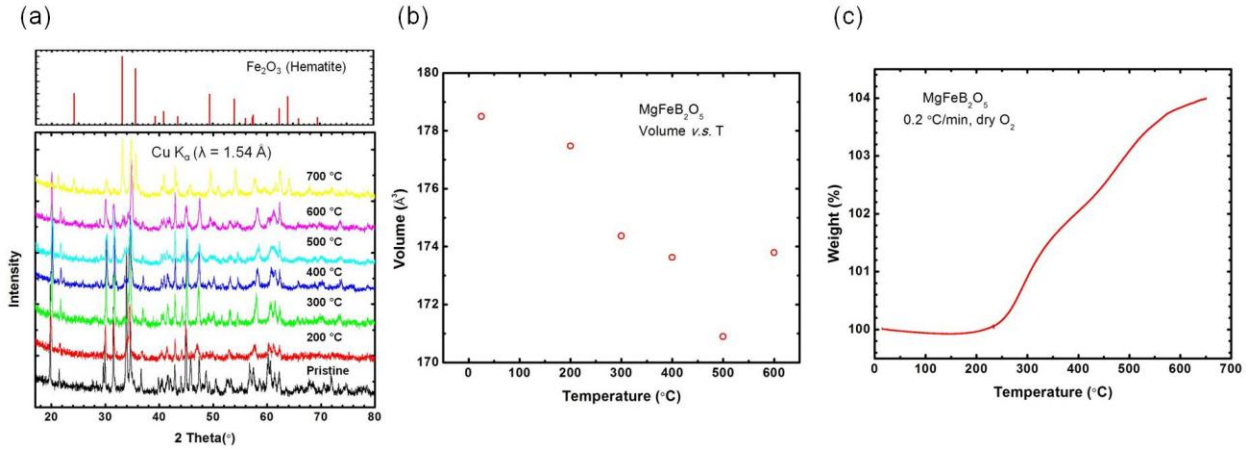

Figure 5.6. (a) X-ray diffraction patterns of "$MgFeB_2O_5$" that are heated at different temperatures in air for one day (from 200 ℃ to 700 ℃). (b) Volumes obtained by Le Bail refinement for "$MgFeB_2O_5$" samples that are heated at different temperatures. (c) Thermogravimetric curve of "$MgFeB_2O_5$" heated at 0.2 ℃ min^{-1} in dry O_2.

Ex situ synchrotron X-ray diffraction collected on powder samples of $Mg_{2/3}Fe_{4/3}B_2O_5$ heated at 250 ℃ and 400 ℃ show both clear shifts in peak positions (indicative of changing lattice parameters) and also large changes in diffraction peak intensities (which suggest substantial changes in site occupancies), as shown in Figure 5.7. These synchrotron X-ray diffraction patterns are free of peaks from the Fe_2O_3 impurity phase that was found to be the eventual decomposition produce at higher temperatures in our preliminary studies, suggesting that the framework of $Mg_{2/3}Fe_{4/3}B_2O_5$ is preserved during oxidation and can thus support the

partial removal of Mg^{2+} ions. The refined lattice parameters indicate that the volume decreases by 2.1% and 2.6% for samples treated at 250 ℃ and 400 ℃, respectively. This decreased volume is expected as oxidation will result in both the removal of Mg^{2+} ions and in the oxidation of Fe^{2+} to Fe^{3+}, two changes which should both promote a reduction in unit cell volume. Additionally, it was observed that there was noticeable peak asymmetry in the 250 ℃ data, but not in the 400 ℃ data. The asymmetry is attributed to the skewed distribution of lattice parameters that results from the diffusion-limited inhomogeneous removal of Mg^{2+} ions at the lower temperature, and which is absent in the 400 ℃ sample, a temperature at which these ions have a greatly enhanced mobility. Similar behavior in all aspects of diffraction was also observed for $Mg_{4/3}Fe_{2/3}B_2O_5$ samples (Figure 5.8).

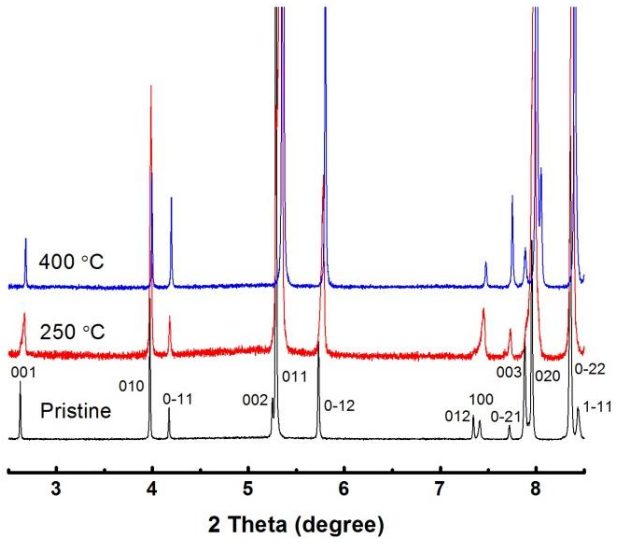

Figure 5.7. Comparison of synchrotron X-ray diffraction pattern (λ ~ 0.41 Å) for pristine $Mg_{2/3}Fe_{4/3}B_2O_5$ with those obtained after heating for 24 hours at 250 ℃ and 400 ℃.

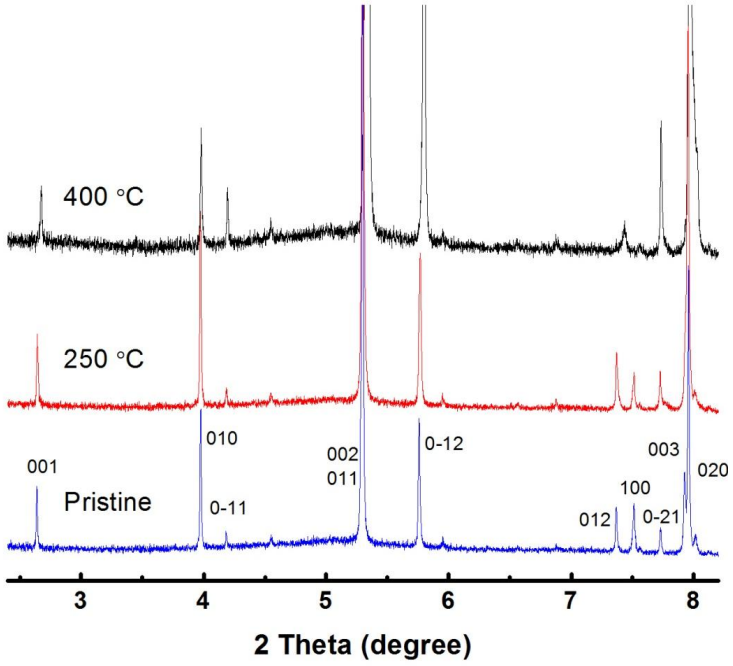

Figure 5.8. Diffraction patterns of the pristine $Mg_{4/3}Fe_{2/3}B_2O_5$, and samples were treated at 250 ℃ and 400 ℃. The data were collected at 11BM beamline of APS with a wavelength of 0.41 Å. A systematic peak shift toward higher angles is observed, suggesting a volume contraction of $Mg_{4/3}Fe_{2/3}B_2O_5$ after heating under air.

Time-of-flight neutron diffraction data was therefore also collected for thermally oxidized samples of the x = 2/3 phase in order to allow the Mg content on the M_A and M_B sites of $Mg_{2/3}Fe_{4/3}B_2O_5$ to be explicitly quantified in Rietveld refinements using identical samples to those studied by synchrotron diffraction. When the structural models obtained for different temperatures were compared, we observed a B as well as Mg loss from room temperature to 250 ℃, and a further Mg loss when the sample was heated at 400 ℃ (Tables 5.6-9). The loss of Mg^{2+} ions should also induce a change in the bond distances of the octahedral sites. While it is quite challenging to effectively obtain site occupancies when three species are mixed on a single

site (Mg, Fe, and vacancies), the bond distances obtained by Rietveld refinement should be insensitive to the nature of the central cation and thus provide an independent mechanism of following the changes in the crystal structure that occur on heating. When the 400 ℃ sample is compared with the pristine sample, the average bond distance for the M_A site is reduced from 2.134 to 2.089 Å, while the M_B site changes from 2.149 to 2.128 Å. The substantially larger reduction of bond distances on the M_A site suggests that the oxidation of Fe^{2+} to Fe^{3+} occurs primarily on this site, and that the induced changes in oxygen positions are larger than those driven by the removal of Mg^{2+} ions from the M_B site.

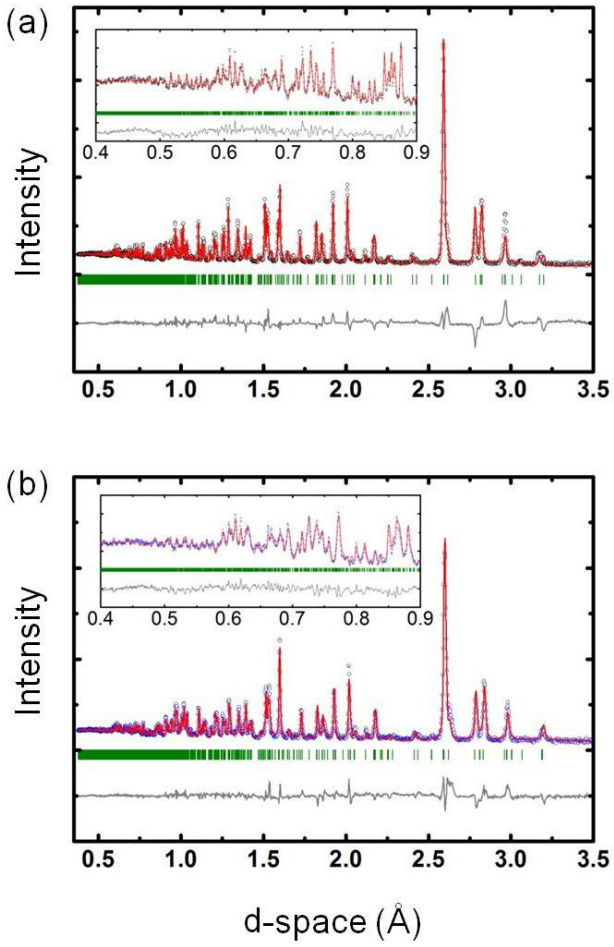

Figure 5.9. Rietveld refinement of TOF neutron diffraction data for the $Mg_{2/3}Fe_{4/3}B_2O_5$ samples that were treated at 250 ℃ (bottom) and 400 ℃ (top) for 1 day.

5.3.3 Insights into Mg^{2+} diffusion: bond valence sum map analysis

$FePO_4$, the delithiated form of olivine $LiFePO_4$, has been recently proposed as a cathode material for Mg-ion battery applications based on the relatively high voltage calculated for this system in DFT calculations [29]. However, no estimate of the kinetic barriers to Mg-ion diffusion was made as a part of that work. The BVS difference map calculated for this compound (Figure

5.10a) forms a percolating network with a very low threshold ($|\Delta V| < 0.1$ v.u.), suggesting that there are no structural barriers to diffusion within this framework, with the same diffusion pathway topology (1D diffusion path along *b*-axis) predicted for both Mg^{2+} and Li^{+} [30]. This compound should be therefore considered as a promising candidate battery cathode in which Mg-ion diffusion might be observed at or near room temperature.

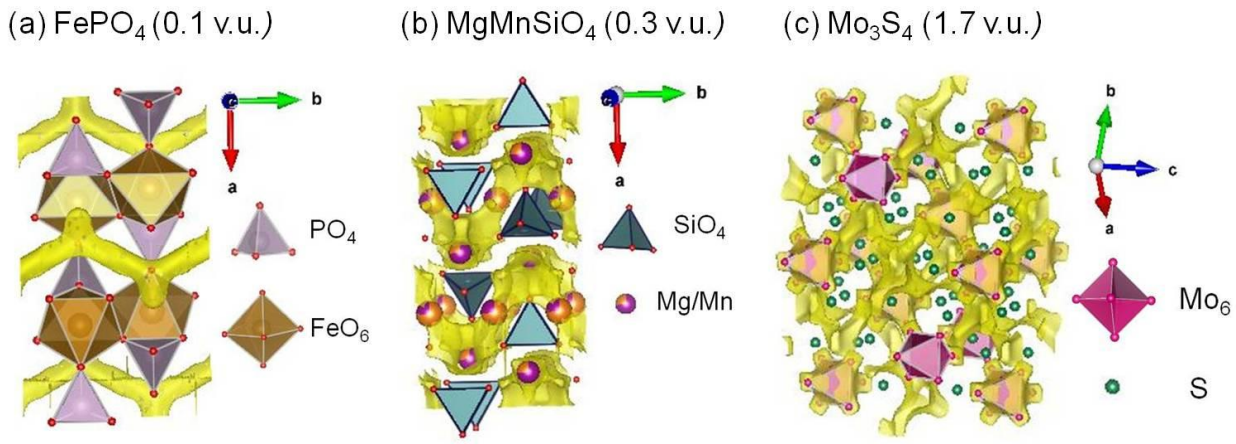

Figure 5.10. Bond valence sum difference maps (and $|\Delta V|$ thresholds used in their construction) for $FePO_4$ (0.1 v.u.), $MgMnSiO_4$ (0.3 v.u.), and Mo_6S_8 (1.7 v.u.). These maps were calculated for Mg^{2+} using the conventional bond valence parameters previously determined for O^{2-} ($FePO_4$, $MgMnSiO_4$) or S^{2-} (Mo_6S_8).

A second olivine-type compound of $MgMnSiO_4$ was also investigated. In contrast to the almost perfect ordering of Li and Fe between the two available octahedral sites in the olivine structural framework, Mg and Mn are partially disordered resulting in a 73/27 distribution of cations with the Mn ions preferentially occupying the site analogous to that of Li in $LiFePO_4$ [31]. Based on the BVS map (Fig. 5.10b), it is expected that Mg^{2+} diffusion occurs through a pathway

that connects both the primary and minority octahedral sites in which Mg can be found. The threshold $|\Delta V|$ barrier for establishing a Mg^{2+} percolation pathway is 0.3 v.u.. Since the topology of the minimal percolation network requires access to both types of octahedral sites, this pathway is expected to be effectively blocked by the immobile Mn cations in both the majority and minority sites, making it likely that the actual barrier to diffusion is much higher than that suggested by the percolation threshold of 0.3 v.u.

The Chrevrel phase Mo_3S_4 is perhaps the only effective cathode material for Mg-ion battery applications that has been demonstrated to date [2]. Despite the experimentally observed mobility of Mg^{2+} ions at room temperature, the BVS method does not predict that this framework will support Mg-ion diffusion as the percolation threshold is $|\Delta V| > 1.7$ v.u. (Fig. 5.10c). This Chevrel phase structure differs from that of most solid state compounds in that it consists of Mo_6S_8 clusters with many strong internal covalent bonds, but there is no clear S-S covalent bond connecting neighboring clusters (the shortest S-S bond length is ~3.3 Å). This suggests that the Chevrel framework can be much more readily distorted than the hard oxide or oxoanion framework of conventional Li-ion battery systems, and that the static structural snapshot used for BVS calculations is inadequate for making accurate predictions if large dynamic structural changes occur in response to the intercalation and de-intercalation of ions. Given the lack of success in discovering rigid oxide frameworks which permit Mg^{2+} ion mobility at room temperature, it is perhaps appropriate to devote additional efforts to identifying and evaluating structures with "soft" modes for their suitability for Mg-ion electrodes.

The potential for the frameworks of $Mg_{2/3}Fe_{4/3}B_2O_5$ and $MgVBO_4$ to support Mg-ion diffusion can be evaluated in the context of these baseline investigations. The $MgVBO_4$ map calculated for MVB does not reach the percolation limit until a threshold of about 1.2 v.u.,

indicating that Mg^{2+} ions are essentially immobile within this structure (Fig. 5.11). Furthermore, the BVS-predicted pathway for hopping from one octahedral site to another involves crossing directly in between two borate group triangles, and will result in Mg^{2+} ions to pass two B atoms that are only 3.1 Å apart (Fig. 5.11b). Since electrostatic repulsions are not included in BVS calculations, the true barrier for Mg-ion diffusion will be much larger than that estimated using the BVS method. As a result, it can be concluded that Mg^{2+} ions will be fully immobilized both at room temperature and at elevated temperatures. Given the unfavorable diffusion network topology of $MgVBO_4$, it is improbable that the diffusion of Mg^{2+} can be enabled by chemical substitution, and this general structure type should not be investigated further for applications requiring Mg^{2+} diffusion (intercalation-type batteries, solid state electrolytes, *etc.*).

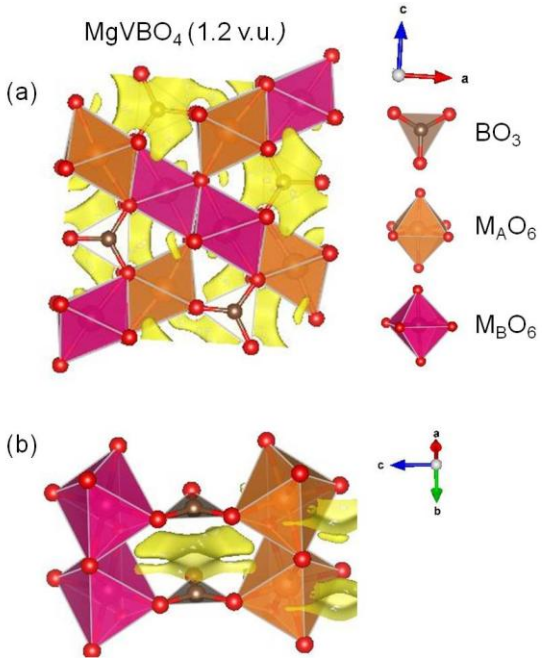

Figure 5.11. Bond valence sum difference maps (and |ΔV| threshold used in the construction) for $MgVBO_4$ (1.2 v.u.). As shown in (b), the only interstitial space that might be accessible by Mg^{2+} is sandwiched between two B atoms of the borate group.

While the orthoborate framework of $MgVBO_4$ greatly inhibits Mg-ion diffusion, the analogous ribbon structure of pyroborate $Mg_{2/3}Fe_{4/3}B_2O_5$ has a nearly ideal topology that results in a defect-tolerant pathway for Mg-ion diffusion enabled by the different geometric pattern in which the quadruple octahedral ribbons are arranged. As seen in Fig. 5.12, there are two types of interstitial defect sites (I_A and I_B) which are predicted to readily accommodate Mg^{2+} ions that have hopped out of their original octahedral site. Each defect site can be readily accessed from just two octahedral cation sites which are both of the same type (M_A or M_B), and these two defect sites are therefore labeled as I_A, and I_B. The I_A interstitial sites linking pairs of M_A cations have a strongly skewed rectangular arrangement of oxygen anions at their corners, while the I_B interstitial sites linking pairs of M_B cations form a more regular rectangular environment that is expected to be more accessible to Mg^{2+} ions based on geometric considerations. Indeed, the more open nature of I_B sites allows them to be connected into a one-dimensional (1D) channel permitting Mg-ion diffusion parallel to the ribbons (*a*-axis direction) at a much lower valence threshold (0.2 v.u.) than the I_A sites (0.5 v.u.).

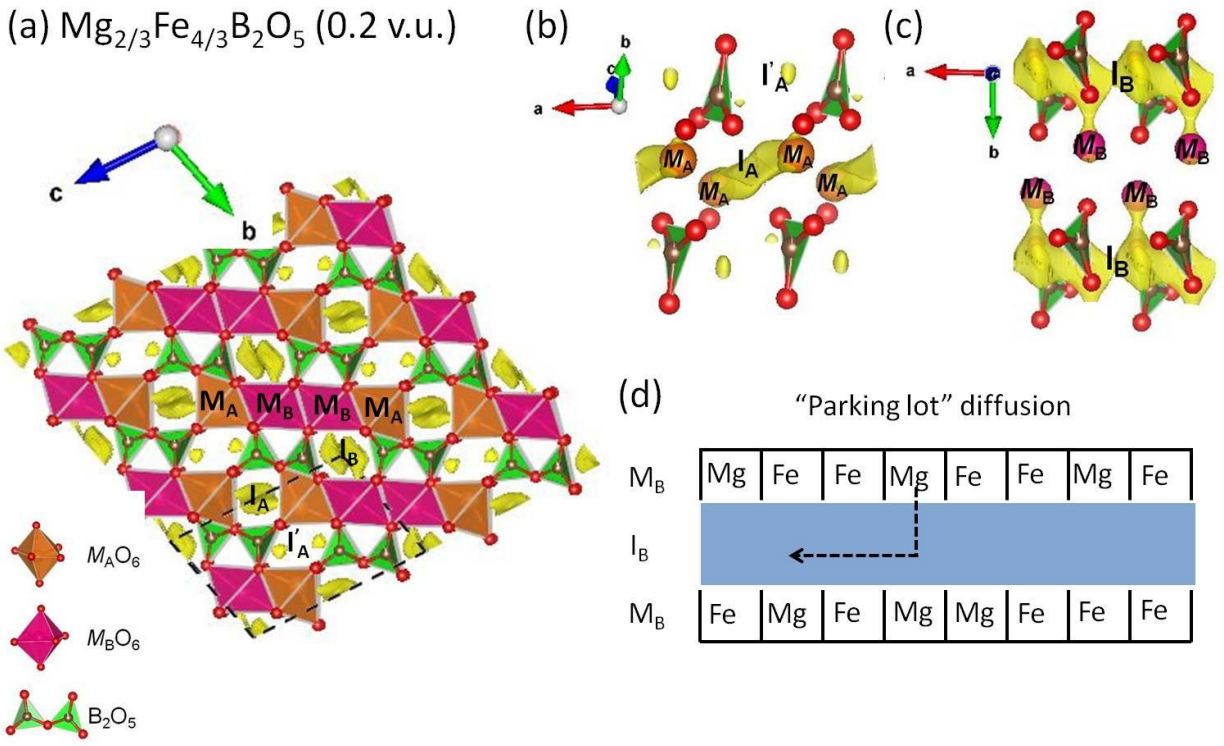

Figure 5.12. Bond valence sum difference maps (and |ΔV| threshold used in the construction) for $Mg_{2/3}Fe_{4/3}B_2O_5$ (0.2 v.u.). As shown in (a), when the BVS map was viewed along the a direction, no percolation diffusion path is observed within the *bc* plane. In the unit cell of $Mg_{2/3}Fe_{3/4}B_2O_5$, as highlighted by the black dotted lines in (a), three types of interstitial defect sites are present (I_A, I'_A and I_B). Only I_A and I_B sites are accessible by Mg ions that are on the M_A and M_B octahedral sites. As shown in (b) and (c), only I_B sites which connect the M_B crystallographic site form a 1D percolation channel. The Mg^{2+} conduction pathways are tolerant to disorder as illustrated in (d). By making analogy to a parking lot, Mg^{2+} ions are parked in octahedral sites until thermally excited into the interstitial sites in the aisles of the parking lot. The ions can then travel freely through the interstitial sites in the aisles, and are therefore unaffected by the Mg/Fe disorder on the octahedral sites.

When viewed from the side, it can be seen that these 1D channels are completely tolerant to the presence of defects on the octahedral sites (Fig. 5.12c). These channels form aisles like those in a parking lot, in which Mg^{2+} ions are typically "parked" in octahedral sites (Fig. 5.12d). However, once the Mg^{2+} ions pull out of their parking spot, they can move continuously through these aisles without having to enter another octahedral site. Therefore, the presence of Fe^{2+} or Fe^{3+} ions in the other parking spots will not inhibit the facile diffusion of Mg^{2+} ions through the aisles. Of course, if the Fe ions do leave their parking spot and enter the aisle, they do have the ability to impact the diffusivity of Mg ions in these channels, though it is expected to be relatively easy for Fe ions in the aisle to re-enter a parking spot. While the presence of site disorder is known to have a strongly deleterious effect on the conductivity of mobile ions in olivine battery cathodes such as $LiFePO_4$, the mobility of Mg^{2+} ions in the pyroborate structure of $Mg_xFe_{2-x}B_2O_5$ should be negligibly affected by Mg/Fe disorder on the octahedral cation sites. This should be a general characteristic of structures whose primary diffusion pathway is through interstitial sites.

It should be noted that the achievable capacity of $Mg_xFe_{2-x}B_2O_5$ cathodes will be affected by the proportion of Mg ions on the M_A and M_B sites. The structural refinements of demagnesiated $Mg_{2/3}Fe_{4/3}B_2O_5$ samples prepared by thermal oxidation at 250 and 400 ℃ indicate that Mg ions are removed from the M_B site and not the M_A site. This general conclusion is robust (large amounts of Mg are removed from the M_B site), although the general limitations of working with powder diffraction data and the specific uncertainty associated with the fraction of Fe ions on the M_A and M_B sites possibly changing during the thermal treatment (due to the possible mobility of Fe at these elevated temperature) make it impossible for us to rule out the loss of small amounts of Mg from the M_A site. The refinements indicate that thermal energy at

modest temperatures of 250 – 400 ℃ is sufficient to enable Mg-ion motion through the I_B site, but is not sufficient to permit Mg-ions to access the I_A site. As a result, the Mg ions from the M_A site will not contribute to the achievable specific capacity of this framework. The two best pathways for improving the performance of the pyroborate framework are (1) chemical substitutions that improve the mobility of Mg^{2+} ions travelling through the I_B interstitial site in this structure, and (2) thermal treatments or chemical substitutions that result in a larger number of Mg cations on the M_B octahedral site, enhancing the specific capacity.

5.4 Conclusions

Two classes of borates with quadruple octahedral ribbons were investigated for their suitability as Mg-ion battery cathodes due to their high theoretical capacity for this application. The orthoborate $MgVBO_4$ and the pyroborate compounds $Mg_xFe_{2-x}B_2O_5$ were synthesized by solid state methods and their structures were for the first time accurately determined through the Rietveld refinement of synchrotron X-ray and time-of-flight neutron diffraction data. In both compounds, there two distinct types of octahedral sites – the M_A site at the edge of the quadruple ribbons and the M_B site at the center of the quadruple ribbons. Both experimental (attempted chemical and thermal oxidation) and theoretical (bond valence sum difference maps) analysis suggests that Mg ions are fully immobilized in $MgVBO_4$ over the full range of temperatures over which this framework is stable (below ~450 ℃). In contrast, it is experimentally demonstrated that Mg-ions can be removed from $Mg_xFe_{2-x}B_2O_5$ (x = 2/3, 4/3) by thermal oxidation over an approximate temperature range of 200 – 500 ℃. BVS difference maps suggest that the preferred diffusion pathway for Mg^{2+} ions is through interstitial sites which are paired with the inner M_B

octahedral sites, and it is confirmed through Rietveld refinements that only the Mg^{2+} ions at this site are selectively depopulated during thermal oxidation, validating the BVS difference map method as a predictive tool for understanding Mg-ion diffusion. The topology of this interstitial diffusion pathway resembles that of the aisle in a parking lot and therefore makes this pathway insensitive to disorder (Mg/Fe mixing) on the M_B octahedral site, allowing extra flexibility in future efforts to improve the Mg-ion mobility in this structure by chemical substitution. Although the present the pyroborate $Mg_xFe_{2-x}B_2O_5$ compounds do not have mobile Mg^{2+} ions at room temperature, their ability to transport Mg^{2+} ions at modest temperatures (~250 ℃) is a promising advance given the current lack of oxide structures with the ability to reversibly intercalate Mg-ions at room temperature. Based on the BVS analysis, it is expected that both the present pyroborate and the well-known olivine structure types have good potential for supporting Mg-ion diffusion at or near room temperature with appropriate chemical substitution.

5.5 References

1. Novak, P.; Imhof, R.; Haas, O., Magnesium insertion electrodes for rechargeable nonaqueous batteries - a competitive alternative to lithium? *Electrochim Acta* **1999,** *45* (1-2), 351-367.

2. Aurbach, D.; Lu, Z.; Schechter, A.; Gofer, Y.; Gizbar, H.; Turgeman, R.; Cohen, Y.; Moshkovich, M.; Levi, E., Prototype systems for rechargeable magnesium batteries. *Nature* **2000,** *407* (6805), 724-727.

3. Gregory, T. D.; Hoffman, R. J.; Winterton, R. C., Nonaqueous Electrochemistry of Magnesium: Applications to Energy Storage. *J Electrochem Soc* **1990,** *137* (3), 775-780.

4. Schollhorn, R.; Sick, E.; Lerf, A., Reversible Topotactic Redox Reactions of Layered Dichalcogenides. *Mater Res Bull* **1975,** *10* (10), 1005-1012.

5. NuLi, Y.; Zheng, Y.; Wang, Y.; Yang, J.; Wang, J., Electrochemical intercalation of Mg^{2+} in 3D hierarchically porous magnesium cobalt silicate and its application as an advanced cathode material in rechargeable magnesium batteries. *J Mater Chem* **2011,** *21* (33), 12437-12443.

6. Yamada, A.; Iwane, N.; Harada, Y.; Nishimura, S.; Koyama, Y.; Tanaka, I., Lithium Iron Borates as High-Capacity Battery Electrodes. *Adv Mater* **2010,** *22* (32), 3583-3587.

7. Kim, J. C.; Moore, C. J.; Kang, B.; Hautier, G.; Jain, A.; Ceder, G., Synthesis and Electrochemical Properties of Monoclinic $LiMnBO_3$ as a Li Intercalation Material. *J Electrochem Soc* **2011,** *158* (3), A309-A315.

8. Bo, S. H.; Wang, F.; Janssen, Y.; Zeng, D. L.; Nam, K. W.; Xu, W. Q.; Du, L. S.; Graetz, J.; Yang, X. Q.; Zhu, Y. M.; Parise, J. B.; Grey, C. P.; Khalifah, P. G., Degradation and (de)lithiation processes in the high capacity battery material $LiFeBO_3$. *J Mater Chem* **2012,** *22* (18), 8799-8809.

9. Fernandes, J. C.; Guimaraes, R. B.; Continentino, M. A.; Borges, H. A.; Valarelli, J. V.; Lacerda, A., Titanium-Iii Warwickites - a Family of One-Dimensional Disordered Magnetic Systems. *Phys Rev B* **1994,** *50* (22), 16754-16757.

10. Norrestam, R., Structural Investigation of 2 Synthetic Warwickites - Undistorted Orthorhombic $MgScOBO_3$ and Distorted Monoclinic $Mg_{0.76}Mn_{1.24}OBO_3$. *Z Kristallogr* **1989,** *189* (1-2), 1-11.

11. Appel, P. W. U.; Bigi, S.; Brigatti, M. F., Crystal structure and chemistry of yuanfuliite and its relationships with warwickite. *Eur. J. Mineral.* **1999,** *11* (3), 483-491.

12. Angst, M.; Hermann, R. P.; Schweika, W.; Kim, J. W.; Khalifah, P.; Xiang, H. J.; Whangbo, M. H.; Kim, D. H.; Sales, B. C.; Mandrus, D., Incommensurate charge order phase in Fe_2OBO_3 due to geometrical frustration. *Phys Rev Lett* **2007,** *99* (25).

13. Angst, M.; Khalifah, P.; Hermann, R. P.; Xiang, H. J.; Whangbo, M. H.; Varadarajan, V.; Brill, J. W.; Sales, B. C.; Mandrus, D., Charge order superstructure with integer iron valence in Fe_2OBO_3. *Phys Rev Lett* **2007,** *99* (8).

14. Block, S.; Burley, G.; Perloff, A.; Mason, R. D., Refinement of the Crystal Structure of Triclinic Magnesium Pyroborate. *J Res Nat Bur Stand* **1959,** *62* (3), 95-100.

15. Guo, G. C.; Cheng, W. D.; Chen, J. T.; Huang, J. S.; Zhang, Q. E., Triclinic $Mg_2B_2O_5$. *Acta Crystallogr C* **1995,** *51*, 351-352.

16. Takeuchi, Y., The Crystal Structure of Magnesium Pyroborate. *Acta Crystallogr* **1952,** *5* (5), 574-581.

17. Kawano, T.; Morito, H.; Yamada, T.; Onuma, T.; Chichibu, S. F.; Yamane, H., Synthesis, crystal structure and characterization of iron pyroborate ($Fe_2B_2O_5$) single crystals (vol 182, pg 2004, 2009). *J Solid State Chem* **2009,** *182* (10), 2947-2947.

18. Fernandes, J. C.; Sarrat, F. S.; Guimaraes, R. B.; Freitas, R. S.; Continentino, M. A.; Doriguetto, A. C.; Mascarenhas, Y. P.; Ellena, J.; Castellano, E. E.; Tholence, J. L.; Dumas, J.; Ghivelder, L., Structure and magnetism of $MnMgB_2O_5$ and $Mn_2B_2O_5$. *Phys Rev B* **2003,** *67* (10).

19. Kawano, T.; Suehiro, T.; Sato, T.; Yamane, H., Preparation, crystal structure and photoluminescence of Mn^{2+}-doped magnesium pyroborates solid solutions, $(Mg_{1-x}Mn_x)_2B_2O_5$. *J Lumin* **2010,** *130* (11), 2161-2165.

20. Continentino, M. A.; Fernandes, J. C.; Guimaraes, R. B.; Boechat, B.; Borges, H. A.; Valarelli, J. V.; Haanappel, E.; Lacerda, A.; Silva, P. R. J., Strongly disordered Heisenberg spin-1 chains: Vanadium warwickites. *Philos Mag B* **1996,** *73* (4), 601-609.

21. Blum, P.; Bozon, H., Preparation electrolytique et constantes crystallagraphiques de quelques composes oxygenes a base de bore, vanadium ou titane. *Comptes Rendus Hebdomadaires Des Seances De L Academie Des Sciences* **1954,** *239* (14), 811-812.

22. Li, Y.; Fan, Z. Y.; Lu, J. G.; Chang, R. P. H., Synthesis of magnesium borate ($Mg_2B_2O_5$) nanowires by chemical vapor deposition method. *Chem Mater* **2004,** *16* (13), 2512-2514.

23. Tao, X. Y.; Li, X. D., Catalyst-free synthesis, structural, and mechanical characterization of twinned $Mg_2B_2O_5$ nanowires. *Nano Lett* **2008,** *8* (2), 505-510.

24. Whittingham, M. S.; Song, Y.; Lutta, S.; Zavalij, P. Y.; Chernova, N. A., Some transition metal (oxy)phosphates and vanadium oxides for lithium batteries. *J Mater Chem* **2005,** *15* (33), 3362-3379.

25. Yin, S. C.; Grondey, H.; Strobel, P.; Anne, M.; Nazar, L. F., Electrochemical Property: Structure Relationships in Monoclinic $Li_{3-y}V_2(PO4)_3$. *J Am Chem Soc* **2003,** *125* (34), 10402-10411.

26. Dodd, J. L.; Yazami, R.; Fultz, B., Phase diagram of $Li_{(x)}FePO4$. *Electrochem Solid St* **2006,** *9* (3), A151-A155.

27. Brown, I., Chemical and steric constraints in inorganic solids. *Acta Crystallographica Section B* **1992,** *48* (5), 553-572.

28. Brown, I., Influence of Chemical and Spatial Constraints on the Structures of Inorganic Compounds. *Acta Crystallographica Section B* **1997,** *53* (3), 381-393.

29. Ling, C.; Banerjee, D.; Song, W.; Zhang, M.; Matsui, M., First-principles study of the magnesiation of olivines: redox reaction mechanism, electrochemical and thermodynamic properties. *J Mater Chem* **2012,** *22* (27), 13517-13523.

30. Nishimura, S.-i.; Kobayashi, G.; Ohoyama, K.; Kanno, R.; Yashima, M.; Yamada, A., Experimental visualization of lithium diffusion in Li_xFePO_4. *Nat Mater* **2008,** *7* (9), 707-711.

31. Redfern, S. A. T.; Henderson, C. M. B.; Knight, K. S.; Wood, B. J., High-temperature order disorder in $(Fe_{0.5}Mn_{0.5})_{(2)}SiO_4$ and $(Mg_{0.5}Mn_{0.5})_{(2)}SiO_4$ olivines: An in situ neutron diffraction study. *Eur. J. Mineral.* **1997,** *9* (2), 287-300.

32. NuLi, Y.; Yang, J.; Li, Y.; Wang, J., Mesoporous magnesium manganese silicate as cathode materials for rechargeable magnesium batteries. *Chemical Communications* **2010,** *46* (21), 3794-3796.

Chapter 6

Conclusions

Detailed structural characterizations of transition metal borates for rechargeable battery applications were for the first time systematically studied in this dissertation. A particular focus of this dissertation study is to understand the structure-property correlations in the two general series of compounds (*i.e.*, lithium metal borates and magnesium metal borates).

Li*M*BO_3 (*M* = Fe and Co) were synthesized in various forms (*i.e.*, ceramic powder, nanocomposite and thin film), to evaluate their potential as cathodes for Li-ion batteries. The electrochemical performance of $LiFeBO_3$ is observed to be superior to that of $LiCoBO_3$. This is likely due to either the extremely low electronic conductivity associated with $LiCoBO_3$, or the relative thermodynamic instabilities of $Li_{1-x}CoBO_3$, making the delithiated phase impossible to access electrochemically to date.

The good electrochemical performance of $LiFeBO_3$ was achieved at the price of careful handling of the compound under rigorous control of air exposure. A central issue is the low operation voltage of $LiFeBO_3$ (~2.8 V *vs.* Li^+/Li), which leads to $LiFeBO_3$ delithiation and degradation by the oxidative constituents in air (*e.g.*, O_2, H_2O and CO_2). The degradation of $LiFeBO_3$ produces a distinct secondary phase with essentially the same structural framework as the parent $LiFeBO_3$ structure, but with Fe/Li disorder and likely Fe deficiency. This makes the conversion between $LiFeBO_3$ and its degraded counterpart an irreversible process. The degraded $LiFeBO_3$, however, can be cycled at a relatively low voltage (~1.8 V vs. Li^+/Li).

When compared with $LiFePO_4$, $LiFeBO_3$ shows poor electronic conductivity and low operation voltage (Fe^{3+}/Fe^{2+} redox couple). The former may be simply rationalized according to the connectivity of Fe-O polyhedra in the two different structures. While corner shared FeO_6 ocatahedra are connected within *bc* plane in $LiFePO_4$, edge-shared FeO_5 trigonal bipyramids only provide a possible 1D electronic conduction path along [1-10] direction in $LiFeBO_3$. The low operation voltage associated with $LiFeBO_3$ is likely related with the less eletronegativity of B than that of P (Pauling electronegativity scale), which yields less inductive effect based on the Goodenough formalism.

Future design of borate based compounds for Li-ion battery applications should therefore be directed to compounds showing multidimensionality of metal-oxygen connection, to provide good electronic conductivity. The use of Fe^{3+}/Fe^{2+} redox couple should be probably combined with the use of pyroborate group ($B_2O_5^{4-}$), as the use of pyroborate group may provide a higher operation voltage than that of borate group by making analogy to the relative voltages of Fe^{3+}/Fe^{2+} redox couples in $Li_2FeP_2O_7$ and $LiFePO_4$. Mn and Co based compounds should also be explored, since the Mn^{3+}/Mn^{2+} and Co^{3+}/Co^{2+} redox couples tend to operate at higher voltages than Fe^{3+}/Fe^{2+} redox couple.

Ribbon-type magnesium metal borates were also studied in this dissertation as potential cathodes for magnesium-ion battery applications. The ribbons in $MgVBO_4$ and $Mg_xFe_{2-x}B_2O_5$ are formed by 4-column-wide edge shared metal-oxygen octahedra, which extend infinitely along one lattice direction, although the topology of ribbon connections are different in these two structures. Intriguingly, it is observed that the pyroborate $Mg_xFe_{2-x}B_2O_5$ structural framework exhibits a defect tolerant Mg diffusion pattern, based on the bond-valence-sum map analysis and neutron diffraction studies. Since the interstitial spaces connecting MgO_6 octahedra are

accessible to Mg ions with a moderate activation barrier, Mg ions can hop out of their original "parking spots" and enter the interstitial "aisles" for diffusion to occur (a "parking lot" diffusion mechanism). It is expected that studies of related compounds can be a rewarding path in the search of cathode materials for Mg-ion battery applications.

Borates groups are light, and can be present in various forms, *e.g.*, trigonal planar BO_3^{3-}, tetrahedral BO_4^{5-}, and planar pyroborate $B_2O_5^{4-}$. Borate based compounds, therefore, provide an exciting platform for explorations of new battery materials. It is believed that many structural insights obtained from this dissertation study can serve as basis for the future exploration of transition metal borates for battery applications.